UNIVERSITÀ DEGLI STUDI DI TRIESTE

XXXI CICLO DEL DOTTORATO DI RICERCA IN NANOTECHNOLOGIE

INFLUENCE OF SUBSTRATE ON PHYSICAL PROPERTIES OF TRANSITION METAL COMPLEXES THIN FILMS

Settore Scientifico-Disciplinare: Fis/03

DOTTORANDO
ABHISHEK KUMAR

COORDINATOR
PROF. LUCIA PASQUATO

SUPERVISORE DI TESI
DR. MADDALENA PEDIO

ANNO ACCADEMICO 2017/2018

Contents

2

Chapter-1

Introduction

1.1 Molecules on Surfaces

The engineering of organized, low-dimensional molecular systems opens up new ways to control matter at nanoscale and the exploration of nanodevice concepts. Self organized growth of molecules on surfaces provides a versatile rout of realize complex nanosystems with desirable functional properties. Therefore, self organization of molecules presents promising prospect for miniaturization of electronic devices. Such miniaturization of electronic devices provides means to fabricate low cost and flexible devices due to possibility to develop molecular devices on flexible substrates. [1]

Bottom up approaches are an attractive choice for the functional molecular devices at nanometer scale. This approach of device fabrication allows precise control over the specific functionalities by appropriate selection of the molecular complexeses. The accurate measurement of electronic transport properties for metal- molecular junctions is challenging task in molecular electronics due to the involment of various physical processes . The charge transport through the molecular junctions is sensitive to molecule-molecule interactions, molecular conformations as well as metal-molecular contact geometry.[2]

There has been considerable interest in the growth of organic thin films for the development of molecular devices.[3] Porphyrin and Phathalocyanines molecular thin films are extensively studied in the literature for their potential applications in spintronics and photovoltaics. [4] However, crucial issue is to gain control over the physical properties of thin films due to their strong dependence on molecular structure and polymorphism. In this thesis, we investigate the structural, vibrational and electronic properties of organometallic molecules assembled in long range ordered networks grown on conducting substrates.

An important issue in molecular electronics is the molecular interface with electrodes as it controls the charge injection and the transport through the device.[3] The adsorption of organometallic molecules on metallic surfaces leads to the formation of interface dipole which is influenced by the interaction of macrocycle and central metal atom with substrate and strongly impact charge injection barriers [4]. A variety of processes can influence energy level alignment at molecule-substrate interface such as charge transfer due to molecule-substrate hybridization effects, push-back effect involving interaction of molecular π electron cloud and metallic substrate electron density and back donation of charge density from molecule to substrate leading to charge redistribution as shown in Figure 1.[4]
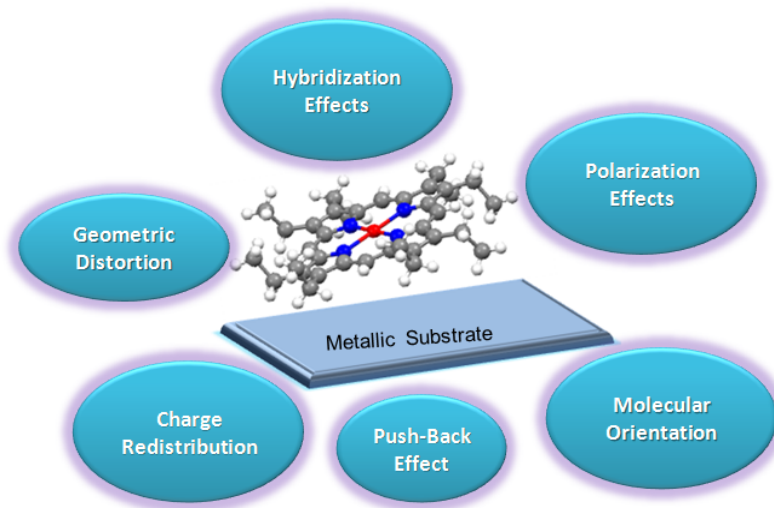
Figure 1 Schematic represntation of various processes at metal-molecule intrface.

The chemical reactivity, stability and nature of frontier moleculer orbitals for organometalic molecule present strong dependance on nature of central metal atom and substituent groups [2]. Therefore, an approporiate selection of organometalic molecule and substrate provides an ample opportunity to control and manipulate electronic and magnetic properties of molecular thin films.

Depending on the type of substrate and molecule one of the processes shown in Figure 1 can be dominant and in turn governs the overall energy level alignment and charge injection barriers at the interface.[5] However, there is no unified model to explain the above mentioned interface processes. Therefore, each molecule-substrate system has to be investigated by a multitechnique approach to get complementary information on the specific system.

The strength of molecule-substrate bond is an important criterion to broadly classify the interfaces. It is worthwhile to note that the strength of interaction not only depend on molecule and substrates involved in interface formation but also on the synthesis procedure adopted for interface formation. [4]

The work function of substrate depends on electrostatic potential across the surface and the bulk chemical potential. Physisorption of organic molecule on substrate can lead to changes in the electrostatic potential across the metal surface while bulk chemical potential remain unaffected.[6] There is significant difference between outer and inner electrostatic potential energies across metallic substrate known as metal-surface dipole potential energy. The work function of the substrate can be related to bulk chemical potential and metal-surface dipole potential energy. Adsorption of organic molecules leads to reduction in metal-surface dipole potential energy resulting in lower work function of metallic substrate after adsorption. In addition to physisorbed molecules, there is a possibility of chemical interaction between adsorbed molecule and metallic substrate. Such chemical bond may lead to up-shift or down shift of vacuum level due to net charge transfer to the molecule or metallic substrate. The push back

4

effect may also play significant role even in chemisorbed molecules due to proximity of metal – molecule electron clouds.[5]

The work function changes significantly for the adsorption of molecules on metallic substrates in the monolayer regime. There are contributions from different factors such as (i) "push-back" effect lowers the electron density of metal at the surface,(ii) an attractive surface potential leads to polarization of the molecules(iii) charge transfer between the two interacting subsystems, ie hybridization at metal-molecule interface,(iv) intrinsic dipole moment of the organic molecule, and (iv) i.e., the formation of the chemical bond. These contributions as a first approximation, the total WF shift can be written as the sum

$$\Delta WF = \Delta_{met} + \Delta_{pol} + \Delta_{chem} + \Delta_{dipole}$$

The formation of chemical or weaker bonds at the adsorption sites causes a rearrangement of the electron density on the adsorbate, connected to a significant change in some of the molecular orbitals. This electronic rearrangement can then be seen as a partial charge transfer between adsorbate and adsorption site. The direction of the electron charge transfer is controlled by the chemical potentials of the two species, with the electronic charge going from the species with higher chemical potential to the one with the lower chemical potential(μ_{SUB})

$$\mu_{SUB} = -\Phi_{SUB}$$

$$\mu_{SUB} = -(IE+EA)/2$$

The values of electronic affinity and ionization energy can be determined experimentally or by DFT calculations. Thus, the direction of charge transfer can be determined. [6]

There is possibility to tune the interfacial electronic properties by intermediate buffer layer between substrate and molecule. The presence of such buffer layer can notably influence the charge transfer across interface, push back effect and bond formation. In the absence of a unfied model to understand the energy level alignment for such peculiar metal-molecule interfaces , detailed photoemission analysis would be necessary. [6]

The transport properties of an organic device are dramatically affected by the molecular orientation relative to the current flow.[7] The most efficient current flow in a molecular film occurs along the direction of the direction of the stacked π bonds being coincident with the interaction between the π bonds of neighboring molecules. Likewise, the molecular orientation determines interfacial energetics and by controlling the relative molecular orientation at the donor/acceptor interfaces inorganic heterostructures the charge transfer and charge dissociation can be affected. It is therefore essential to control both the crystallinity of grown films and the molecular orientation.

In order to utilize the potential of molecules for novel electronic devices, in addition to metal-molecule interfaces, the information about the molecular orientation and molecule stacking is also significant. Thin films of phthalocyanins and porphyrins have been deposited on substrates of technological interest have been such as SiOx/Si and ITO and characterized to understand their physical properties. Depending on the substrate roughness and interaction with molecule film morphology and molecular stacking can be significantly affected. [18] The thesis aims to add to the existing knowledge of organic-inorganic interface along with an effort to establish interconnection with molecular order and physical properties of organic thin films.

Transition metal complexes on surfaces

Among tetrapyrrole complexes, metalloporphyrins and phthalocyanines have gained considerable scientific interests due to their intriguing electronic and magnetic properties.[8] These molecular thin films have shown promising applications in thin film organic field-effect transistors (OFETs), organic light emitting diodes (OLEDs) and organic photovoltaic devices[9]. Due to such impactful applications, considerable attention has been given to various factors influencing charge carrier mobility and light harvesting ability of molecular thin films.

Table 1 summarizes the transition metal complexes studied in this thesis. Tetraphenylporphyrins are an important class of tetrapyrrole complexes which exhibits potential to be utilized as building blocks in modern electronic and spintronics devices.[8] Tetraphenylporphyrin molecules tends to adopt a planar conformation on metallic substrates due to intermolecular interactions among molecules in the monolayer regime. However, due to intermolecular strain between porphyrin core and peripheral phenyl groups, planar conformation is energetically not favorable.[10] Therefore, in order to minimize the intermolecular strain, porphyrin core adopts a saddle-shapede formation.[10] STM studies for the adsorption of FeTPP, CoTPP on Ag(111) confirms the saddle–shaped molecular conformer. Such adsorption induced and non reactive structural deformations are influenced by molecule-substrate interaction.[10] Therefore, on a weekly interacting substrate such as HOPG such saddle shaped deformation of the macrocycle is not anticipated.

Another category of porphyrin molecules are the metal octaethylporphyrin (MOEP) molecules with eight peripheral ethyl groups. Ethyl groups can adopt different orientations in order to minimize steric hindrance and to obtain energetically stable configuration.[11] In addition, different 3d filling of central metal atom can notably impact the frontier molecular orbitals MOs energy level alignment, thereby influencing the interaction of porphyrin molecules with underling substrate. The self assembly and interfacial electronic properties of MOEP molecules adlayers on weakly interacting substrates can be influenced by molecular conformer and intermolecular interactions.

Although metalloporphyrins have structural similarity with phthalocyanines however these two classes of molecules differ in their macrocycle for the number of nitrogen atoms thereby notably

impacting polarization effects and macrocycle mediated interactions. In addition, metalloporphyrins with peripheral ethyl and phenyl groups exhibits more plasticity as compared to rigid phthalocyanine molecules. Due to which tertraphenylporphyrins molecules can adopt different molecular conformations. These factors can strongly influence the interaction of tetrapyrrole complexes adlayers with underlying substrate thereby notably impacting their electronic and magnetic properties.
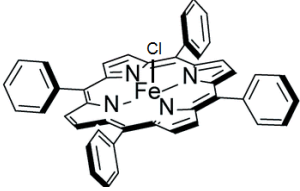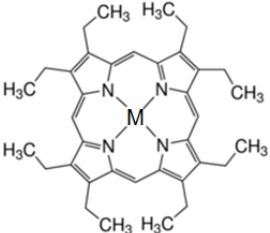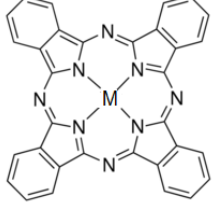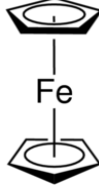
Transition Metal Complexes	Structure
Iron(III) porphyrin chloride	
Metal(II)Octaethylporphyrin	M=Zn, Ni, Cu
Metal(II) phthalocyanine	M=Cu,Co,Fe
Ferrocene [Fe(C$_5$H$_5$)$_2$]	

Table 1

Metal Phthalocyanine (MPc) molecules belong to the planar and fully conjugated transition metal complexes category of molecules. Similar to porphyrin molecules MPcs also exhibits strong light absorption properties in the visible region as well as thermal stability attributed by

the conjugated π-system. In contrast to porphyrin molecules, MPc molecules are not found in nature. These molecules possess good photostability and form ordered molecular structures on metallic substrates by thermal evaporation. Therefore, these molecules are an attractive choice for novel electronic devices such as thin film transistors, organic light-emitting diodes, and organic photovoltaic and liquid crystalline materials. [12] It has been observed that magnetic moment of plannar tertapyrrole complexs such as phthocyanines is quenched due to strong interaction with underlying substrate[13]. The quenching of magnetic moment is also accompanied by the alteration in the electronic structre of central metal atom.

Concerning the metal complexes and in particular porphyrins and phthalocyanines the 3d-orbital energy levels of the central metal atom present a splitting due to the ligand field within the macrocycle. This splitting depends on the oxidation state (3d occupancy) of the central atom and on the macrocycle different symmetries. See appendix-1 for more detail regarding splitting of 3d orbitals in different symmetries.

In this thesis the interfacial electronic properties of Iron transition metal complexes are also investigated. Due to the non plannar geometry of ferrocene, the interaction of Iron ion with underlying substrate is expected to be notably distinct as compared to planer tertrapyrrole complexes such as porphyin and phthalocyanine molecules.

1.2 Objectives and Approach

The objective of the research activity is to highlight the impact of molecular conformer, intermolecular interactions and molecular order on properties of technologically important transition metal complexes interfaces and thin films. As interfacial energy level alignment strongly influence charge transport at metal-molecule interfaces, we have selected specific metal-molecule interfaces in order to understand the impact of various physical processes involved in interfacial energy level alignment such as interfacial charge transfer, formation of interface dipole polarization effects, adsorption induced molecular distortions and type of central metal atom.

It has been observed that structural perturbations of the molecular conformers in the molecular layers and substrate symmetry lead to the alterations in the energy level alignment of the molecular orbitals. In order to achieve the above objective we have selected weakly interacting model system of CuOEP adsorbed on Au(111) so that impact of different molecular conformer can be highlighted. Further, the significance of intermolecular interactions on molecular order and energy level alignment is highlighted by utilizing NiOEP on Au(111) substrate so that impact of substrate induced perturbations can be minimized.

We focus our study on Inverse Photoemission characterization to enlighten the density of unoccupied electronic states energy positions of associated orbitals. The interest of such studies is due to the observation that empty orbitals are more sensitive to the intermolecular interaction due to their higher delocalization around the macrocycle. [17] These states exhibits notable

energy separation as compared to filled states induced by alterations in the molecular arrangements which makes inverse photoemission spectroscopy technique more sensitive to molecular perturbations. Inverse photoemission spectroscopy (IPES) has the potential to provide direct access to the unoccupied density of states for MPc molecule films absoprbed on metallic substates. Although, quantum yield of IPES is 10^{-5} times less than PES and electron beam can damage the molecular films. However, low current density allows reducing electron beam damage of organic molecules. Further, an efficient photon detector helps to enhance signal to noise ratio as well as energy resolution. Our IPES results are also complemented by Near Edge Absorption Fine structure and Photoemission taken at Synchrotron facilities (BESSY II, ELETTRA) and in campus (UPS and XPS), in order to get a complete framework of the studied systems. Combined photoemission and IPES analyses reveal the electronic structure of CoPc within 1 ML is different as compared to CuPc (weaker interaction) due to different hybridization of the Co with the Au substrates through the Co 3d orbital filling.

Metal-Molecules Interfaces	Objectives
CoPc and CuPc on Au(110)	To investigate impact of central metal atom on unoccupied density of states
NiOEP and CuOEP on Au(111)	To investigate impact of intermolecular interactions on unoccupied density of states
FeTPP-Cl on Gr/Ni(111), Gr/Pt(111) andHOPG	To study impact of intermediate graphene layer on interfacial electronic properties and dechlorination
Ferrocene on Gr/Ni(111) and HOPG	To explore interfacial electronic properties

Table 2

The electronic and magnetic properties of the adsorbed molecules may be significantly influenced by the metal-molecule interface and can be possibly modified by using an appropriate intermediate layer. In this context, graphene holds the potential to alter molecule-substrate hybridization effects thereby, notably influencing charge transport at interfaces and energy level alignment. It has been demonstrated that interfacial charge transfer can be significantly influenced by the introduction of graphene buffer layer between transition metal complexes adsorbed on metallic substrates.We investigate interfacial electronic properties for the deposition of FeTPP-Cl on Gr/Ni(111), Gr/Pt(111) and HOPG and explore various processes influencing

9

the interfacial charge transfer. These substrates are selected in order to highlight the impact of dissimilar graphene-substrate coupling and unique surface properties of these substrates on interaction with adsorbed molecules, which in turn control the interface dipole, energy level alignment, bond strength and adsorption geometry of the molecules. Despite of the fact that both graphene and graphite have same surface structure but HOPG is a layered carbon material and its surface is characterized by step edges and surface defects which can significantly impact molecule interaction as compared to graphene. Moreover, there are significant electronic and geometric structure differences in the HOPG basal and step edges planes [9]. HOPG has been found to interact weakly with tetrapyrrole complexes, therefore taken as reference substrate to compare interaction of FeTPP-Cl on Gr/Pt(111) and Gr/Ni(111).

The study also investigates the interconnection between structural and physical properties of transition metal complexes thin films by underscoring the significance of intermolecular interactions and molecular order. The research activity provides useful insights for the creation and control of functional molecular films, crucial for the technological applications of organic semiconductors.In addition, nature of substrate and its treatment significantly influences the properties of the metal phthalocyanine and porphyrin thin films by controlling the molecular orientation during growth. The relative orientation of the molecules is driven by the fine interplay between molecule–substrate and intermolecular forces governing the molecular and optoelectronic properties of the system .We have selected CoPc, FePc and ZnOEP adsorbed on SiOx/Si and ITO as model systems to highlight the impact of molecular order and intermolecular interactions on physical properties of thin films. In order to establish interconnection between structural and dynamical properties, a detailed analysis of molecular thin films crystallinity was performed with Grazing incidence X-ray diffraction (GIXRD). It has been shown that vibrational as well as dynamical properties investigated by visible Pump-Probe experiments have dependacne on molecular stacking.

Transition Metal complexes Thin Films	Objectives
ZnOEP/SiOx/Si ZnOEP/ITO	To establish Interconnection between structural and physical properties (vibrational and electronic) of Zinc Octaethylporphyrin Thin Films.
FePc, CoPc on ITO SiOx/Si and Au	To establish Interconnection between structural and physical properties(vibrational) of Cobalt phthalocyanine and iron phthalocyanine Thin Films.
CoPc on Gr/SiOx and Au(111)	To establish Interconnection between structural and physical properties(dynamical) of Cobalt phthalocyanine thin Films.

Table 3

References

[1] G.B. Blanchet, Y.-L. Loo, J.A. Rogers, F. Gao, C.R. Fincher, Appl. Phys. Lett. 82 ,2003, 463.

[2] W.Auwärter, D. Écija, F. Klappenberger and J. V. Barth Nature Chemistry volume 7, 2015, 105–120.

[3] M. Marks, A. Schöll, U. Höfer, Journal of Electron Spectroscopy and Related Phenomena 195, 2014, 263–271.

[4] Y.Bai, F.Buchner, I.Kellner, M.Schmid,F.Vollnhals,H.P.Steinrück, J.M.Gottfried, NewJ.Phys.112009, 125004.

[5] J.Uihlein, H.Peisert, H.Adler,M.Glaser,M.Polek,R.Ovsyannikov,T.Chassé, J.Phys.Chem.C118,2014, 10106–10112.

[6] S. Braun, W. R. Salaneck, and M. Fahlman Adv. Mater. 2009, 21, 1450–1472

[7] M. Campione, E. Fumagalli, L. Raimondo, A. Monguzzi, F. Meinardi, A. Sassella Chem. Mater. 2011, 23, 832–840.

[8] S.A. Krasnikov, N.N. Sergeeva, M.M. Brzhezinskaya, A. B. Preobrajenski, Y.N. Sergeeva, N.A. Vinogradov, A.A. Cafolla, M. O. Senge, A.S. Vinogradov, J. Phys.-Condens. Matter 20, 2008, 235207.

[9] G. Run-Da , Y. Shou-Zhen, W. Peng , C. Yu , Z. Yi and L. Shi-Yong 2013 Chinese Physics B 22,12,127304

[10] Z.-Y.Yang,C.Durkan,Surf.Sci.604(2010)660–665.

[11] S. Ditze, M. Röckert, F. Buchner, E. Zillner, M. Stark, H.P. Steinrück, H. Marbach, Nanotechnology 24, 2013, 115305.

[12] P. Gargiani, M. Angelucci, C. Mariani, M.G. Betti, Phys. Rev. B 81 (2010) 085412.

[13] P.Gargiani,M.Angelucci,C.Mariani,M.G.Betti,Phys.Rev.B81 (2010) 085412.

[14] M.Sauer, Phys. Status Solidi B, 12, 2012, 2408–2411.

[15] J. Zeng, Carbon 98, 2016, 607-612.

[16] Yongjun Gao, Dalton Trans., 2011, 40, 4542.

[17] M. Shibuta, K. Miyakubo, T.Yamada, and T. Munakata J. Phys. Chem. C 2011, 115, 19269–19273.

[18] A. Kumar, D. Naumenko, L. Cozzarini, L. Barba, A. Cassetta, M. Pedio, J. Raman Spectroscopy, 2018, 1-8.

[19] A. Alkauskas, L. Ramoino, S. Schintke, M. von Arx, A. Baratoff, H.-J. Gu1ntherodt, T. A. Jung J. Phys. Chem. B 2005, 109, 23558-23563

Chapter-2

Experimental methods and set up

In order to investigate interfacial electronic properties as well as bulk properties of transition metal complexes thin films and to achieve the objectives of the thesis as mentioned in first chapter, we have adopted multi-technique characterization approach. The studies presented in this thesis are a result of teamwork. The work cannot be achieved without the contribution and collaboration of all the authors, expert either in experiment, data analysis and theory.

I have contributed to all the data acquisition of electron (PES, IPES), Raman and absorption (NEXAFS, Optical pump-probe) spectroscopies and the sample preparation, i.e. substrate's surface and transition metal complexes thin film growth, presented in this thesis.

My work also involves collaboration with other expert researcher for data analysis and theoretical simulations, namely: detailed Grazing incidence X-Ray Diffraction (GIXRD) measurements and analysis, EXAFS measurements and analysis, NEXAFS fitting using MXAN code and theoretical DFT. In this section, a brief description of the experimental techniques and set up used in this thesis are discussed

2.1 Raman Spectroscopy

Raman spectroscopy is a widely used technique in various scientific fields due to its potential to deduce structure of molecules, isomerism, electrolytic dissociation, association, polymerization, hydrogen bonding and kinetics of fast reduction etc. Basic principle of Raman spectroscopy is based on the inelastic scattering of light by molecules. When light passes through a medium, a portion of it get scattered by molecules of the medium. Elastically scattered light is termed as Rayleigh scattering while, inelastically scattered light is known as Raman scattering. Raman scattering is the weaker as compared to Rayleigh scattering.[1] It is worthwhile to mention that about 99.999% of all incident photons undergo elastic Rayleigh scattering. Only about 0.001% of the incident light produces inelastic Raman signal with altered frequencies.

Inelastic scattering means that the frequency of photons in monochromatic light changes upon interaction with a sample. Photons of the laser light are absorbed by the sample and then re-emitted. Frequency of the re-emitted photons is shifted up or down in comparison with original monochromatic frequency, which is called the Raman Effect. This shift provides information about vibrational, rotational and other low frequency transitions in molecules. Raman spectroscopy can be used to study solid, liquid and gaseous samples. Classical theory can be utilized to explain the variation of frequency of scattered radiations. When a molecule is in an electric field E, the electron cloud and nuclei become polarized resulting in an induced dipole moment P. The size of the dipole moment induced by a field of magnitude E is given by the polarizability α of the molecule:

$$P = \alpha E$$

Light consists of oscillating electric and magnetic fields. For light of Frequency ν_0, the magnitude of the electric field may be written as

$$E = E_0 \cos(2\pi\nu_0 t)$$

Thus, the induced dipole moment oscillates in phase with the applied field:

$$P = \alpha\, E_0 \cos(2\pi\nu_0 t)$$

It is possible to expand α in terms of q_i the vibrational displacement coordinate of the ith normal mode. The classical normal mode vibration is

$$q_i = q_0 \cos(2\pi\nu_i t)$$

where ν_i frequency of normal mode i.

Then, based on classical theory, we can write

$$P = \alpha_0 E_0 \cos(2\pi\nu_o t) + \frac{1}{2}\left(\frac{\partial\alpha}{\partial q_i}\right)_0 E_0 q_i^0 \left[\cos\left(2\pi(\nu_o - \nu_i)t\right) + \left(\cos 2\pi(\nu_o + \nu_i)t\right)\right]$$

The first term in above equation represents the Rayleigh scattering. The last two terms oscillate at the sum and difference frequencies, and represent the anti-Stokes and Stokes scattering, respectively.[2] As show in Figure 1 below, in case of stokes lines the energy of the scattered radiation is less than the incident radiation, while for anti-stokes lines energy of the scattered radiation is more than the incident radiation. Due to unique energy separation of vibrational levels of the molecule, the measured values of wave-number provides a information about the vibrational energies of the molecule. The shift of these lines from Rayleigh line is found to be corresponding to the frequencies of the molecular vibrations and independent of the exciting radiation.
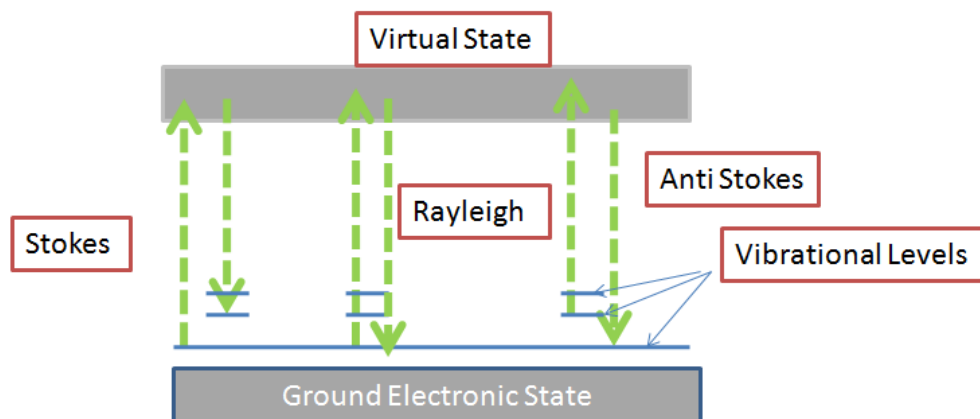
Figure 1 Schematic representation of transitions in vibrational states

For, a molecular vibration to be Raman active, there must be a change in the polarizability of the molecule during this vibration. This change can be considered as being a change in the shape of the electron cloud surrounding the molecule. The theory of Raman scattering shows that the amount of Raman scattering from a molecule is directly proportional to the intensity of the incident light and also to the fourth power of the frequency of the excitation radiation. Raman spectrum gives information about molecular symmetry which can then be used to determine the molecular configuration.

It is worthwhile to mention that intensity of the Raman scattering is seen to be proportional to the squared derivative of the polarizability of the molecule.

$$I_{\text{scatt}} \propto \left| \left(\partial \alpha / \partial q_i \right)_0 \right|^2 I_0^2$$

Importantly, polarizability must change linearly with vibrational motion of the molecule under study. It is evident that Raman intensity will be higher for greater change of α. There is a possibility that there is no raman scattering in case α does not change.[1]

In a typical Raman experiment, a polarized monochromatic light source (usually a laser) is focused into a sample, and the scattered light at 90° to the laser beam is collected and dispersed by a high-resolution monochromator. The incident laser wavelength (chosen such that the sample does not absorb, in ordinary Raman Spectroscopy) is fixed, and the scattered light is dispersed and detected to obtain the frequency spectrum of the scattered light. The scattered light is very weak ($<10^{-7}$ of the incident power), so that monochromators with excellent straylight rejection and sensitive detectors are required.

A Raman system typically consists of four major components:

1. Excitation source (Laser).

2. Sample illumination system and light collection optics.

3. Wavelength selector (Filter or Spectrophotometer).

4. Detector (Photodiode array, CCD or PMT).

A sample is normally illuminated with a laser beam in the ultraviolet (UV), visible (Vis) or near infrared (NIR) range. Scattered light is collected with a lens and is sent through interference filter or spectrophotometer to obtain Raman spectrum of a sample.

Experimental Set up

The measurements presented in the thesis were performed at CNR-IOM laboratory in the reflection geometry. CW laser with a wavelength of 532 nm (Cobolt Samba, 50 mW, bandwidth 1 MHz) was used as excitation source. 532 nm RazorEdge Dichroic™ laser-flat beamsplitter and

532 nm RazorEdge® ultrasteep long-pass edge filter were used to direct the light into microscope and cut Rayleigh scattered light, respectively. The laser power on the sample was controlled by the neutral density filter (Thorlabs) and kept at 100 µW. The acquisition time in all experiments was 600 s. Atomic Force Microscopy (AFM) measurements were performed in contact mode using Nanowizard II AFM (JPK), which allows to scan the sample in the range of 100x100x15 µm. CSG 01 Silicon probes (NT-MDT) with a force constant of 0.05 N/m and 10 nm tip curvature were used.

2.2 X-ray Photoemission Spectroscopy

Photoemission spectroscopy is a widely used technique for the investigation of the filled electronic structure of a wide variety of materials. The basic principle of the technique is based on the detection of an electron emitted from the sample by photoelectric effect. When sufficient energy is provided to the material under study, photoelectrons are ejected and kinetic energy of the emitted electrons is measured by the analyzer. In this way, information about the binding energy and wave vector can be gathered since the kinetic energy of emitted electrons is a function of binding energy (B.E.), which, in turn, is element and environment specific .There are two primary de-exciation processes namely Auger process and fluorescence. The kinetic energy of photoelectron ($K.E._{XPS}$) can be related to binding energy $B.E._{XPS}$ as follows. Here WF represents work function of analyzer (define Work Function). E_{Ph} is incident photon energy.

$$K.E._{XPS} = E_{Ph} - WF - B.E._{XPS}$$

The information about the binding energy provides useful information on the chemical environment and oxidation state of the atom under study. This can be achieved by measuring the chemical shift i.e., the deviation of the binding energy from the free atom value.
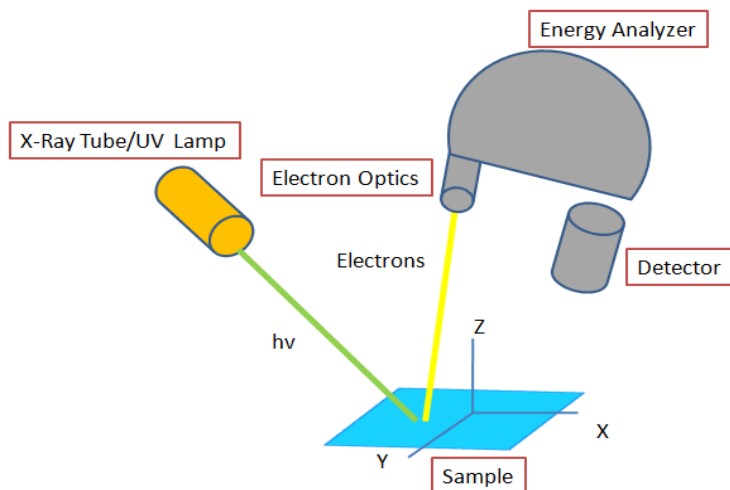

Figure 2: Schematic represntation of PES set up

The figure 2 shows the schematic representation of photoemission set up. Typically a photoemission instrument consists of an X-ray source (lamp or synchrotron), an electron extraction optics, an energy filter and adetection system. The size of the analysis area was defined by the aperture selection of the focus Analyzer energy resolution (ΔE/E) was determined by the choice of pass energy and selected aperture.[3]

The so called 3-step model is usually applied to interprete the Photoemission process [4]. X-ray Photoemission process can be divided into three parts (i) excitation of the core electron from material (ii) electron transfer toward the surface and (iii) propagation of the electron from the surface to the vacuum. A fundamental assumption in the PES theory is the sudden approximation in which the response of the system upon the creation of the hole is instantaneous and there are no interactions between the emitted electron and the system itself. [4]
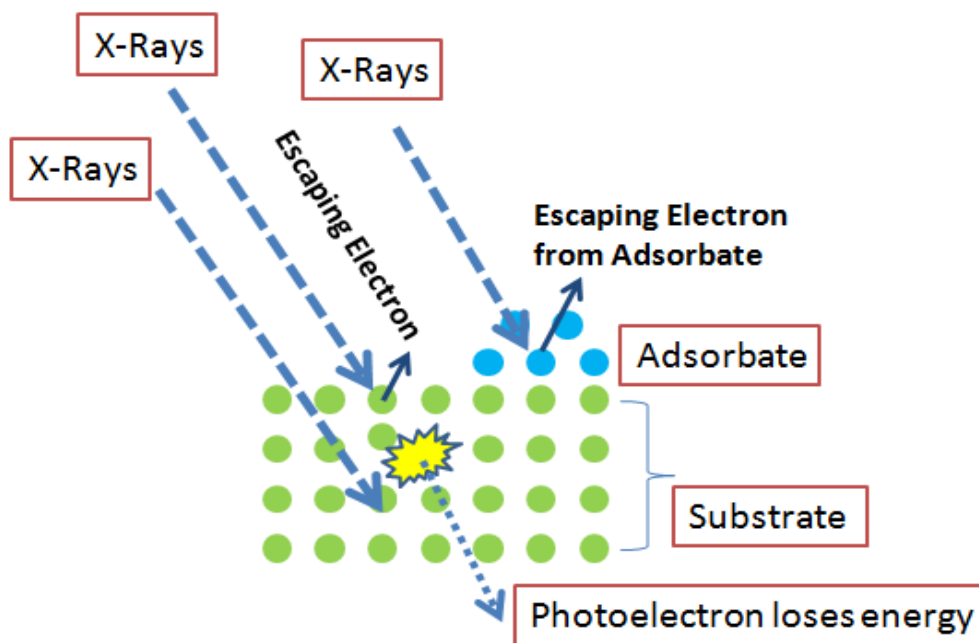
Figure 3: Schematic represenation of photoelectron emission from a solid materialand the surface adsorbate layer

The advantage of using synchtron radations as compared to laboratory sources for XPS measurements is the higher resolution and accurate dtermination of chemical shifts.In this thesis we intend to utilize photoemission experiments in order to investigate chemical shift and change of oxidation state of adsorbed molecules so that metal-molecule interactions can be revealed. Ultraviolet Photoemission Spectroscopy (UPS) a photoemission experiement performed using gas discharge lamp as source are normally related to valence band measurements.

It is important to note that PES detects only those electrons that have actually escaped into the vacuum from the surface of sample, above the Vacuum level. These photo-emitted electrons are

those that originated from within the top few nanometres of the material. The sensitivity depth depends on the Kinetic Energy, i.e. on the impinging photon energy. All of the deeper photo-emitted electrons, which were generated as the X-rays penetrated 1–5 micrometers of the material, are inelastically lost prior to escape.[5] Figure 3 shows a schematic representation of various processes that can occur when X-rays interact with the sample under study. Photoelectrons jected from substrat surface are also influenced by the presence of adsorbate on ts surface, thereby decreasing the intensity of signal from the substrate. The attenuation of substrate intensity with increasing adsorbate thickness can be utilized to estimate the thickness of adsorbate coverage.

As shown in figure 3, the ejected electrons may lose energy due to inelastic scattering. These inelastically scattered electrons provide the spectral background in the PES spectrum. It is important to mention that the probability of electron interaction with matter is higher as compared to photons. Path length of the photons is few micrometers, while the path length of the electrons is of the order of tens of angstrom. If we consider a volume element of the sample of thickness dz at a depth z beneath the sample surface. The photoelectrons emitted at an angle θ with respect to the normal to the sample surface enter the detector and contribute to the spectrum.[9] The probability that a photoelectron will escape from the sample without losing energy is:

$$P(z) = \exp(-z/\lambda \sin \theta)$$

where λ is the photoelectron inelastic mean free path. Suppose that one layer of thickness dz, by photoionization produces the intensity of photoectrons dI and assuming that the thickness of the sample is much larger than few anstrom then we can calculate the intensity of the electrons emitted from the depth d by following integral:

$$\int_0^d dI = \int_0^d \alpha \exp(-z/\lambda \sin \theta) dz$$

where α is a coefficient depending on photoemission cross section incident X-ray flux, angle between photoelectron path and analyser sample axis.

The intensity of electrons I_d emitted from all depths greater than *d* in a direction normal to the surface is given by the Beer-Lambert relationship.

$I_d = I \exp(-d/\lambda \sin\theta)$

Here λ represents the inelastic mean free path.
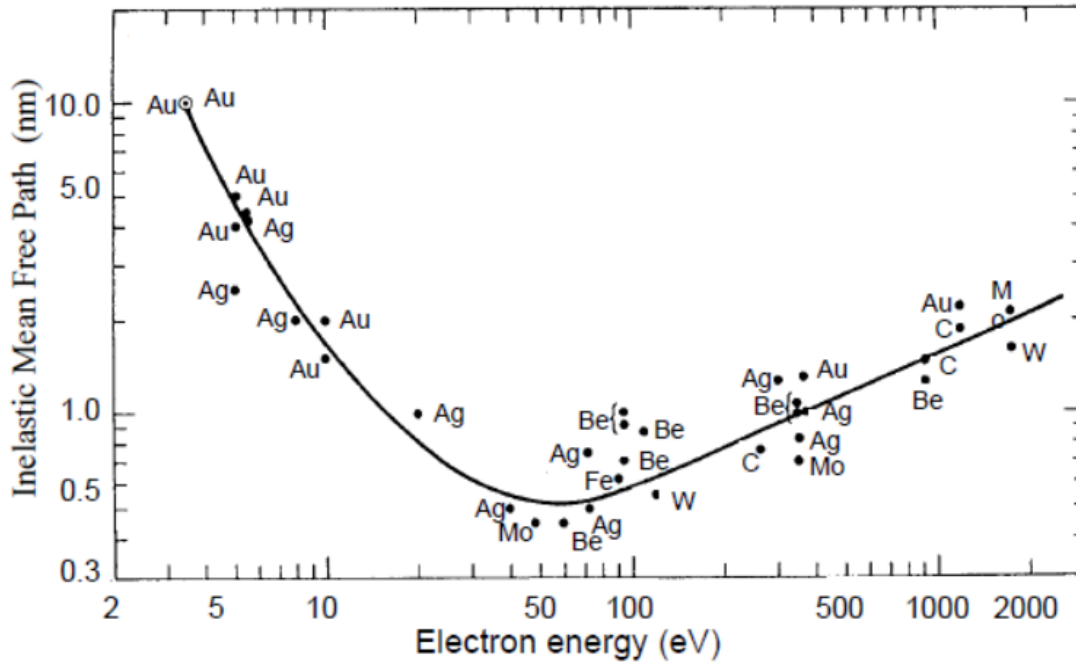
Figure 4: Measured electron mean free path as a function of their kinetic energy for various metals are represented with black dots. The universal curve of inelastic mean free λ of the electron is a best fit trough the measured points

The photoemission transition probability w can be calculated for N electron system in the ground state ψ_i to probable final state ψ_f using Fermi Golden rule. If E_f and E_i represents the energies of final and initial states respectively, then photoemission intensity is proportional to

$$w \propto 2\pi/\hbar \ |\langle \psi_f | H | \psi_i \rangle|^2 \delta(E_f - E_i - hv)$$

Considering Dipole and sudden approximations, the equation reduces to

$$w \propto |\langle \psi_f | \epsilon \cdot \mu | \psi_i \rangle|^2 \propto |\epsilon \, D_{fi}|^2$$

Here , D_{fi} stands for matrix element. It determines how the system will interact with an electromagnetic wave of a given polarization, while the square of the magnitude gives the strength of the interaction due to the distribution of charge within the system. Here ϵ is aunitary vector in the direction of light propagation and μ is a dipole operator. Measured photoelectron intensity also depends on atomic density of the element/cm^3 , detection efficiency, differential cross section, Probability of emission from the solid and Photon flux/cm^2s.[5]

The binding energy E_B of an electron in an atom is characteristic of each element. This chemical sensitivity is one of the most striking features of XPS (core level) which can be used for the

19

analysis of the elements in a sample. In particular, different types of bond determine the so-called chemical shift [3], that is, the deviation of the binding energy from the free atom value. In this way is possible to distinguish atoms depending on their chemical environment, for instance, nonequivalent atoms within a molecule or elements bonded to different atomic species. The binding energy may be regarded as the energy difference between the initial and final states after the photoelectron has left the atom. Because there is a variety of possible final states of the ions from each type of atom, there is a corresponding variety of kinetic energies of the emitted electrons. It is important characteristic as the satellite peaks can provide useful information about plasmon loss , shake up and shake off processes in the sample. [4]

Experimental Set up

PES measurements were performed at BACH beamline of Elettra synchrotron facility. The beamline offers high intensity and brilliance photon beam in the energy range of 35 to 1650eV with control of light polarization. The radiation source is based on two APPLE-II elliptical undulators that are used alternatively in order to optimize the flux. Beamline operates with four different interchangeable spherical gratings. The first three gratings allow resolving powers of 20000-6000, 20000-6000 and 15000-5000 in the energy ranges 35-200 eV, 200-500 eV and 500-1600 eV respectively. In addition, a fourth grating operates in the 300-1600 eV range providing higher flux with reduced resolving power (10000-2000), suitable for x-ray emission experiments. The flux in the experimental chamber ranges between 1.2×10^{12} photons/s at 125 eV and 6×10^{10} photons/s between 900 eV and 1250 eV.

Moreover PES experiments were also performed in laboratory source at CNR-IOM. Measurements were performed in normal emission geometry, using a hemispherical electron energy analyzer, and a conventional Mg Ka X-ray source (hv: 1253.6 eV) and a He lamp (hv: 40.8 eV). The overall energy resolution for the XPS and UPS spectra were, respectively, ~0.8 and ~0.2 eV.

2.3 Inverse photoemission Spectroscopy

IPES technique is an electron in , photon out technique which can provide information about unoccupied density of states. Figure 5 shows the schematic representation of IPES experimental set up. An electron gun provides a collimated beam of low energy electrons(5to 20eV). These electrons couple to unoccupied states within the material and radiate energy in the form of photons. These photons are then detected by Geiger-muller counter which act as a band pass detector and can count photons of particular energy depending on the type of gases used to build the counter. The current pulses are the fed to the preamplifier to convert the current pulse to a voltage pulse shapedTTL. These pulses are counted by the counter and fed to the computer by DAQ.
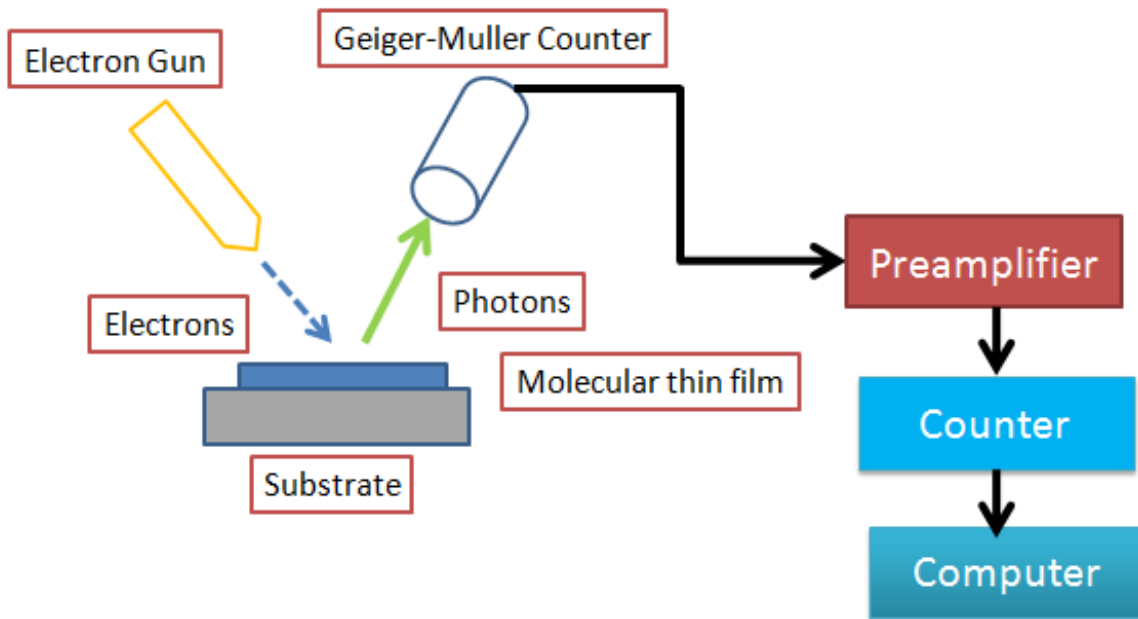
Figure.5 Schematic representation of IPES experimental set up

A three step model can be adopted to understand the inverse photoemission process. [6] As discussed above a collimated beam of electrons of know energy produced by the electron gun impinges onto the sample . These electrons then couples to an unoccupied state above the Fermi edge energy. In the second step the electron decays as shown in fig below emitting photons. There is a finite probability that electrons decay non-radiatively loosing energy through inelastic collisions. In the next step emitted photons are detected by Geiger-Muller counter.

If the energy of incoming electrons is known then detection of photons can provide information about the final state using the relation

$$E_f = E_i - h\nu.$$

In the isochromat mode the energy of the electron beam can be varied while only one photon energy,hv is measured. The intensity of the collected photons will then peak whenever

$$E_i = E_f + h\nu$$
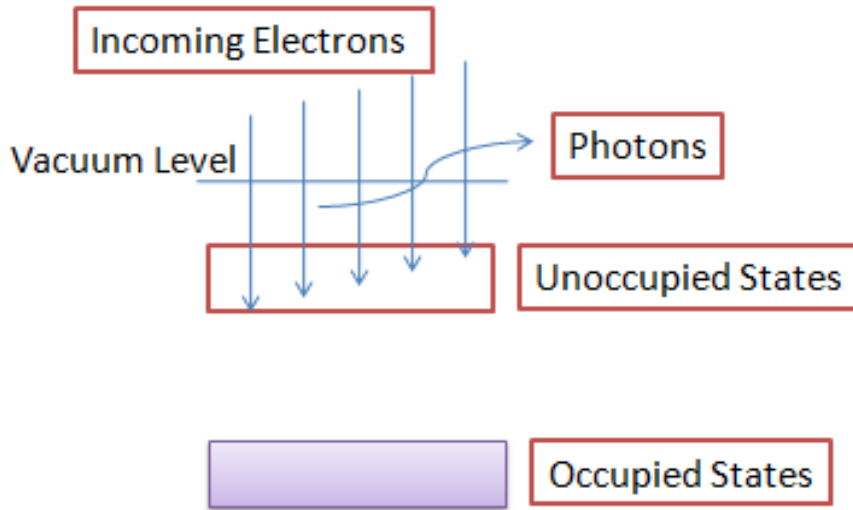
Figure 6 Isochromat mode of photon Detection [ref. 7]
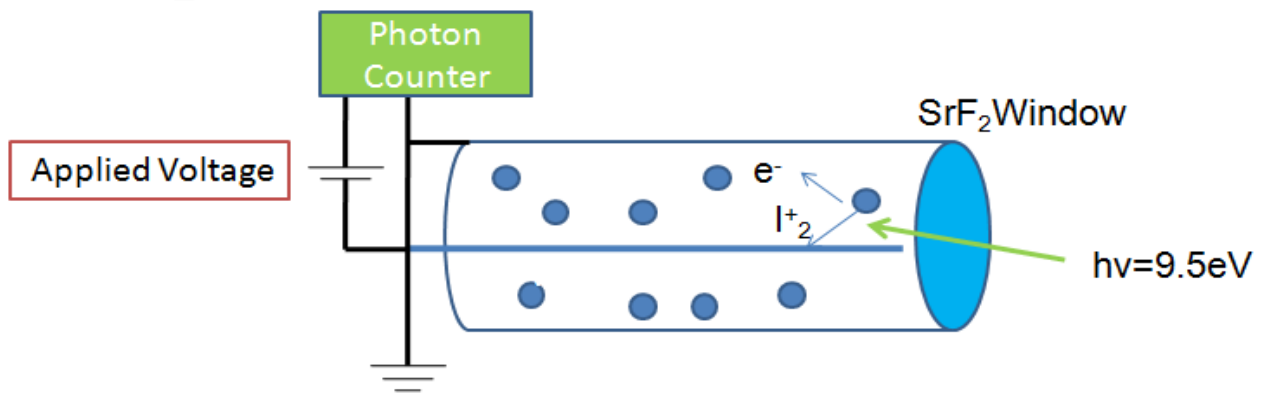
Figure 7 Photon Detection using Geiger-Muller counter

Geiger-Müller tube is filled with a mixture of Iodine and helium gases. The presence of iodine as quenching gas is necessary to improve the dead time as well as it improves count rate. The ideal G–M tube should produce a single pulse for every single ionizing event due to radiation. It should not give spurious pulses, and should recover quickly to the passive state, ready for the next radiation event. However, when positive iodine ions reach the cathode and become neutral atoms by gaining electrons, the atoms can be elevated to enhanced energy levels. These atoms then return to their ground state by emitting photons which in turn produce further ionisation and thereby spurious secondary discharges. Some form of quenching of the ionisation is therefore essential to reduce the dead time and protect the tube. As shown in figure SrF_2 window together with I_2 acts as a band pass filter with maximum at 9.5 eV.
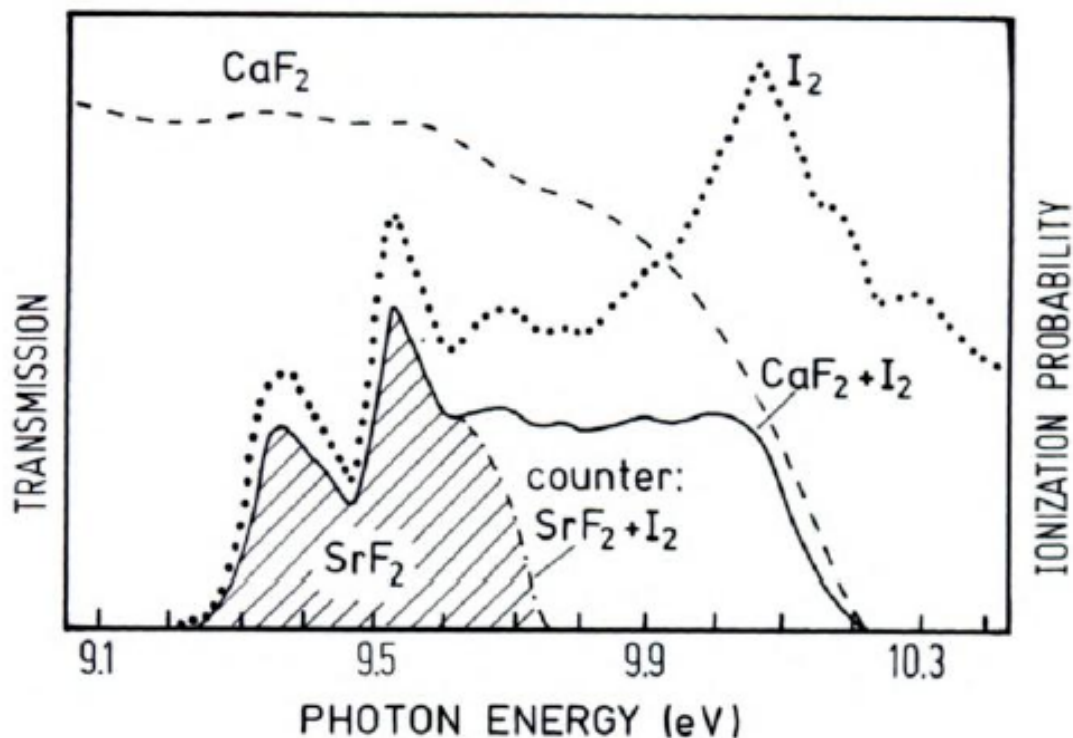
Figure. 8 The transmission of the SrF$_2$ window and the ionization probability spectra
of I$_2$ gas of the IPES detector. [Rporduced from Ref.7]

The count rates for IPES and PES can be compared by considering the ratio of their cross sections as shown below. Here $\lambda_{e\text{-}}$ and λ_{hv} are the wavelengths of the incident electrons and photons, respectively. It can be calculated that cross section of IPES is 2×10^{-5} times higer than PES for electrons of 10eV energy. In other words the count rate of IPES is lower than PES by many orders of magnitude. [7]

$$\frac{\left(\frac{d\sigma}{d\Omega}\right)_{\text{IPES}}}{\left(\frac{d\sigma}{d\Omega}\right)_{\text{PES}}} = \left(\frac{\lambda_{e-}}{\lambda_{hv}}\right)^2$$

The use of a Geiger Müller detector has the advantage of a very high detection efficiency (>85%).

Experimental set up

The normal incidence IPES measurements were performed in the UHV system of IOM SIPE laboratory by using an Erdman-Zipf electron gun, with the electron beam divergence $< 3°$. photons emitted from the sample surface are collected by a Geiger- Müller detector with a He-I$_2$

23

gas mixture and a SrF$_2$ entrance window filtering photons at energy hv = 9.5 eV. Current on the sample was < 1µA. The overall resolution was < 300 meV, as measured by the Fermi level onset of a clean ta foil. Spectra presented in this thesis are normalized at each point to the incident electron beam current.

2.4 Near-edge X-ray absorption fine structure

Near-edge X-ray absorption fine structure (NEXAFS) spectroscopy can provide useful information about the element specific unoccupied states together with the average orientation of adsorbed molecules on substrates. The technique involves measurement of absorption of X-rays by core shell, whith electrons promoted to anti-bonding molecular orbitals. This technique is particularly useful for organic layers because C-C 1s-π* transitions are quite strong and well-resolved. The NEXAFS technique requires the use of synchrotron radiation as the X-ray photon energy has to be varied near the ionization edge of the specific elements . The resulting spectrum provides a map for the bonding environment of specific atomic species corresponding to intra-molecular and extra-molecular (substrate atoms) neighbors.
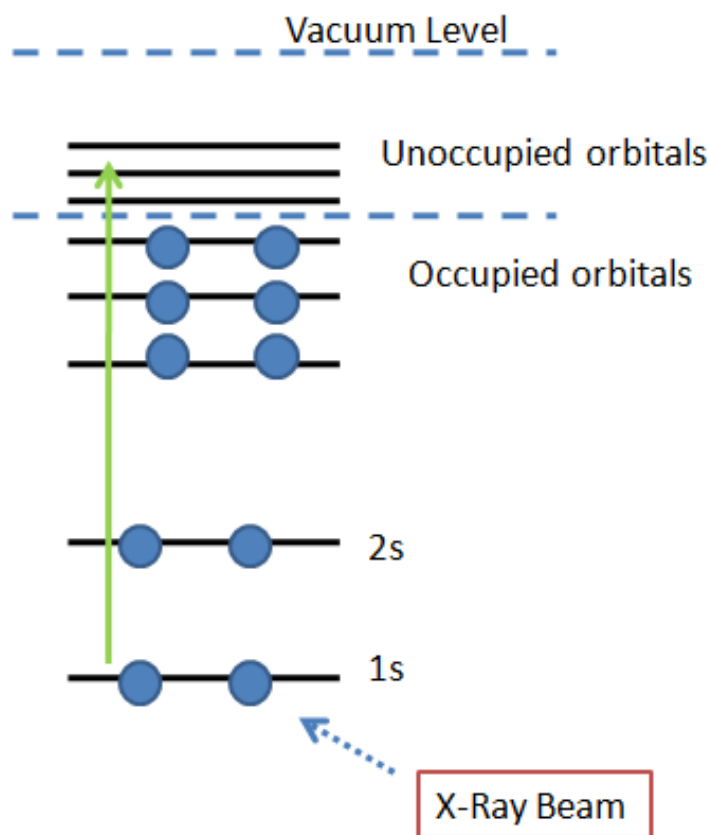

Figure 9 Schematic representation of X-ray absorption process

One of the advantages of using NEXAFS is the ability to provide information about the molecular orientation for molecular thin films. It is due to the highly directional nature of the bonds corresponding to the excited molecular orbitals and to the linear polarization of synchrotron radiation, typically used in organic layer characterization (circular polarization is mandatory in case of XMCD measurements for magnetic measurements). Figure 10 shows a diatomic molecules with two different orientations of its molecular axis. The molecular orientation can be obtained by monitoring the intensity variation of resonances as a function of X-ray beam incidence angle.

As shown in figure 9 the photo-absorption process takes place when the incident photons hit the sample substrate resulting in the creation of a photoelectron and a core hole. There is a probability that the resulting hole is filled by another electron and the corresponding excess in energy is dissipated either radiatively by the emission of a fluorescent photon. Second possibility is the generation of an Auger electron resulting in non-radiatively decay. Both possibilties are a direct result of the core hole created in the X-ray photoabsorption process and thus provide a basis to determine the absorption cross section.

The resonance intensity in case of σ* molecular orbital final state is given by

$$I_{if}(\sigma^*) \propto |\epsilon \cdot \widehat{e}_z|^2 \propto \cos\theta^2.$$

The σ* resonance will be greatest for ε along the molecular axis and lowest when ε is perpendicular to it. The π* has opposite angular dependence than σ* . Considering the above molecular geometry equation σ* resonance intensity will be higher for grazing incidence (Fig.10) and π* resonances will be higher for normal incidence (Fig.10)
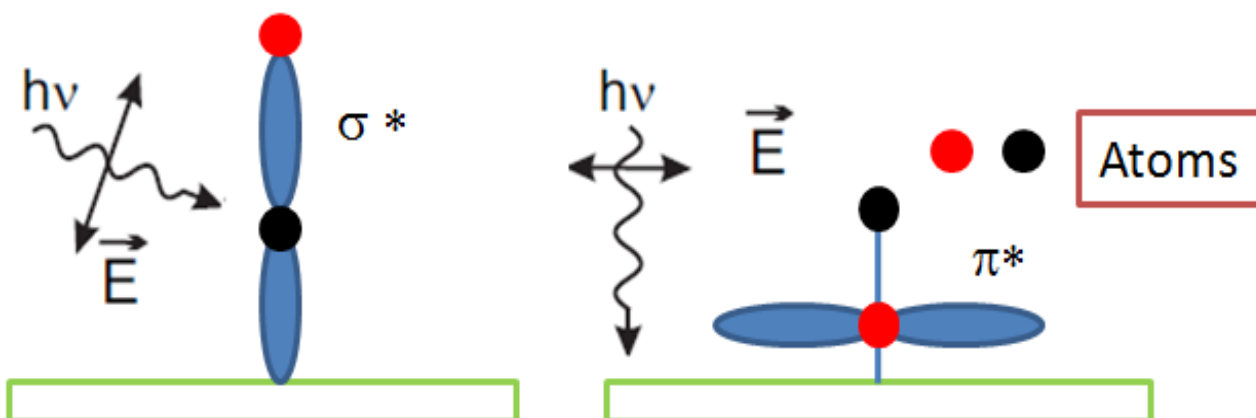

Figure 10 Schematic represntation of polarization of light with repsct to orbital orintation

NEXAFS spectra can be measured in many modes. In principle, the different dissipation processes can be used for the detection. It is necessary to note, however, that for low-Z elements (C, N, O) the Auger electron yield is much higher than the fluorescence yield (FY). The simplest measurement mode is total electron yield (TEY), which measures the charge compensation current through the grounding path. Other electron-yield modes typically measure electrons ejected from the sample surface using an electron detector. With an appropriate high-pass kinetic energy filter the electron-yield signal can be adjusted to include only unscattered Auger electrons (AEY), or to include some Auger electrons that have been inelastically scattered from deeper layers within the sample (PEY). The PEY mode permits a near-surface depth profiling capability with adjustment of the energy filter bias. While all of the NEXAFS electron yield modes are surface-sensitive (about 0.5 in AEY, 5-10 nm in PEY and TEY), it is also possible to measure NEXAFS by bulk-sensitive fluorescence yield (FY) (sensibility depth ≥ 100 nm).

FY experiments, however, can be experimentally complex because scattered incident light must be separated from the fluorescence signal.

The average orientation of the π^* in thin molecular films [8] can be quantified using a dichroic ratio, R, defined as

$$R = (I (90°) - I (0))/(I (90°) + I (0°))$$

where $I(\theta)$ indicates the intensity at an angle of incidence with respect to the surface plane of For an azimuthally symmetric system, with the transition dipole tilted from the surface normal by an angle θ,

$$R = \frac{P(1-3\langle\cos^2\theta\rangle)}{2(1-\langle\cos^2\theta\rangle)-P(1-3\langle\cos^2\theta\rangle)}$$

where P is the polarization purity of the beam line, R can vary from 0.7, for a perfectly edge-on conjugated plane to 1.0 for a perfectly plane-on system (such as highly oriented pyrolytic graphite). It is worthwhile to mentiona that parameter R is more complex and exhibits depedance of substrate symmetery.[8]

The position of σ resonances can provide information about intramolecular bond lengths, while location and intensity of π^* resonances provide information about the bond hybridization. The X-ray absorption measurements were performed at BACH beamline of Elettra Synchtron facility both in total electron yield and partial electron yield.

2.5 Pump probe Experiments

Figure 11 shows the basic principle of pump-probe spectroscopy. Generally, a femtosecond laser source is used to produce Pump and probe pulses with certain delay time. The pump pulse excites the sample and leaves the sample to evolve in time and another pulse is used to

26

investigate the change induced by the pump pulse. The energy of pump and probe together with time delay between probe and pump can be changed to analyze the excited state dynamics of the sample.

In the visible pump probe experiment it is important to know about the linear absorption of sample under investigation so that appropriate pump wavelength can be selected for excitation of the sample. It is possible to get the spectrum in reflection or transmission mode depending on the sample characteristics and experimental setup. The pulse duration of pump and probe pulses used in the pump-probe experiments are crucial as they govern the time resolution of pump-probe spectroscopy. The time resolution can reach to femtosecond scale with Femtosecond laser pulse. It makes pump-probe spectroscopy a unique tool to investigate fast dynamics processes occurring in the sample after excitation by pump pulse.

The pump-probe experiments have been performed at "Ultrafast Laser Micro and Nano processing" laboratory of Foundation for Research and Technology – Hellas research facility at Crete Greece. Figure 12 shows the schematic representation of experimental set up. Dynamical properties have been investigated by the time resolved femtosecond pump and probe experiments.
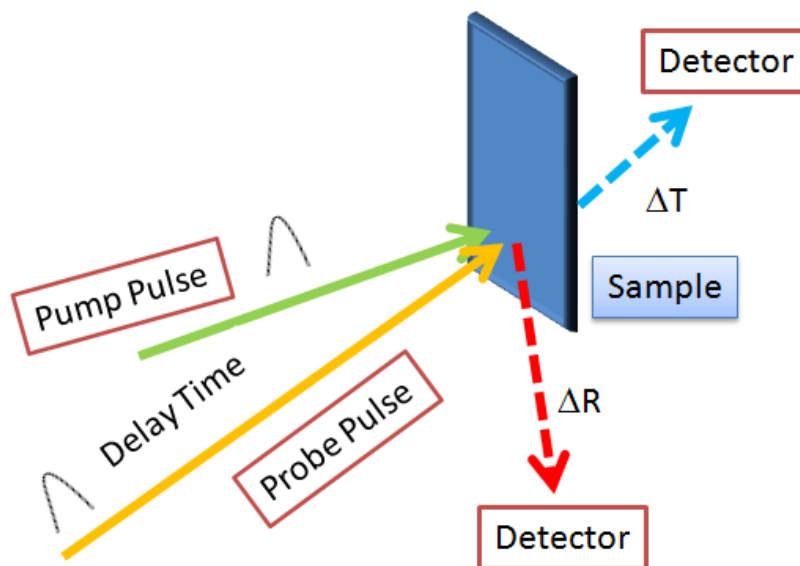
Figure 11 Principle of Pump-Probe Experiment

Femtosecond laser pulses were generated using a Ti: Sapphire oscillator170 femtosecond pulses with a repetition rate of 82 MHz then passed a regenerative amplifier. At the output, the repetition rate was reduced to 1 kHz. The pump wavelength was 512nm while a range of wavelengths from 450nm to 1100nm was used as probe pulse.

The delay time between pump and probe was controlled by computer. The measurements were performed at room temperature. The reflected probe beam was directed onto optical fiber. The

measurements were then performed as a function of pump-probe delay time using charge-coupled device camera (CCD).

As shown in Figure 12 a portion of pump pulse is sent into the optical parametric amplifiers (OPAs). It generated a continuum ranging from 450nm to 1100nm. We determined differential reflection of the samples for each delay time. The time delays were varied between 0 to 50ps. The reflected intensity of the pump pulse was measured with excitation of sample by the pump pulse and without excitation as a function of probe energy.
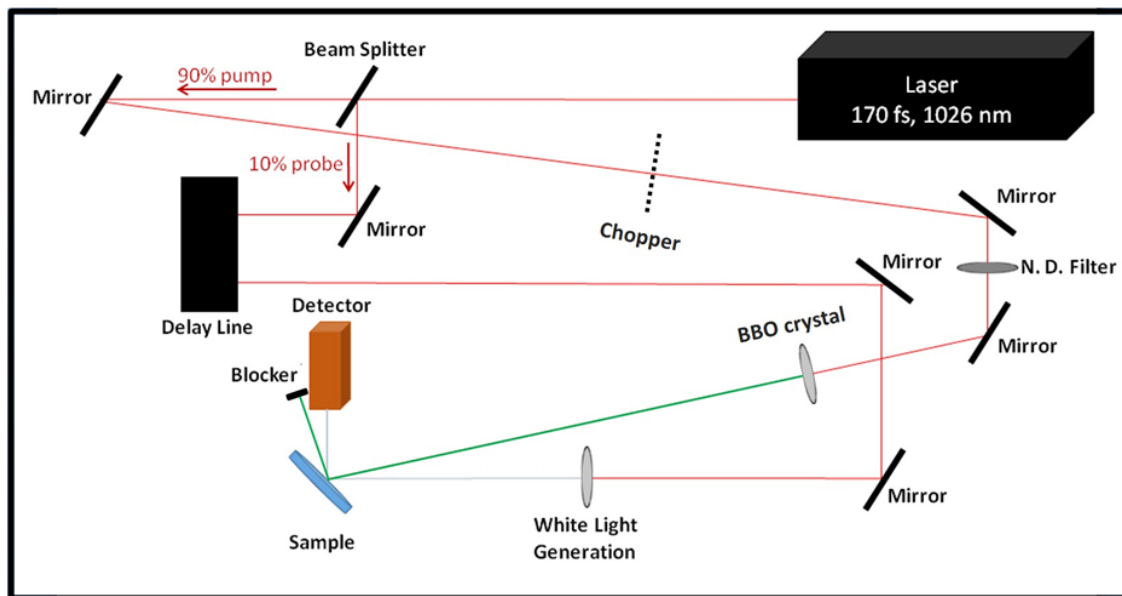
Figure 12 Experimental set up for pump-probe experiments at FORTH research facility Crete, Greece

2.6 Surface preparation

The Ni(111) single crystal was cleaned by several sputtering–annealing cycles (15min.,2Kev and flash annealing at 600°C). Graphene was obtained by exposing the sample, which was kept below 600 °C to 6000 L of ethylene (1 L = 10^{-6} torr·s). The quality of epitaxial graphene was monitored using LEED and valence band analysis. Graphene on Pt(111) was grown by adopting standard cleaning procedure for Pt(111) and then exposing the sample to ethylene atmosphere at about 1000K.

HOPG was freshly cleaved before introducing into the chamber and subsequently annealed at 1100 K. Gr/SiOx substrate was prepared following a well established (transfer method) protocol.[1] Au(110) and Au(111) substrates were cleaned by multiple cycles of sputtering and annealing following standard procedure.

2.7 Transition metal complexes Thin film Deposition

Porphyrin and phthalocyanine molecules were deposited from a quartz crucible at the respective sublimation temperatures (MPc Tsubl≈580 K, MOEP≈500 K, MTPP ≈550 K) onto the substrate held at room temperature (RT) under UHV with in a pressure of about $2x10^{-9}$mb. The film thicknesses were estimated by measuring the XPS (laboratory source or synchrotron facilities) and calculating the ratios of the normalized area of the core level peaks corrected by photoemission cross sections. In case of IPES measurement the molecular thickness was estimated after calibration and characterization of a single ML after annealing of a multilayer by WF and LEED and subsequent XPS measurements in the lab chamber, after *in vacuum* transfer.

Ferrocene deposition was performed at a substrate temperature of 120K onto the substrates. Multilayer was measured at this temperature. A desorption of the multilayer took place at about 250K.

Reference

[1] S.K. Freeman "Applications of Laser Raman Spectroscopy", John Wiley and Sons, New York 1974.

[2] D.A. Lon "Raman Spectroscopy", Mc Graw-Hill, Great Britain 1977.

[3] D P Woodruff and T A Delchar. Cambridge University Press, 1994.

[4] Stefan Hüfner. Photoelectron spectroscopy. Springer, 2003.

[5] C S Fadley, S B M Hagstrom, M P Klein, and D A Shirley. Chemical effects on core-electron binding energies in iodine and europium. The Journal of Chemical Physics, 48:3779, 1968.

[6] J. C. Fuggle and J. E. Inglesfield, Topics in Applied Physics: Unoccupied Electronic States (Springer-Verlag, Berlin, 1992.

[7] 2V. Dose, Prog. Surf. Sci. 13, 225 1983; N. Smith, Rep. Prog. Phys. 51, 1227 ,1988; F. J. Himpsel, Surf. Sci. Rep. 12, 3, 1990.

[8] Jochim Stöhr, NEXAFS Spectropy, Springer Series in Surface Sciences, Berlin 1992

[9] J.F. Watts, X-ray photoelectron spectroscopy, Surface science techniques, Leicesterhier, Pergamon, UK, (1994)

[10]Shukla, A.K., S. Banik, and S.R. Barman, Current Science, 2006. 90, 4, 490-496.

[11] Cahen, D., A. Kahn, and E. Umbach, Materials Today, 2005. 8, 32-41.

[12] Himpsel, F.J. and T. Fauster, Journal of Vacuum Science and Technology A, 1984. 2, 815-821.

[13] Dose, V. and G. Reusing, Applied Physics, 1980. 23, 131-134.

[14] Roentgen, W.C., Physik. Med. Ges., 1895. 137,1, 1- 29.

[15]. Duane, W. and F.L. Hunt, Physical Review, 1915. 6, 2 ,166-172.

[16]. Smith, N.V., Reports on Progress in Physics, 1988. 51, 9, 1227-1294.

[17]. Pendry, J.B., . Journal of Physics C: Solid State Physics, 1981. 14, 9, 1381-1391

[18] M.C. Biesinger, L.W.M. Lau, A.R. Gerson, R.St.C. Surface Science, 2010, 257, 2717–2730.

Chapter-3

Metal Phthalocyanine thin films: Influence of d level occupancy and intermolecular interactions on physical properties

3.1 Introduction

Metal Phthalocyanine (MPc) molecules exhibit good photostability and organize in well ordered crystalline structures on metallic substrates by thermal evaporation.[1] These molecules are an attractive choice for novel electronic devices such as thin film transistors, organic light-emitting diodes, organic photovoltaic and liquid crystalline materials.[1-4] Moreover, open shell MPcs show paramagnetic properties due to the 3d central metal states occupancy and exhibits potential for spintronic applications.[5] Therefore, thorough understanding of their occupied as well as unoccupied electronic properties is important to realize functional molecular devices based on MPc molecules. We focus this segment on Inverse Photoemission Spectroscopy (IPES) investigations in order to enlighten the role of metal 3d orbital occupancy on the MPc unoccupied electronic states and in their interaction process.

It has been established that isolated transition MPc molecules (MnPc, FePc, CoPc, NiPc, CuPc, and ZnPc) exhibit a D_{4h} symmetry in their molecular structure. The D_{4h} crystal field of isolated Pc macrocycle lifts the degeneracy of the 3d transition metal orbital giving rise to the sequence of orbitals depicted in Figure 1.
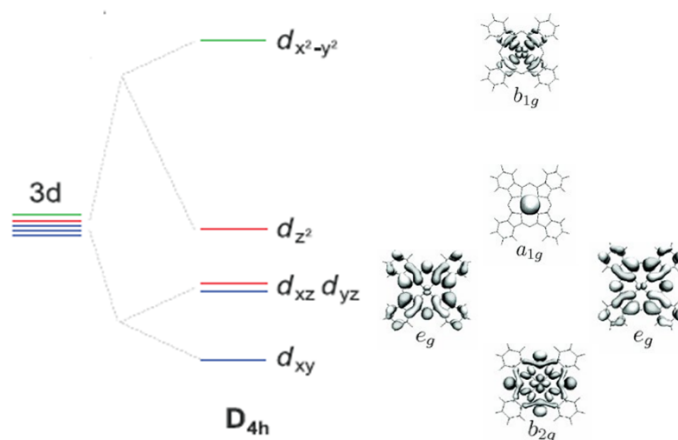

Figure 1 Schematic representation of d- level splitting in the D_{4h} symmetry [6]

Molecule	Ground state Electronic configuration[6]	Spin[6]
ZnPc(d^{10})	$b^2_{1g} a^2_{1g} e^4_g b^2_{2g}$	0
CuPc(d^9)	$b^1_{1g} a^2_{1g} e^4_g b^2_{2g}$	½
NiPc(d^8)	$b^0_{1g} a^2_{1g} e^4_g b^2_{2g}$	0
CoPc(d^7)	$b^0_{1g} a^1_{1g} e^4_g b^2_{2g}$ or $b^0_{1g} a^2_{1g} e^3_g b^2_{2g}$	½
FePc(d^6)	$b^0_{1g} a^1_{1g} e^3_g b^2_{2g}$	1
MnPc(d^5)	$b^0_{1g} a^1_{1g} e^3_g b^1_{2g}$ or $b^1_{1g} a^2_{1g} e^2_g b^2_{2g}$	3/2

Table-1

Table 1 summarizes the ground state configurations and spins as studied using soft X–ray absorption spectroscopy.[6] In spite of theoretical calculation contradictions related to MPc ground state configuration, some conclusions can be drawn based on soft X-ray absorption studies performed on MPcs thin films. Most of studies agree that b_{1g} state with d_{x2-y2} character is highest in energy as compared to other central metal atom associated orbitals in D_{4h} symmetry. [6] As shown in Table-1, holes occupy b_{1g} orbital in case of CuPc and NiPc. However, situation becomes interesting for CoPc as hole may occupy e_g or a_{1g} orbitals. A combined theoretical and experimental approach suggest that third hole occupies a_{1g} orbital.[6] As the nature of MPc frontier orbitals can be determined due to dependence of X-ray absorption resonance intensity on orbital symmetry.

Although, considerable efforts have been made based on theoretical DFT calculations in the literature,[7,8,9] there is still ambiguity regarding the ground state electronic configuration, energy level sequence and occupation of 3d character orbitals. The choice of exchange-correlation functional is crucial for the calculations of electronic structure of MPc molecules. Figure 2 demonstrate the energy position of few significant orbitals of CuPc and CoPc obtained by using various exchange-correlation functional [8a,b]. It is reported that although, various functionals are suitable to describe the geometry of the molecule but differ significantly in the predicted electronic structure. Moreover, the ordering of orbital and identity of HOMO and LUMO is notably altered as shown in Figure 2.
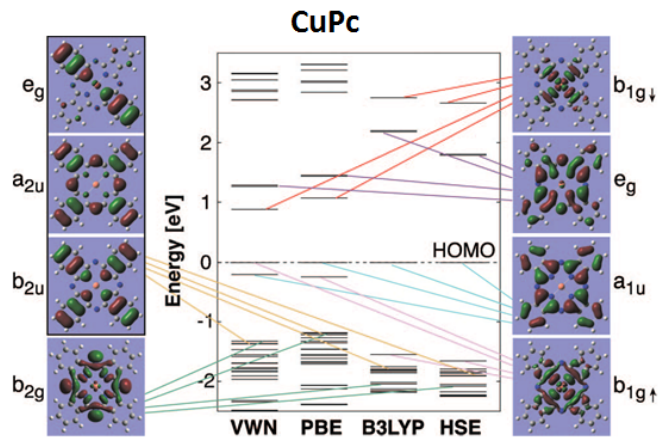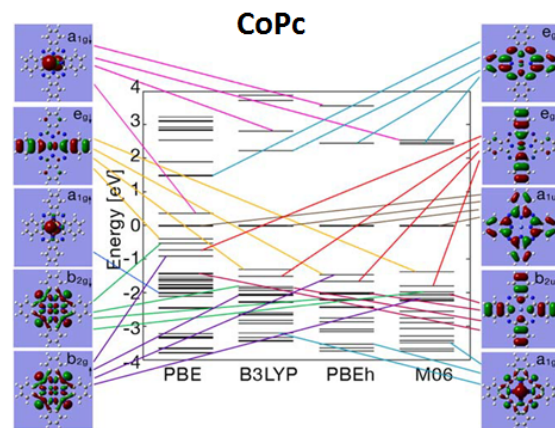
Figure 2(a)   Figure 2(b)

Figure 2 Energy levels and ordering of selected MOs calculated with different exchange-correlation functionals of a) CuPc, b) CoPc, All spectra were shifted to align the highest occupied molecular orbital (HOMO) at 0 eV. (Reproduced from ref. 8)

In this thesis, we have performed IPES measurements on MPc TFs and compared with X-ray absorption studies in order to rationalize unoccupied density of states assignments. Figure 3 shows our IPES data taken at normal incidence of different MPc TF. The overall resolution of the spectra is 250 meV.
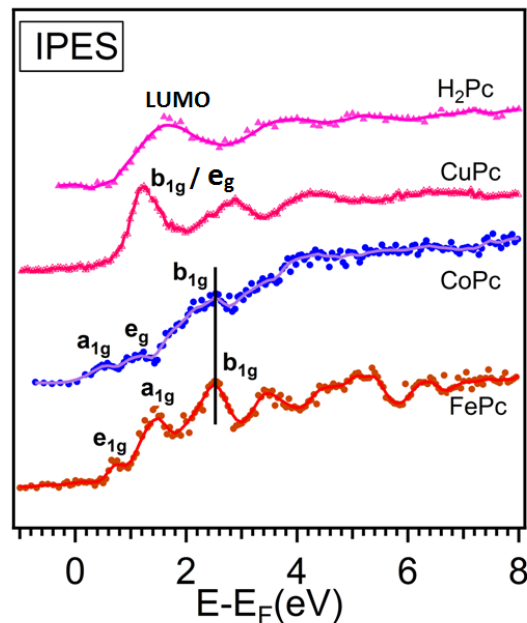
Figure 3: Inverse Photoemission spectra for 8 nm MPc TFs

The IPES spectra of the thin films (TFs) can be interpreted as a superimposition of empty state located on the metal central atoms and of the empty states located on the pyrrole and benzene

ring, at low energy, while at higher energy the dominant emission comes from the organic ligand molecular states. The IPES spectrum of the metal free Pc is characterized by a prominent feature at about 1.8 eV above the Fermi level and the other peaks common to the IPES data of tetrapyrrole thin films, in agreement with literature results. [19 and ref. therein].

The CuPc spectrum results similar, though the LUMO peak results more pronounced and all the feature result shifted with respect to the metal free case, strongly suggesting the influence of central metal atom on the energy level alignment. In case of CoPc and FePc additional peaks are present. Although, IPES measurements on MPc TFs have been published [19] however, due to poor resolution, the feature of the 3d orbitals near Fermi level are not well defined. Therefore, detailed information about the contribution of frontier orbitals is not well resolved.

As shown in Figure 3 our IPES spectra of the different MPc (due to higher overall energy resolution) are quite distinct and highlight the contribution of the 3d electronic states of the central atom to the empty orbitals.

In order to tentatively assign the MOs in our IPES data, we compare our measurements with XAS results on MPc present in the literature. As discussed in the previous chapter devoted to experimental techniques, the XAS and IPES techniques provide information on the unoccupied orbitals, considered more sensitive to the structural environment.[18] While IPES provide information on the total density of states corresponding to N+1 electron final state, XAS is element sensitive it provides information in the presence of the core−hole.

Moreover, as shown in Figure 1 central metal 3d orbitals have preferred orientations due to which it is possible to distinguish their contributions by examining variation in metal L_3 edge intensity for in-plane and out-of-plane polarization. CuPc TF empty MOs have been deeply discussed in the literature [30, 31, 19, 34 and references therein]. In particular the different experimental projections of the density of unoccupied states, obtained from the XAS Cu L3 edge, the N K edge, and inverse photoemission data have been compared in ref 34.

In case of CuPc only one hole is present, which is occupied by b_{1g} orbital in accordance with DFT and XAS studies.[6,12, 34] The single unoccupied b_{1g} MO for CuPc is resonant with the LUMO state localized on the pyrrole ring. This picture is consistent with the recent literature on MPc thin-films of tens of nm-thickness [12, 17, 34]
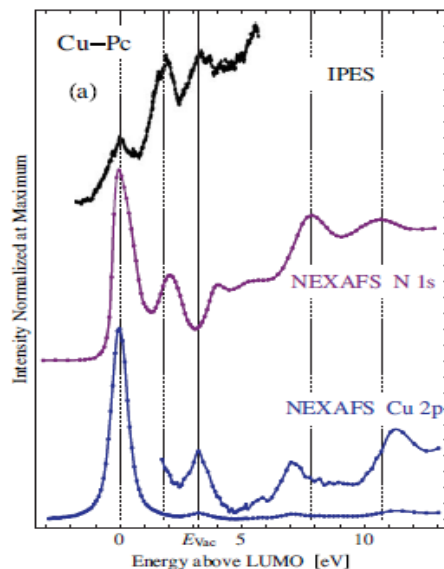
Figure 4 Comparison of the CuPc TF XAS and IPES results [reproduced from ref.34]

In case of FePc the central Fe^{+2} ion has to accommodate four holes (d^6). Analysis of Fe L edge supports the assumption that forth hole can occupy e_g or b_{2g} orbitals. However considering the XAS spectral similarities with CoPc it is proposed that ground state of FePc is similar to CoPc and forth hole occupies e_g orbital.[6] Importantly, magnetic properties of MPc molecules are significantly influenced by electronic ground state of the central metal atom and its hybridization with neighboring ligands. X-ray magnetic circular dichroism studies XMCD [13] show that MPc magnetic properties are impacted by electronic coupling to the underlying substrate.
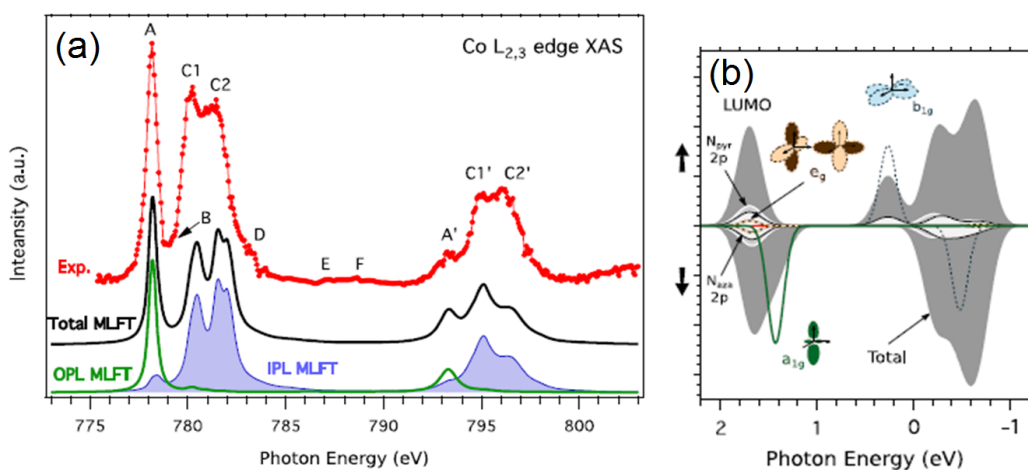
Figure 5 (a) Co L-edge X-ray absorpion spectrum (shown in red) in comparison with the multiplet ligand-field theory (MLFT) angleresolved simulation (shown in black), where the in-plane (IPL, blue filled) and out-of-plane (OPL, green) contributions are resolved. (b) DFT orbital and spin-resolved atomic contributions to the unoccupied valence states. [Reproduced from ref. 15]

CoPc gas phase XAS spectrum of Co L edge together with multiplet ligand-field theory (MLFT) angle resolved simulation, confirms that ground state configuration for CoPc is $^2A_{1g}$ with hole in the a_{1g} orbital.[15] However, ground state DFT calculations reveal that LUMO of CoPc has small contribution from e_g orbitals of Co metal atom and can hybridize with p_z orbitals of pyrrole and macrocycle nitrogen.

Furthermore, gas phase photoemission performed at different energies confirms that that the HOMO of CoPc has strong contribution from organic ligand of the molecule with feeble metallic character. [15] In the characterization of isolated CoPc (Figure 5) the sequence of 3d orbitals have been interpreted as e_g (LUMO) and a_{1g} at higher photon energy.[15] However, in case of MPc TFs, linear polarization XAS dichroism can be exploited to gain information about the symmetries of the electronic charge densities and the first empty orbital in XAS Co L_3 edge is assigned to the a_{1g} orbital.[6]
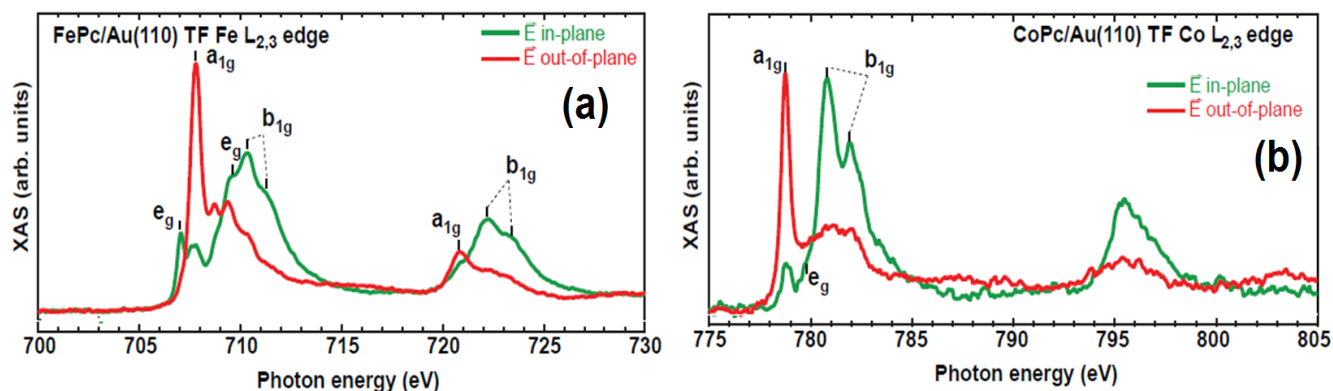
Figure 6 (a) Fe L edge NEXAFS for FePc TFs on Au(110) (b) Co L edge NEXAFS for CoPc TFs on Au(110) [Reproduced from ref. 24]

In case of CoPc TF on Au(110), the Co L_3 edge XAS spectrum exhibits high intensity for out-of-plane polarization and low intensity for in-plane polarization as shown in Figure 6(b). The observed trend unambiguously shows that a_{1g} orbital lies lower in energy as compared to e_g orbitals in case of CoPc thin films. On the other hand the trend of Fe L_3 edge (Figure 6 a) intensity variation shows that e_g orbitals lie lower in energy as compared to a_{1g} orbital for FePc thin films. Based on XAS analysis,[13] we assign the IPES first feature to the a_{1g} orbital in case of CoPc thin film while the e_{1g} lies lower in energy as compared to a_{1g} orbital for FePc thin film. Importantly, the relative separation of b_{1g} orbital from the fermi level in case of FePc is similar to CoPc, It means that addition of an electron doesn't influence the b_{1g} orbital. This inference is coherent with X-ray absorption study. In our IPES results we follow the assignment of previously described XAS [13], as labeled in the Figure 3.

In summary, for CuPc the central metal ion-related states are due to the b_{1g} orbitals, while the CoPc TF spectrum has a more complex attribution considering its ground state configuration. In fact, the a_{1g} MO is at lower energy as compared to the b_{1g} MO, thus we can tentatively assign the

first IPES feature of the CoPc TF to the partially filled a_{1g} MO. This picture is consistent with the recent literature on MPc thin-films of tens of nm thickness.[19,20] We assign the LUMO near 1.4eV in the CuPc IPES spectrum to the b_{1g} orbital.

3.2 CoPc/Au(110) and CuPc/Au(110)

IPES has been efficiently utilized to distinguish the molecule-substrate interaction for the adsorption of a variety of aromatic molecules, like non-metalate Tetraphenyl-Porphyrin (2H-TPP) on filled d-band metals [21], enlightening band splitting upon interaction, and being sensitive to the different structural arrangements adopted by molecules.[21]

In this section, we exploit IPES to highlight the contribution of frontier unoccupied MOs in the interfacial electronic properties at CoPc and CuPc interface with Au(110) to highlight the influence of d level occupancy on unoccupied density of states. It has been observed that adsorption of MPc molecules on metallic substrates can lead to reconstruction of the substrate symmetry. The structure of a CoPc or a CuPc layer on Au(110) and the substrate reconstruction in the sub-monolayer regime investigated by low energy electron diffraction (LEED) and grazing incidence X-ray diffraction (GIXRD) demonstrate that MPcs cause (5x5) and (5x7) reconstructions with increasing film thickness.[22] Scanning Tunneling Microscopy (STM) studies of the self-assembly of MPcs on Au(110) demonstrate that molecules lie flat on the substrate and arrange in compact chains along the Au(110) reconstructed channels, exhibiting two-dimensional (2D) long-range order.[23] The interfacial interaction for the deposition of CoPc and CuPc on Au(110) has been studied using photoemission, X-ray absorption spectroscopy(XAS) and X-ray Magnetic Circular Dichroism (XMCD). Importantly, XMCD studies reveal total quenching of CoPc magnetic moment on Au(110) for low coverages, in contrast to CuPc, demonstrating the possibility of rehybridization of the CoPc frontier orbitals with the underlying Au states.[23] Despite IPES studies have been performed for MPc thin films on metallic substrates, a comprehensive investigation of the unoccupied states involved in the interaction process for the self-assembly of CoPc and CuPc on metal surfaces is still lacking.

In this section, we investigate by IPES the involvement of CuPc and CoPc frontier orbitals interaction with Au(110), in the low-coverage range. Furthermore, the high overall resolution of our IPES (due to high detector sensitivity-efficiency and low thermal spread of the electron beam) enables us to highlight the subtle details about the empty states of CoPc and CuPc involved in the interaction with the underlying Au substrate states, unveiling a surface driven symmetry reduction of the electronic molecular states induced by CoPc adsorption on Au(110), while CuPc interacts weakly.

37
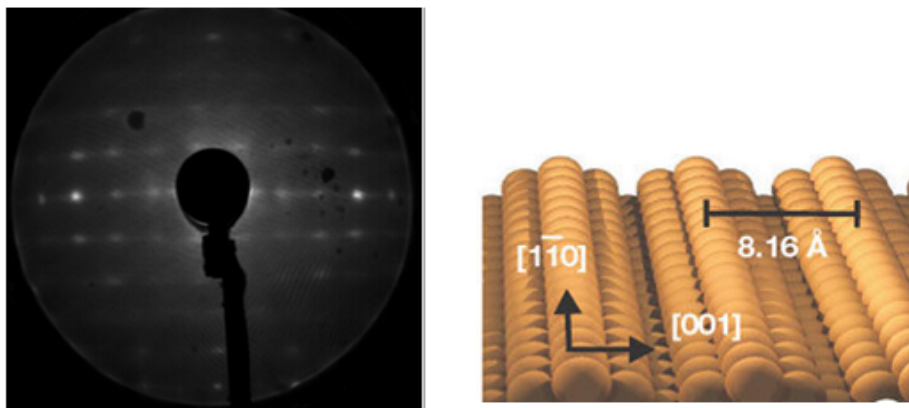
Figure 7 (a) LEED pattern showing the 5x5 reconstruction for the deposition of CoPc on Au(110) (b) Model of the missing row symmetry of 1x2 Au(110) clean surface.[23]

We can thus provide a coherent picture of the interface electronic structure of CoPc and CuPc, induced by the different occupancy of 3d level of central metal atom, complementary to X-ray absorption studies. Cobalt and copper-phthalocyanines adsorbed on the Au(110) reconstructed channels form ordered super-structures constituted by flat lying parallel molecular chains as reported in the STM image for self-assembled CoPc chains.[24] These chains give rise to a 5×5 symmetry reconstruction, as confirmed by the LEED pattern shown in Figure 7. Further deposition leads to differences in the CuPc [25] and CoPc a 5×7 periodicity [24] at the completion of the first single layer (SL) with MPc chains and testifying differences in the MPc Au(110) interaction in the two cases. In order to investigate the empty orbitals involved in the interfacial interaction we have monitored the evolution of IPES spectrum with increasing thickness of CoPc and CuPc thin films on Au(110)-(1x2) as shown in Figure 8(a,b). Clean Au(110)-(1x2) spectrum at normal incidence (Γ point), in agreement with literature, is characterized by a surface state at about 0.2 eV above the Fermi level. At low coverages the Au(110)-(1x2) IPES spectrum shows considerable modifications after the deposition of CoPc and CuPc.

The peak line shapes are notably different for CoPc and CuPc depositions for low as well as high coverages. Empty molecular states grow with the film thickness and become prominent for the 5x5 (0.7ML) systems. IPES spectrum at high coverages is characterized by three peaks corresponding to empty molecular states for both MPcs. The CoPc 3 ML is similar to the 8 nm CoPc TF IPES shown in Figure 3.

38
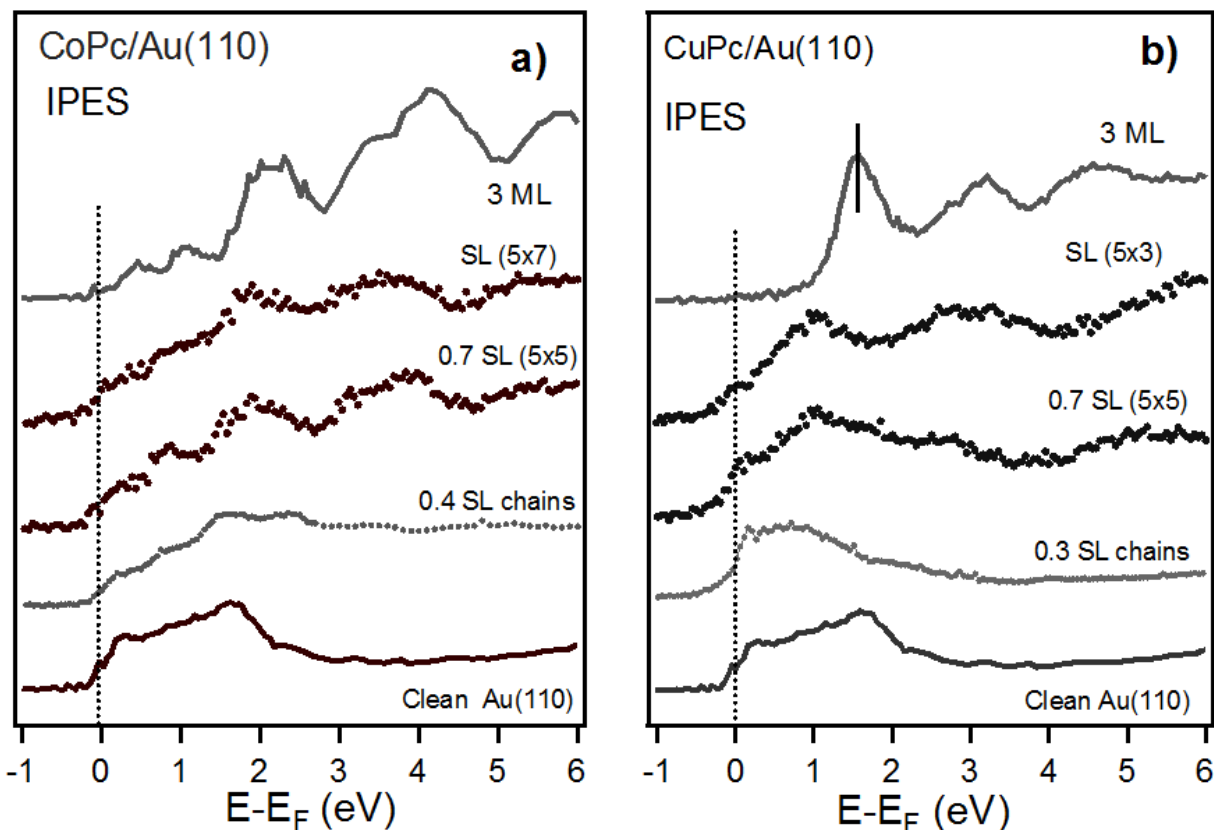
Figure 8 Evolution of the IPES spectrum as a function of coverage upon deposition of CoPc (a) and CuPc (b) on the Au(110) surface.

It is evident from Figure 8(a) for the deposition on CuPc on Au(110) that the emission near Fermi level is only slightly decreased completely for 0.3ML deposition while for CoPc system it results broader. The unoccupied MOs start to appear at 0.3 ML coverage and become prominent at higher film thickness. The dichorism shown at the Cu $L_{2,3}$ edge XAS for the monolayer deposition of CuPc on Au(110) shows that the MO involved in the transition have in plane symmetry[23] indicating that empty states have in plane, d_{x2-y2} symmetry. These states are involved in bonding with the nitrogen of pyrrole ring of macrocycle and do not contribute to the interaction with substrate.[23] Our IPES measurements supports these observations as the emission near Fermi level corresponding to Au(110) is not completely suppressed in contrast to CoPc deposition strengthening the argument of weaker interaction of CuPc with Au(110) as compared to CoPc. It is worth noting that though both CoPc and CuPc molecules have same spin (1/2) configurations, their response to the external magnetic field in the submonolayer regime is considerably different.[23] Based on DFT and XMCD analysis it is demonstrated that magnetic moment of CuPc is due to partially occupied b_{1g} MO and remain unaltered at low coverages. This observation supports the argument that partially occupied b_{1g} state with d_{x2-y2} symmetry couples weakly with Au(110).

39

Although, theoretically there is ambiguity regarding the nature of the LUMO in CoPc as discussed in previous section, it can inferred from IPES spectrum that the energy position of first feature related to unoccupied density states for CoPc and CuPc, with respect to Fermi level is different for CoPc and CuPc indicating that their interfaces are not identical with metallic substrate highlighting the influence of central metal atom on energy level alignment. The energy level alignment is influenced by screening and by the change in molecular orientation with thickness of the adsorbed molecules. It has been observed that change in the molecular orientation with thickness results in energy level shifts at the interfaces and significantly influence device performance.[18] IPES spectrum shows that for coverages beyond the monolayer, the LUMO shifts with respect to the Fermi level differently   in CuPc andCoPc , as shown in Figure 8(a) (see also reference 19 for MPc/Au(111)). Coverage dependent shift of HOMO in UPS towards higher binding energy has been reported for example in case of CuPc deposition on Au(110).[32]
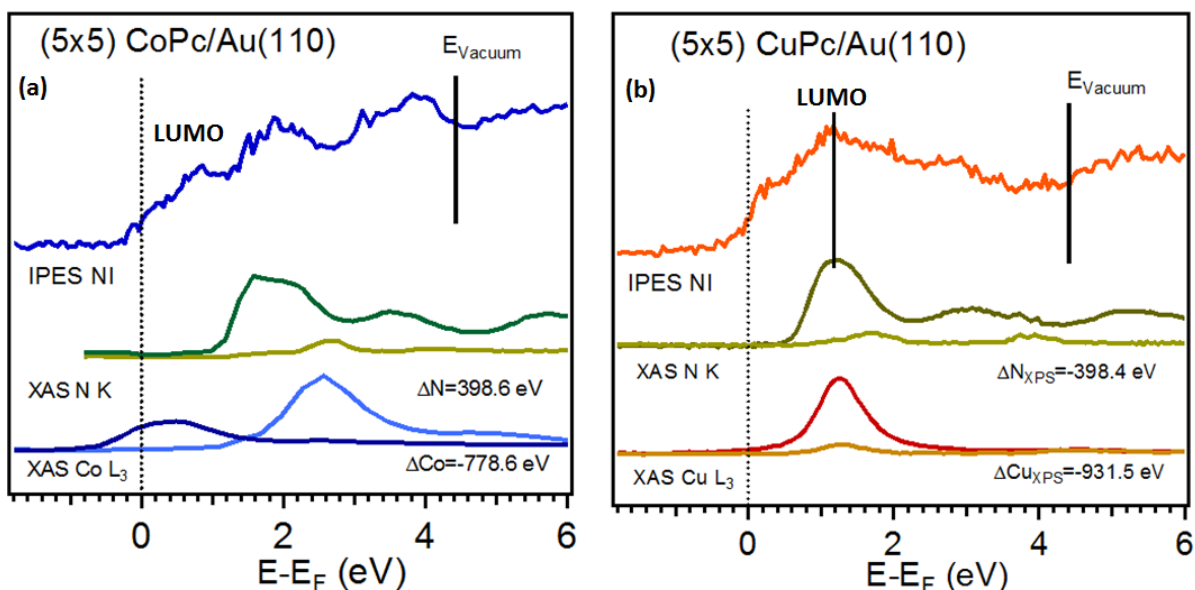
Figure 9 Comparison of normal incidence and angle resolved IPES spectrum for the deposition of (a) CoPc on Au(110), (b) CuPc on Au(110) along with N K edge and Co L edge to reveal intermixing of metal-molecule Co $3d_{z2}$.

In order to complete the identification of the empty states, we compare IPES spectra for the 0.7 ML (5x5) structures of CoPc and CuPc on Au(110), and element selective X-ray absorption spectra from the N K and metal L_3 edges, as shown in Figure 9(a,b). In particular, the XAS data have been taken with linearly polarized radiation in the two s- and p- configurations; due to the flat adsorption of the (5x5)-0.7 ML [24], a strong dichroic effect is visible, with the p-component exciting the π*-related resonances and the s-one exciting to the σ*-empty states. For a neat comparison with the IPES spectra, the XAS edges from reference 23 are shifted aligning the MO assignment following the procedure of reference 34. The corresponding shifts differ by the XPS binding energies of the respective core levels (see Figure 10). The values of the shifts do not

match with the core level binding energies due to electron-hole interaction effects, as in case of IPES no core hole is formed so electron-hole interaction effects are absent.

It is depicted by the dichroism shown by Co L_3 XAS peak that the electronic states near Fermi level have contribution from Co $3d_{z2}$. Importantly at grazing incidence the feature corresponding to Co $3d_{z2}$ broadens with respect to the TF data [23], suggesting an intermixing of Co $3d_{z2}$ and Au(110) states near the Fermi level. Such broadening of Co $L_{2,3}$ edge is not observed for the adsorption of CuPc on Au(110).
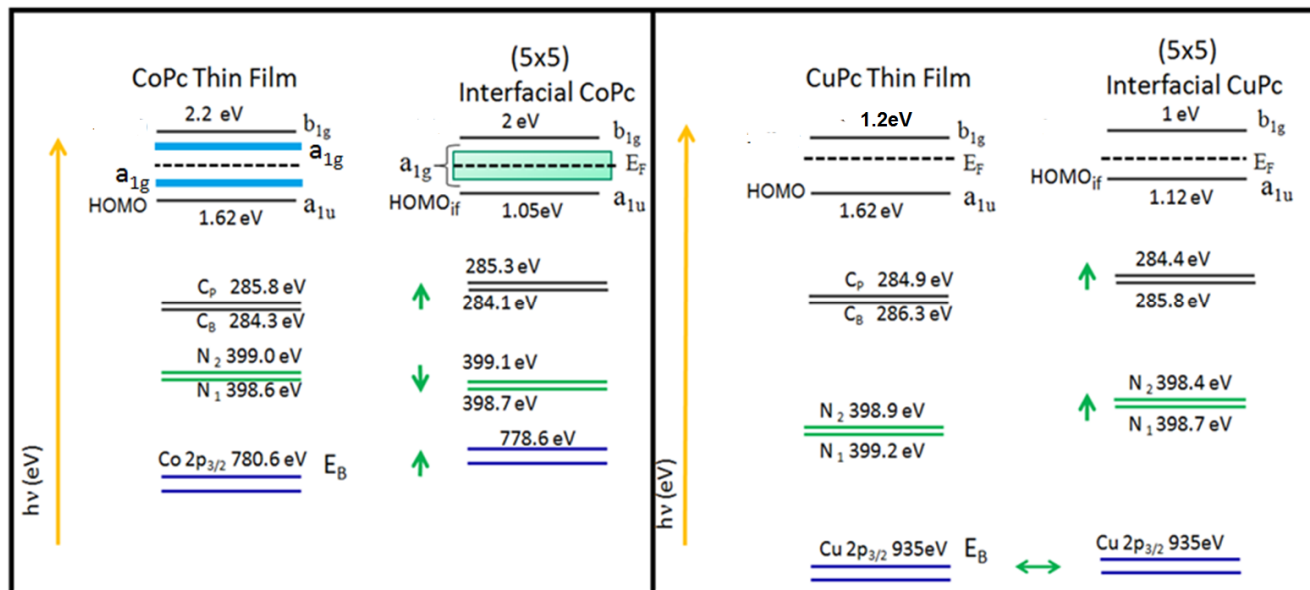
Figure 10 Energy level alignment for the adsorption of CoPc and CuPc on Au(110) in the thin film and submonolayer regime.

The dissimilarities in the interfacial interaction observed by IPES measurements for the deposition of CoPc and CuPc on Au(110) are also supported by photoemission spectroscopies as shown in Figure 10. C1s and N1s XPS spectrum line shapes do not change significantly with increasing film thickness of CuPc on Au(110).[32] However, a chemical shift of 0.5eV towards higher binding energy has been observed for both C1s and N1s XPS spectrum at higher film thickness. The observed shift is attributed due to the screening effects of underlying metallic substrate. In addition, no significant change in line shape and chemical shift has been observed for the Au 4f core levels measured for the clean Au(110)-(1x2) surface, submonolayer phase (5x5) and monolayer phase (5x3) for the deposition of CuPc on Au(110). These results clearly indicate that no significant charge transfer takes place between CuPc and the underlying substrate complementing our IPES observation. In contrast to Cu2$p_{3/2}$, Co 2$p_{3/2}$ core level XPS spectrum shows notable chemical shift of 2eV towards higher binding energy with increasing film thickness suggesting charge transfer between adsorbed molecules and substrate.

Importantly, normal-emission UPS spectra reveal the presence of an interface state at 0.73eV below the Fermi level for the deposition of CoPc on Au (110).[26] Similar interface state has been observed for FePc on Au(110). These observations clearly indicate towards involvement of metal 3d states with underlying substrate. Similar to UPS, our IPES spectra also show an intermixing of Co $3d_{z^2}$ orbitals with underlying Au substrate near the fermi level for the adsorption of CoPc on Au(110) at submonolyer coverages, further supporting the inference that in case of CoPc metal 3d states interacts with Au(110).

DFT calculations are performed [reference S. Fortuna and S. Fabris, unpublished] for CoPc/Au(110) system for adsorption geometries with the metallic center both on top of a central Au atom and short-bridged between two Au atoms of the same row. It results that molecules does not have any preferential adsorption site, as the top configuration is favored over the short-bridged by only 0.057 eV, well below the calculation error. No correlation effects are introduced.
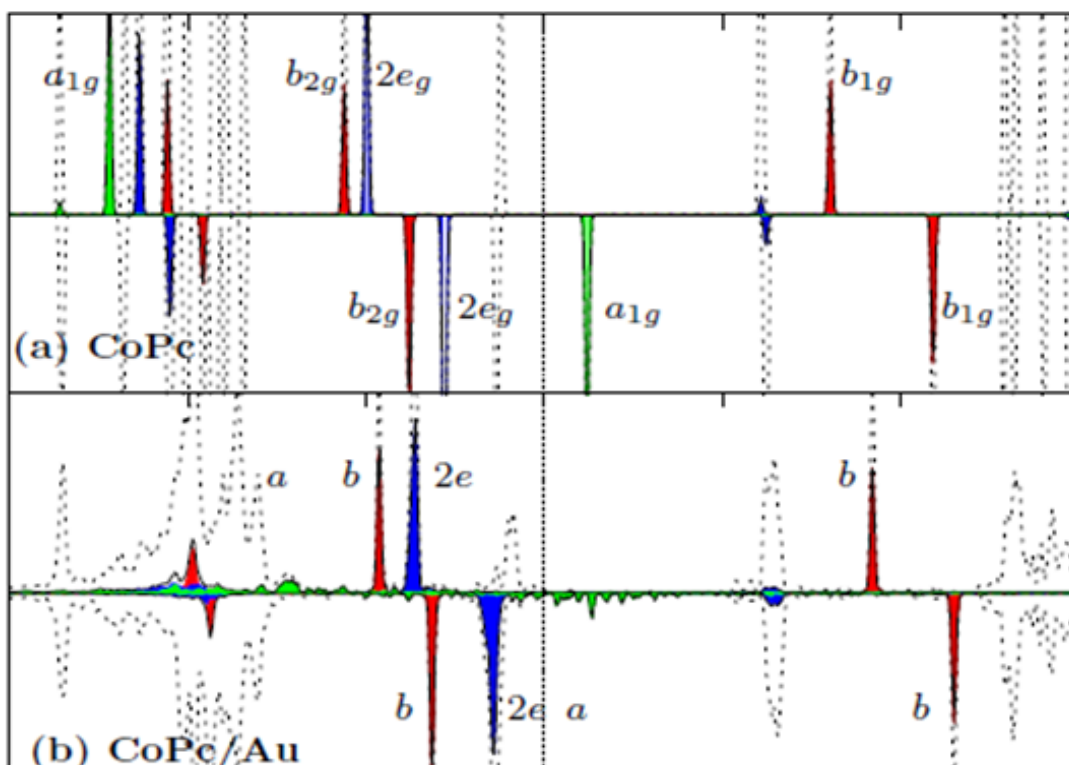
Figure 11 Projected density of states (pDOS)for (a) free CoPc and (b) CoPc/Au(110), pDOS on the CoPc (black dotted), metal (black solid),d_{xz} and d_{yz} (filled blue/dark grey), and d_{z^2} (filled green/light grey), $d_{x^2-y^2}$ and d_{xy} (red).

The projected density of states (pDOS) of the adsorbed CoPc molecule on Au(110) substrate with that of isolated CoPc molecule are compared in Figure 11 in order to understand nature of the CoPc/Au(110) interaction. In case of free CoPc molecule, the central metal atom has a partially filled a_{1g} state. However, due to interaction with underlying substrate spread along the whole observed energy range, centered at the Fermi level. By adsorption, the states does not

change their ordering, as previously observed for the FePc, with the exception of the spin down a_{1u} organic state which now overlaps with the e_g states. Also the delocalized π-system indicates a stronger interaction of the organic portion of the molecule with the metallic surface, an effect more pronounced for the filled states. By looking at the mixing of the Co d orbitals, in the case of the free CoPc the b_{2g} states have a pure d_{xy} component, the b_{1g} has only d_{x2-y2} component, while the e_g result as the product of an equal mixing between the d_{xz} and d_{yz} as expected in a D_{4h} framework.

In conclusion, our IPES results for the deposition of CoPc and CuPc on Au(110) are in coherence with DFT calculation which depicts that in case of CoPc partially occupied out of plane a_{1g} sates are involved in interaction with s-like valence band of Au substrate.[23] In addition calculations show that adsorption energy is higher for CoPc as compared to CuPc with lower Co-metal distance. The charge reorganization is weaker for CuPc which does not involve partially occupied b_{1g} state. Our IPES spectra for CuPc/Au(110) do not show significant involvement of Cu 3d orbitals with the underlying substrate in accordance with theoretical calculations for this system.

The CoPc adsorption on Au(110) induces a re-hybridization of the electronic states localized on the central metal ion, promoting a charge redistribution of the molecular orbitals of the MPc molecules, and the molecule-substrate interaction is controlled by a symmetry-determined mixing between the electronic states. [24] A comparison of the evolution of the molecular states intermixing by means of inverse photoemission and of the atom selected empty state projection as deduced by absorption spectroscopy, is a powerful route to identify the role of the organic ligands and the metallic centers in the interaction process.

Charge transfer from Au(110) to partially filled $3d_{z2}$ can be responsible for different energy location of frontier unoccupied states in case of CoPc as compared to CuPc. Similar observation regarding the different offsets of LUMO with respect to Fermi level have been reported for the deposition of CuPc and CoPc on Au(111) due to engagement of CoPc frontier orbitals with Au(111) states.[19] Similar inferences have been drawn based on STM studies demonstrating higher interaction for the self assembly of CoPc on Au(111) as compared to CuPc.[27]

3.3 Metal Phthalocyanine thin film: Influence of polymorphism and crystallinity on physical properties

In order to utilize metal phthalocyanine thin film for technological applications it is crucial to gain thorough understanding of various factors influencing optical, vibrational and dynamical properties. In particular due to MPc thin film applications in solar cells and light emitting diodes, there is considerable research interest in their optical and dynamical properties. 14] Metal phthalocyanine molecules form ordered crystalline structures due to their self-organizing property. However, self organization of organic molecules is governed by different possibilities

43

of close packing arrangements. Intermolecular interactions such as π-π interactions and Van der Waals interactions play crucial role in governing the overall crystalline order of MPc thin films on underlying substrate. In order to maximize favorable intra and intermolecular interactions MPc molecules can adopt different molecular arrangements which differ in their relative orientation. The aggregation of Tetrapyrrole complexes thin films enhances the intermolecular π-π stacking, facilitating the intramolecular charge transport. The understanding and the control of the processes determining the magneto-electronic and dynamic properties of organic semiconductors are crucial to the further development of organic electronics and other technological applications.

Self assembly of MPc leads to ordered molecular structure on wide variety of substrates and crystalline films show distinct polymorphs. Among different polymorphs, α- polymoprphism is commonly observed for the room temperature deposition on weakly interacting substrates. While annealing of α- polymorph above 200°C leads to almost complete convertion of α-polymporph to β-polymorph.[35] Molecules adopt herringbone molecular arrangement in both α and β polymorphs. The β-polymorph is thermally more stable and differ from α polymporph by the molecular orientation and stacking with respect to substrate. Due to dissimilar molecular stacking in the two polymorphs the structural, morphological, vibrational and spectroscopic properties of thin films are notably influenced.[35]

Although, α-polymorph is the commonly observed polymorph for the room temperature deposition of MPc. However, herringbone molecular stacking may not be always observed in the α- polymorph. An electron diffraction study for the 300 nm thick CuPc films reveal the presence of brickstone molecular arrangement for the α- polymorph.[36] The coexistence of brickstone and herringbone molecular arrangements have been confirmed by the GIXRD analysis for the room temperature deposition of CuPc on ZnO(1$\bar{1}$00) as shown in Figure 12.[36]

The Figure 13 shows the schematic representation of the molecular orientation adopted by molecules in two structural phases. Simulations of the reciprocal space maps have been performed using SimDiffraction software to determine the peak positions corresponding to herringbone and brickstone molecular arrangements. The simulations of the reciprocal space maps (Fig.12(a)) clearly demonstrate the peak positions corresponding to herringbone and brickstone molecular arrangements. The peak positions differ considerably in the region of Q_{xy}=1.7 and 1.9 Å^{-1}.

44
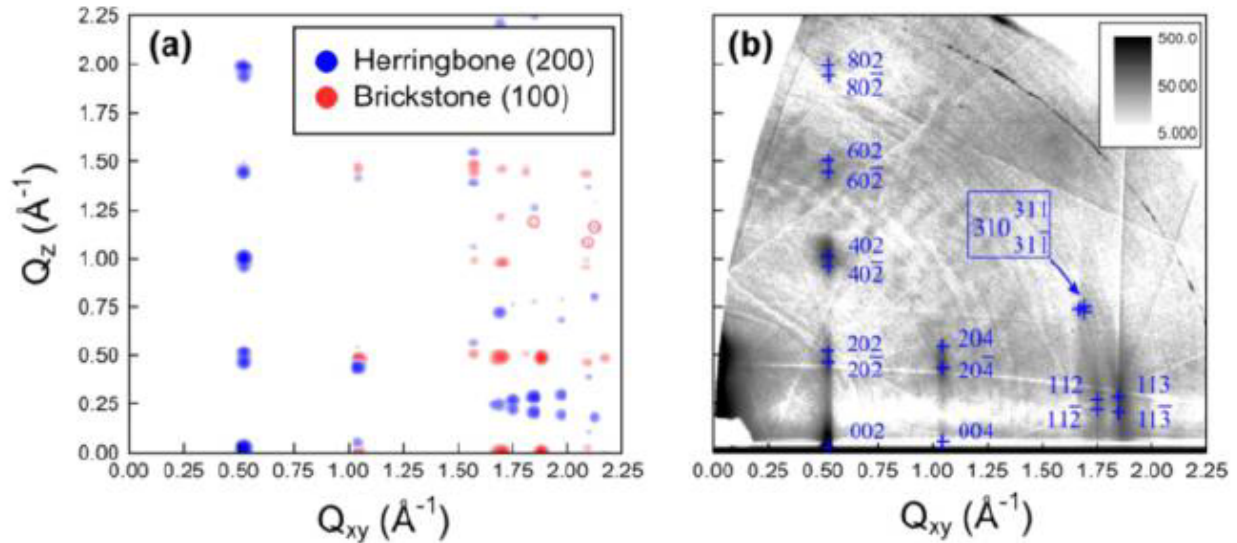
Figure 12 (a) Simulated peak positions for herringbone and brickstone molecular arrangements (b) GIXRD analysis for the room temperature deposition of CuPc on ZnO(1$\bar{1}$00) as shown in Figure 12(b).Repordced from reference 36.
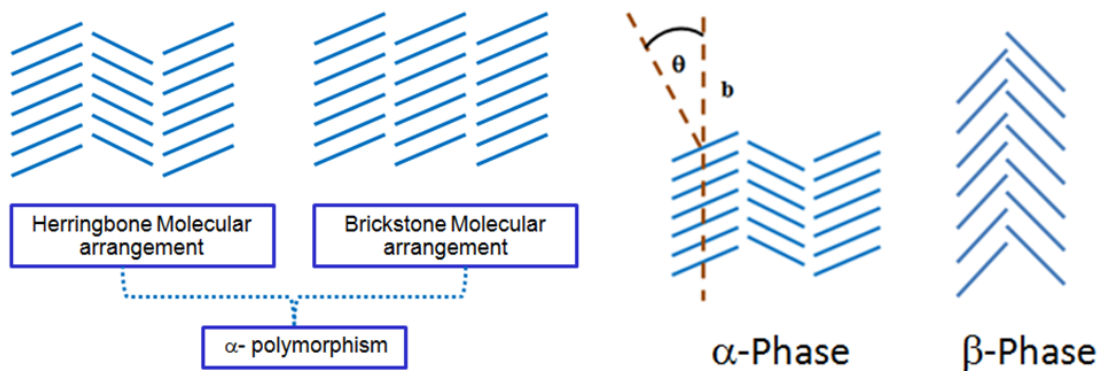
Figure 13 Schematic representation of molecular arrangements adopted by MPc TFs in α and β-Phases

The MPcs thin films generally adopts α-phase for the room temperature deposition, while thermally state β-phase is mostly found in bulk crystals. Figure above shows the peculiar molecular arrangements corresponding to these phases where β-phase is characterized by $\theta \sim 45^{\circ}$ in contrast to metastable α-phase with $\theta \sim 25^{\circ}$. Based on electron diffraction measurements it has been reported that 300nm CuPc films adopt brickstone arrangement with a triclinic crystal structure. However, monoclinic crystal structure has also been proposed for CuPc TFs by Ashida et al. with herringbone molecular arrangements.

The physical properties of metal phthalocyanines thin films are strongly influenced by phthalocyanine polymorphism [37], crystal structure, and central metal atom [38]. In addition, nature of substrate significantly influences the properties of the metal phthalocyanine thin films

45

by controlling the molecular orientation during growth[39]. Substrate surface properties can significantly influence the growth mechanism thus effectively controlling the crystal phase and film structure [40]. In this regard, various parameters such as substrate surface roughness, deposition temperature and molecule–substrate interactions are crucial for fabrication of good quality films.

The relative molecular arrangements of polymorphs are unique and known to influence the optical and transport properties of thin films significantly. It has been demonstrated that absorption spectra of MPc is red shifted in the triclinic structure due to increased intermolecular interactions in this phase.[41] Raman spectroscopy efficiently highlights dissimilarities in the vibrational properties of α–polymorph to β–polymorph adopted by CoPc and FePc thin films. In order to gain control over the organic thin films phase and morphology organic molecular beam deposition has been effectively utilized to get high quality and reproducible samples.[41] In addition the interaction of central metal atom with the substrate effectively controls the organic thin films properties, as the hybridization of metal 3d and macrocycle orbitals determines the gap between the highest occupied molecular orbital (HOMO) and the lowest unoccupied one (LUMO), which is crucial parameter for optoelectronic devices.[41]

X-ray adsorption based study for the adsorption of CuPc on polycrystalline gold and ITO shows that molecules adopt standing configuration on the substrates [42] though detailed molecular arrangements have not been thoroughly understood. Here, we present a comprehensive study for FePc and CoPc grown at room temperature on technologically applicable substrates. A multi-technique characterization approach is needed to comprehend the detailed information about the molecular phases. We have adopted grazing incidence X-ray diffraction (GIXRD), atomic force microscopy (AFM) and Raman spectroscopy to decipher the solid state packing of MPc on substrates.

The first section of the chapter presents a comprehensive study of CoPc and FePc thin films of about 50 nm thickness on technologically relevant substrates such as SiOx/Si, indium tin oxide (ITO) and polycrystalline gold in order to investigate the substrate induced effects on molecular stacking and crystal structure. Raman spectroscopic analysis reveals lower intensity for the vibrational bands corresponding to phthalocyanine macrocycle for the CoPc and FePc thin films grown on ITO as compared to SiOx/Si due to the higher order of phthalocyanine molecules on SiOx/Si. Grazing incidence X-ray diffraction reciprocal space maps reveal that FePc and CoPc molecules adopt a combination of herringbone and brickstone arrangement on SiOx/Si and polycrystalline gold substrate, which can have significant implications on the optoelectronic properties of the films due to unique molecular stacking.

3.4 FePc and CoPc thin films on polycrystalline gold, SiOx/Si and ITO

Thin films of CoPc and FePc of about 50 nm thickness were deposited on ITO (1.7 nm roughness), polycrystalline gold (Au, 0.3 nm roughness), and native oxide SiOx on Si(100)

(SiOx roughness is 0.2 nm). The FePc and CoPc high purity polycrystalline powders (Sigma Aldrich) were evaporated from resistively heated quartz crucibles in UHV at the base pressure of 2×10^{-10} mbar and low deposition rate of 2 Å/min. All the depositions were performed at room temperature. The three substrates were rinsed in acetone before introducing them into the UHV chamber.

3.4.1 Structural and morphological Characterization

In order to gain information about the structural properties of CoPc and FePc films deposited on polycrystalline gold, SiO_x/Si and ITO substrates GIXRD reciprocal space maps have been analysed as shown in Figure 14. Comparison of reciprocal space maps clearly demonstrate the notable differences in the molecular order corresponding to CoPc and FePc TFs on gold, SiO_x/Si and ITO substrates.

In particular, CoPc and FePc on SiO_x/Si exhibits higher crystalline and ordered structure as compared to gold and ITO as depicted by several distinct diffraction spots. It is evident that diffractions spots are comparatively broader for the deposition on polycrytalline Au, demonstrating that molecular stacking disperse over a range of orientations for most of FePc and CoPc crystallites. Further, GIXRD reciprocal space map analysis for the deposition on ITO demonstrate that crystalline order is poor as almost no diffraction spots are observed. It can be inferred that and CoPc and FePc molecules are randomly oriented on ITO.

It is well established that MPc molecules adopt a α-polymorphism for the room temperature deposition on substrates however, in order to gain thorough information about the herringbone and brickstone molecular arrangements for α-polymorphism, we compared our reciprocal space maps with reciporcal space maps for CuPc adsorbed on ZnO(1$\bar{1}$00) as shown in Figure 12. It is apparent that there is good resemblance between reciprocal space maps for the deposition of FePc and CoPc on SiO_x/Si and reciprocal space maps for CuPc adsorbed on ZnO(1$\bar{1}$00).[36] Simulations performed by SimDiffraction software assign peaks around Q_{xy}=1.7, 1.9 Å^{-1} and Q_{xy}=0.5, 1.04 Å^{-1} to brickstone (100) oriented phase and herringbone (200) oriented phase.[36]

It is worthwhile to mention that our reciprocal space maps show diffraction spots at Q_{xy} values corresponding to both herringbone and brickstone molecular arrangements. It suggests that for 50nm thick CoPc and FePc films the molecules are arranged in a mixed phase. The two phases differ in their relative orientation of molecules.[36] It is important to note that in case of FePc and CoPc deposition on Au substrate the diffraction spots are observed around Q_{xy}=1.7 and 1.9 Å^{-1}. However, diffraction spots are more spread indicating reduced molecular order on polycrystalline Au.
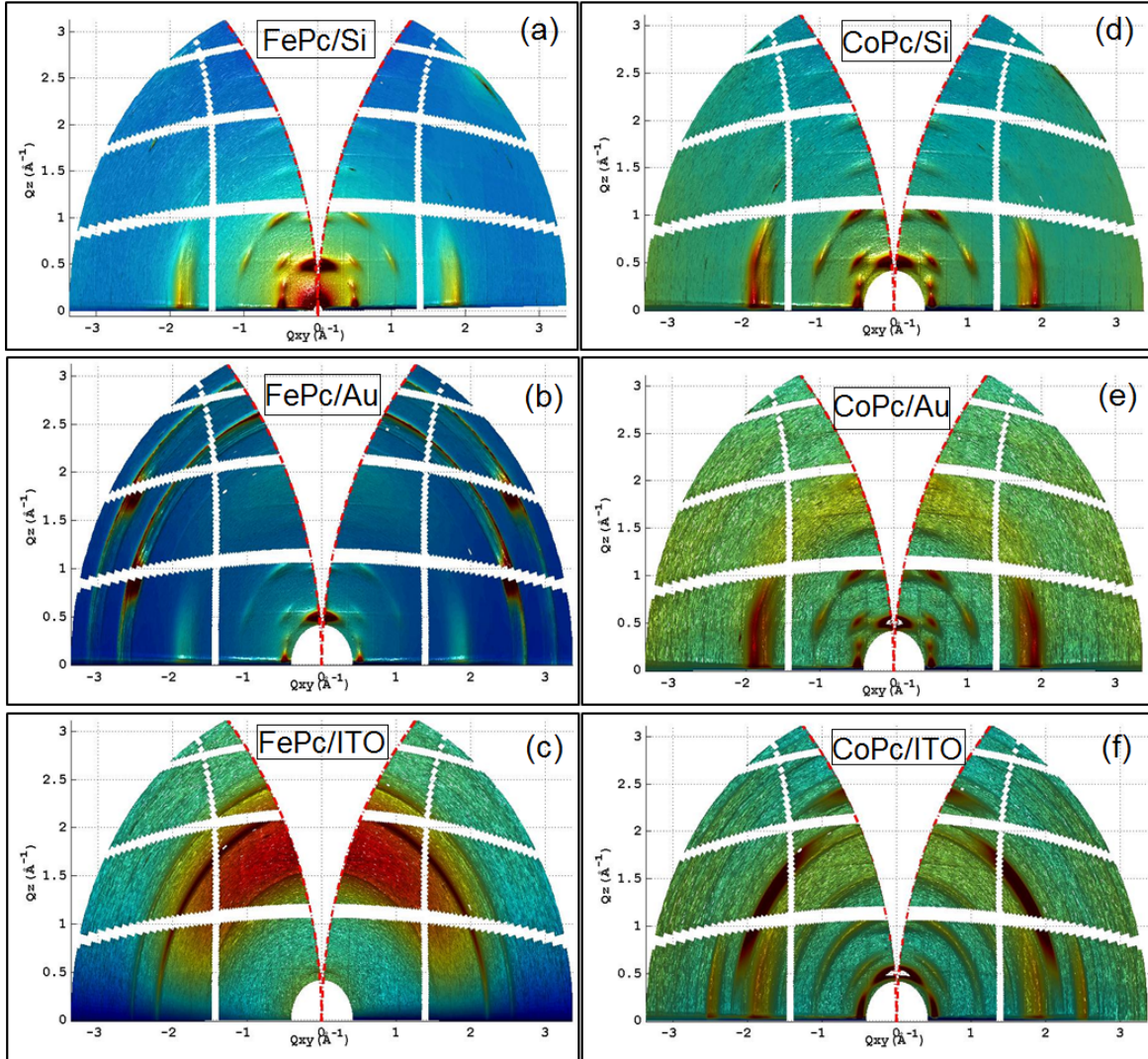
Figure 14 GIXRD reciprocal space maps for the deposition of FePc (a, b, c) and CoPc (d, e, f) on SiOx/Si, Au and ITO at room temperature.

Average crystallite size obtained by the GIXRD peak profile analysis agrees reasonably with the values obtained from AFM image analysis (Table 1) and follows similar trend.   We have analyzed the topography of CoPc and FePc thin films using AFM as shown in Figure 15. FePc films on Au consist of densely packed, small elongated grains which are randomly distributed. Notably the grain density for the FePc thin film is higher as compared to CoPc thin film deposited on Au. These grains have good resemblance with CuPc thin films grains deposited on glass which adopts α phase for room temperature deposition.[44] The shape of grains is characteristic of α phase as β phase exhibits much longer grain size obtained for the deposition above 200^oC temperature.[43]

48

	FePc_ SiO$_x$/Si	FePc _Au	FePc_ITO	CoPc_ SiO$_x$/Si	CoPc_Au
A	12.0	16.9	18.0	12.4	14.0
B	11.8	14.0	17.3	12.0	13.1
C	0.2	0.3	0.2	0.3	0.3

Table-2

	FePc_ SiO$_x$/Si	FePc _Au	FePc_ITO	CoPc_ SiO$_x$/Si	CoPc_Au
A	12.0	16.9	18.0	12.4	14.0
B	11.8	14.0	17.3	12.0	13.1
C	0.2	0.3	0.2	0.3	0.3

Table-3

Table for GIXRD profile analysis of FePc and CoPc films on SiOx/Si, Au and ITO substrates. Average crystallite sizes estimated along the Out of Plane (2) and the In Plane (3) direction are calculated from the FWHM of reflections belonging to the *h00* and *01k* families, respectively. A: Average crystallite Size (surface weighted) [nm], B: Average crystallite Size (volume weighted): [nm], C: Average Microstrain (SQR$<e^2>$) (%),

AFM images are analyzed using average crystallite size and RMS (Roughness) parameters as listed in Table 4. The average crystallite size and RMS values are highest for ITO as compare to Au and SiO$_x$/Si. Lower RMS values for the deposition of FePc and CoPc on Au and SiO$_x$/Si indicate that molecules are comparatively uniformly distributed as compare to ITO. Due to weaker interactions of FePc and CoPc with ITO the molecules tend to aggregate under the influence of intermolecular interactions which results in higher surface roughness and average crystallite size.

STM study for the room temperature deposition of FePc on Au (111) shows that molecules adopt columnar stacking structure on Au (111).The molecules lie on the substrate with small tilt angle at low coverages due to higher molecule-substrate interactions.[14] It is the strength of molecule-substrate and molecule–molecule interactions that generally controls the self assembly of the molecules and registry of first layer directs the growth of further layers.

Comparatively lower crystallite size and RMS values for deposition of FePc and CoPc on Au and SiO$_x$/Si indicate that the influence of molecule-substrate interactions appear to be more pronounced for Au and SiO$_x$/Si as compared to ITO and significantly influence the film growth.
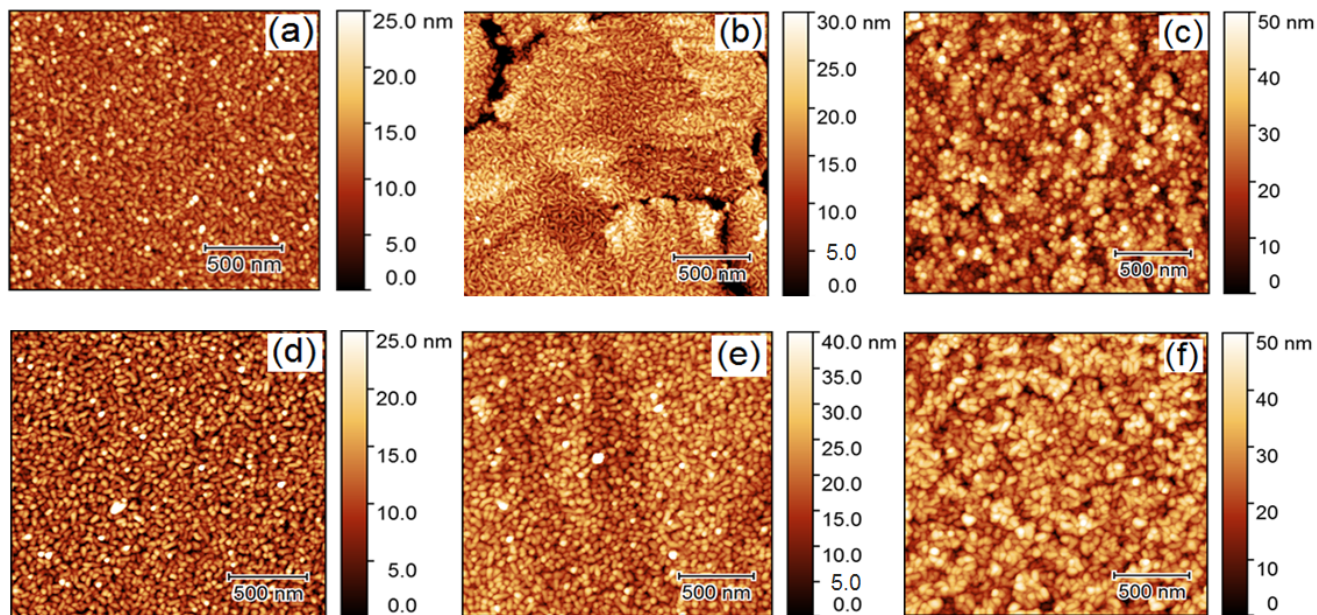
Figure15 AFM images for the deposition of FePc (a, b, c) and CoPc (d, e, f) on SiOx/Si, Au and ITO at room temperature

System	Average grain size (AFM analysis)	Average crystallite size (GIXRD)	RMS (Roughness)
FePc_ SiO$_x$/Si	10.56nm	11.80 nm	3.190nm
FePc _Au	15.89nm	13.99 nm	3.442nm
FePc_ITO	22.44nm	17.32 nm	8.862nm
CoPc_ SiO$_x$/Si	10.16nm	10.80 nm	4.562nm
CoPc_Au	20.27nm	14.5 nm	5.100nm
CoPc_ITO	25.63nm	Nil	7.485nm

Table-4 Comparison of average grain size obtained from AFM analysis with the crystallites size as obtained from GIXRD peak profile analysis.

3.4.2 Dependence of vibrational properties on molecular order

The relative molecular arrangements of polymorphs are unique and known to influence the optical and transport properties of thin films significantly. It has been demonstrated that absorption spectra of MPc is red shifted in the triclinic structure due to increased intermolecular interactions in this phase.[45] Figure 16 and Figure 17 show the Raman spectra of CoPc and FePc thin films of about 50 nm thickness deposited on polycrystalline gold, silicon and ITO. The assignments of the peaks related to various vibrational modes are shown in figure.[46-48] The Raman spectrum of metal phthalocyanine is dominated by A_{1g}, B_{1g}, B_{2g} and E_g modes corresponding to vibrations of the macrocycle, isoindole moieties and metal–nitrogen bands.[48] The spectrum exhibits phthalocyanine macrocycle vibrational bands in region of 600cm^{-1} to 800cm^{-1}. No significant wave number shift is observed for the Raman vibrational bands of CoPc and FePc deposited on these substrates.
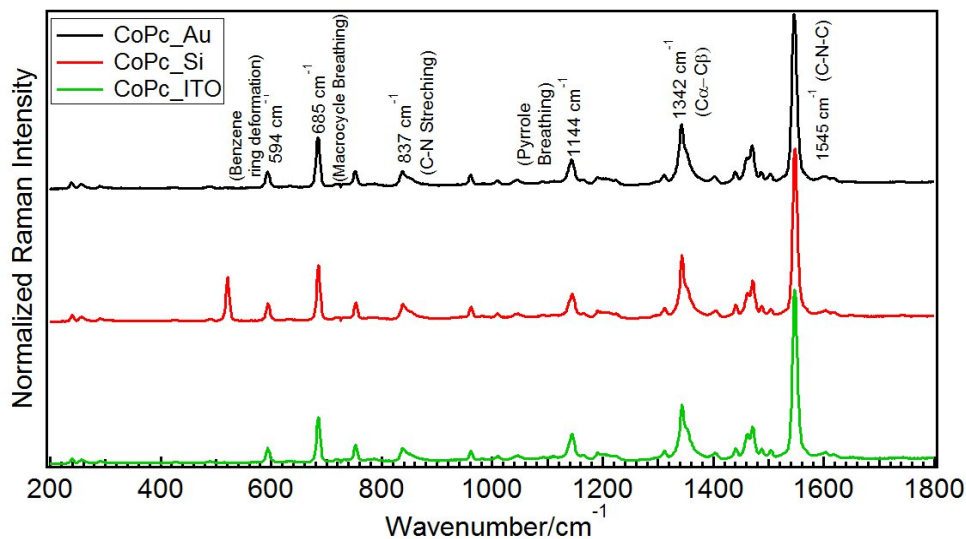
Figure 16 Raman spectrum of CoPc films on polycrystalline Au, SiOx/Si and ITO substrates
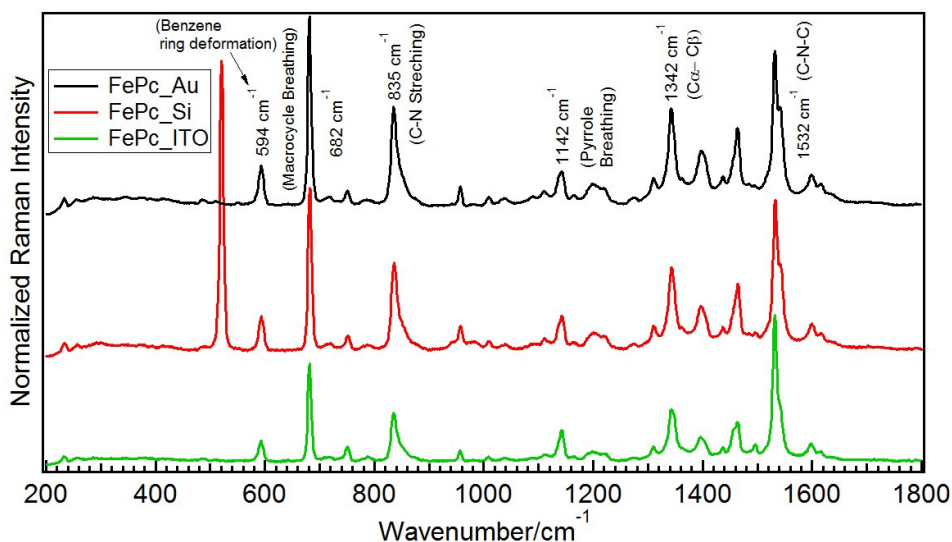
Figure 17 Raman spectrum of FePc films on polycrystalline Au, SiOx/Si and ITO substrates.

The relative intensity ratio of vibrational bands can be used to distinguish between polymorphic phases.[22] The relative intensity of the peak at about 750cm^{-1} is lower than the peak at about 684cm^{-1} which is characteristic feature of alpha polymorph phase while the intensity ratio is reversed for β phase.[49] The region between 600cm^{-1} to 800cm^{-1} in Figure 18 shows that relative intensity ratio of the peaks at about 750cm^{-1} and at about 684cm^{-1} is reversed for the FePc bulk, α and β phases along with thin film α phase for the deposition on Au. In addition considerable modifications for the vibrational Raman Bands are observed for the powder bulk phase as compared to thin films phase demonstrating the influence of unique molecular stacking in these phases. In order to analyze the intensity variation among different modes we have

51

normalized the spectra to the intensity of C-N-C vibrational mode for the deposition on SiO_x/Si. In order to decipher the molecular stacking of self assembled thin films of CoPc and FePc we have monitored the intensity of mode corresponding to macrocycle breathing vibration at $685 cm^{-1}$ as this mode most probably be effected by intermolecular interactions.

The Figure 19 shows the variation of relative intensity of macrocycle breathing mode with respect to the film roughness as acquired from AFM image analysis. The intensity of the macrocycle breathing mode is least for the deposition of FePc and CoPc on ITO. The intensity variation follows the trend of surface roughness in case of CoPc deposition while for the FePc deposition on Au, it shows maximum value. Molecular orientation and films growth are influenced by surface roughness, lattice structure as well as chemical interaction with substrate.[23]
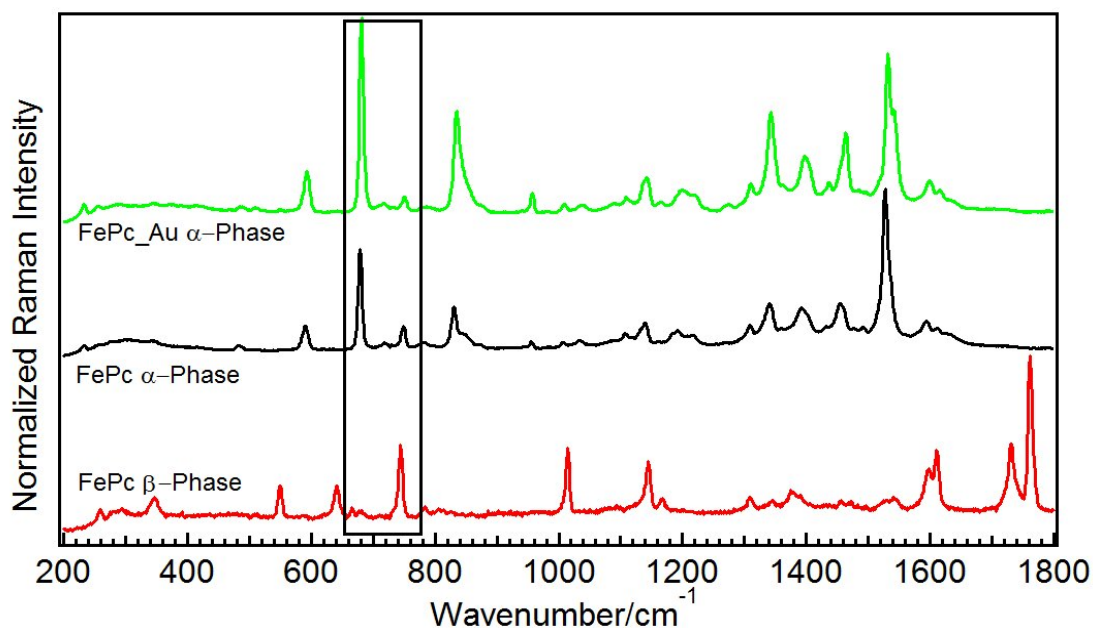
Figure 18 Raman spectrum of the FePc α and β crystalline powders along with α-phase FePc thin film on Au.

Based on X-ray absorption studies it has been observed that metal phthalocyanine molecules tend to adopt standing configuration with increase in substrate roughness.[50] As the intensity of Raman bands depend on crystal orientation and polarization geometry,[51] we can associate the intensity variation of the macrocycle breathing mode to the average molecular orientation. Due to higher surface roughness of ITO and weaker chemical interaction as compared to SiO_x/Si and Au disordered and standing configuration of molecules can be expected. Moreover in the absence of stronger molecule-substrate interactions weaker intermolecular interactions dominate and molecules adopt standing configuration.[52] Comparatively higher intensity for the deposition of FePc on Au as compared to CoPc can be associated to the different interaction and growth mechanism induced by the different central metal atom. Importantly dissimilarity in the

FePc and CoPc growth mechanism on Au is evident from AFM analysis which depicts elongated and dense FePc grains as compared to spherical CoPc grains. It has been observed for the deposition of CuPc on Au that molecules adopt lying configuration with respect to substrate during initial growth of first few layers due to higher interaction of π electron cloud with metallic substrate. [53] However for the deposition on ITO molecules are not expected to adopt lying configuration in the absence of stronger molecule-substrate interactions. In addition AFM analysis shows that grain size and surface roughness is relatively higher for ITO as compared to Au and SiO$_x$/Si. Thus we can associate the observed variation in the macrocycle breathing mode intensity to the unique molecular orientation adopted by CoPc and FePc molecules under the unified influence of substrate roughness, lattice structure and molecule-substrate interactions.
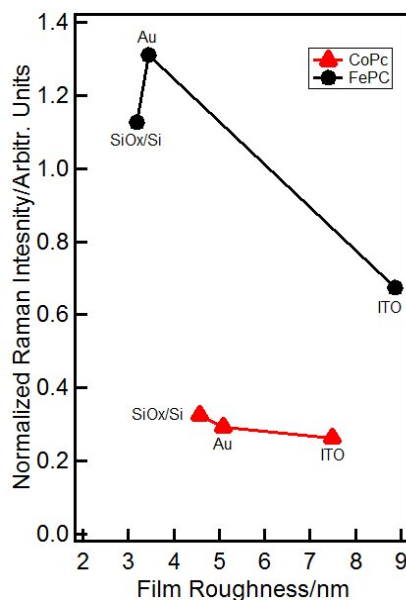
Figure 19 Variation of macrocycle breathing mode normalized intensity with film roughness.

3.5 Interrelation between structural and dynamical Properties of CoPc thin films

The physical properties of MPc thin films can be notably altered due to wide range of possibilities offered by the change of central metal atom and peripheral as well as axial groups. There has been considerable interest in the utilization of MPc thin films in optoelectronic devices because of their favorable optical properties. Due to their potential optoelectronic applications, considerable attention has been given to understand the dynamical properties of MPc molecular films. MPc TFs show inhomogeneous broadening of optical absorption bands in the solid state as compared to solution phase due to molecular distortions in the solid state. Among MPc

molecules CoPc molecular films exhibits strong absorption in the visible region (Q band) as well as near 330 nm (Soret band).[54]

In this section, we intend to correlate the dynamical properties of CoPc thin films with structural phases adopted by CoPc molecules. The orientation of the molecules in the thin films varies depending on various factors such as the choice of substrate, the deposition procedure, and the substrate temperature during deposition. Since the mode of molecular stacking and thus the opto-electronic properties affect the electrical and photoconductivity of the devices, their determination is of interest in order to model the performance of organic opto-electronic devices and to improve their efficiency. As discussed in previous section that MPc molecules exhibits α-polymorphism for the room temperature deposition. However, adsorption geometry of MPc TFs strongly depends on surface properties of substrate.[55]

Here, we investigate the impact of the substrate on the growth of a multilayer film. In case of MPc deposition on graphene, the topographic corrugation of the graphene also impacts the adsorption geometry.[56] STM studies show that MPc form a square lattice on epitaxial graphene on SiOx and hexagonal lattic on Au(111) as shown in Figure 18.[56] It is important to note that we obtained two types of crystalline CoPc TFs simply by varying the substrate, without changing evaporation rate and sample temperature. Hence, we can state that the particular substrate is able to alter not only the properties of the first layer of molecules, but also the crystal phase of the molecular film up to tens of nanometers. In other words, the registry of first layer governs the molecular stacking of subsequent layers during TF growth.

Interestingly, Q band of MPc corresponding to absorption in visible region presents a single peak in gas phase. However, in the solid state the molecules get distorted and degeneracy of LUMO can be removed. It results in splitting of Q band peak in optical absorption spectrum.[55] Moreover, optical absorption spectrum corresponding to α and β-polymorphs are found to be different confirming that absorption properties are significantly affected by crystal structure and relative orientation of molecules.[55] Here, we investigate the dynamical properties of CoPc TFs presenting different molecular stacking in the α-polymorphism using visible pump-probe technique.
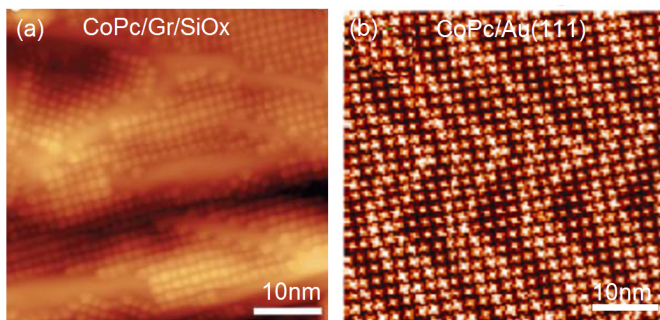

Figure 20 (a) STM image demonstrating that CoPc molecules adopts square lattice on Gr/SiOx while (b) CoPc molecules presents hexagonal symmetry on Au(111) [Reproduced from ref. 56]

It is evident from GIXRD analysis that CoPc molecules adopt a mixed phase configuration on polycrystalline gold, SiOx/Si and ITO, i.e. CoPc molecules exhibits coexistence of herringbone and brickstone molecular arrangements belonging to α polymorphism. Dynamical study performed for the 600nm thick CoPc films on quartz reveal that CoPc shows much faster dynamics as compared to H_2Pc, highlighting the significance of Co 3d states in the relaxation process.[57] It has been proposed that hybridization of Co 3d states with ligand π orbitals can give rise to new energy relaxation mechanisms.

Due to dissimilar molecular stacking in case of herringbone and brickstone structural phases, the intermolecular separation between adjacent CoPc molecules is distinct; therefore, the energy relaxation processes depending on intermolecular interactions among adjacent Co ions can be notably impacted. However, in order to highlight the significance of Co ions in the dynamical processes, it is important to deposit CoPc thin films with a dominant structural phases instead of a mixed phase. Figure 21 shows the GIXRD reciprocal space maps for the deposition of CoPc on Gr/SiOx and Au(111). Comparison of reciprocal space maps confirms the notable structural differences. Multiple diffraction spots are observed on both cases suggesting that CoPc molecules adopts an ordered structure on Gr/SiOx and Au(111) for thickness ≤40nm. In order to identify the polymorphism and molecular orientation adopted by CoPc molecules, we have compared these reciprocal space maps with the reciprocal space maps for CuPc adsorbed on $ZnO(1\bar{1}00)$.[36] Indexing has been performed for the CuPc deposition on $ZnO(1\bar{1}00)$ corresponding to herringbone and brickstone phases utilizing Simdiffraction software. The simulation assign peaks around $Q_{xy}=0.5$ Å^{-1}, Q_z ~0.5, 1,0 Å^{-1} and $Q_{xy}=1.7$, 1.9 Å^{-1}, Q_z ~0.27 Å^{-1} to herringbone (200) oriented phase.[36]
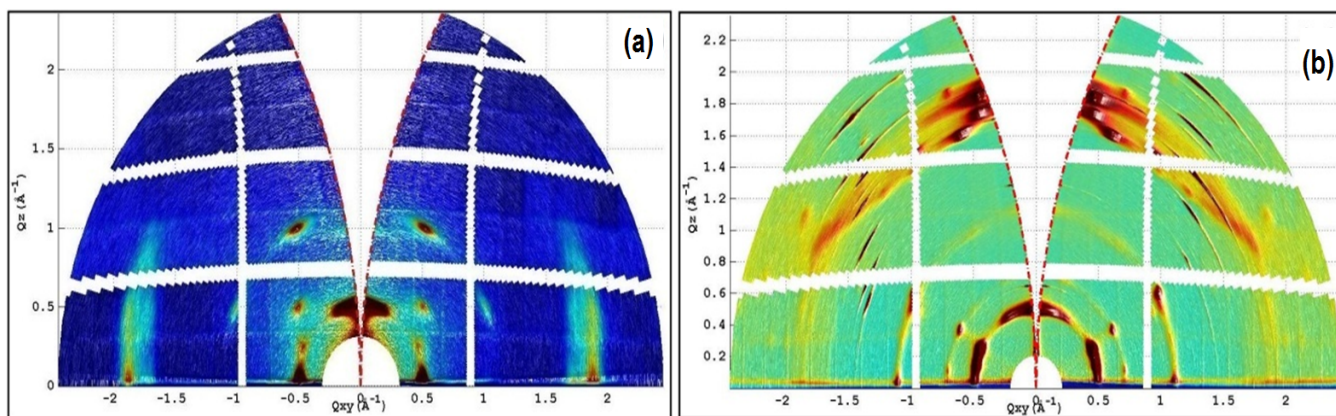

Figure 21 GIXRD reciprocal space maps for the deposition of CoPc on (a) Gr/SiOx and (b) Au(111)

Our reciprocal space map for the deposition of CoPc on Gr/SiOx exhibits good resemblance with the herringbone peak positions suggesting that herringbone phase is dominant in case of CoPc/Gr//SiOx as shown in the Figure 21. In case of CoPc on Au(111) diffraction spots

corresponding to herringbone phase are less pronounced. Therefore, it can be inferred that there are notable differences in the structural phases adopted by CoPc on Gr/SiOx and Au(111).

In order to further investigate the average CoPc molecular orientation on Gr/SiOx and Au(111) substrates, Co L_3 edge a_{1g} intensity has been analyzed corresponding to different angle of incidence of X-ray radiations with respect to substrate. As mentioned in the previous section this feature of CoPc is formed by out of plane d_{z2} state therefore its intensity variation with respect to angle of X-ray incidence provide the average orientation of the molecular orientation.

As shown in Figure 22 the trend of a_{1g} intensity variation complements the inferences drawn from GIXRD analysis; CoPc adopts predominantly a herringbone molecular orientation. In case of CoPc/Au(111) the a_{1g} intensity decrease monotonically suggesting that the dominant structural phase on Au(111) is brickstone.

According to reference 57, due to the proximity of molecular planes out of plane Co $3d_{z2}$ orbitals can give rise to delocalized exciton state. Such exciton states can facilitate transfer of excitation energy among adjacent molecular planes in the crystalline film. As we mentioned above there are notable differences in the molecular orientation of CoPc molecules on two substrates. Therefore, charge transfer related to exciting states as well as intermolecular interactions can be significantly affected.
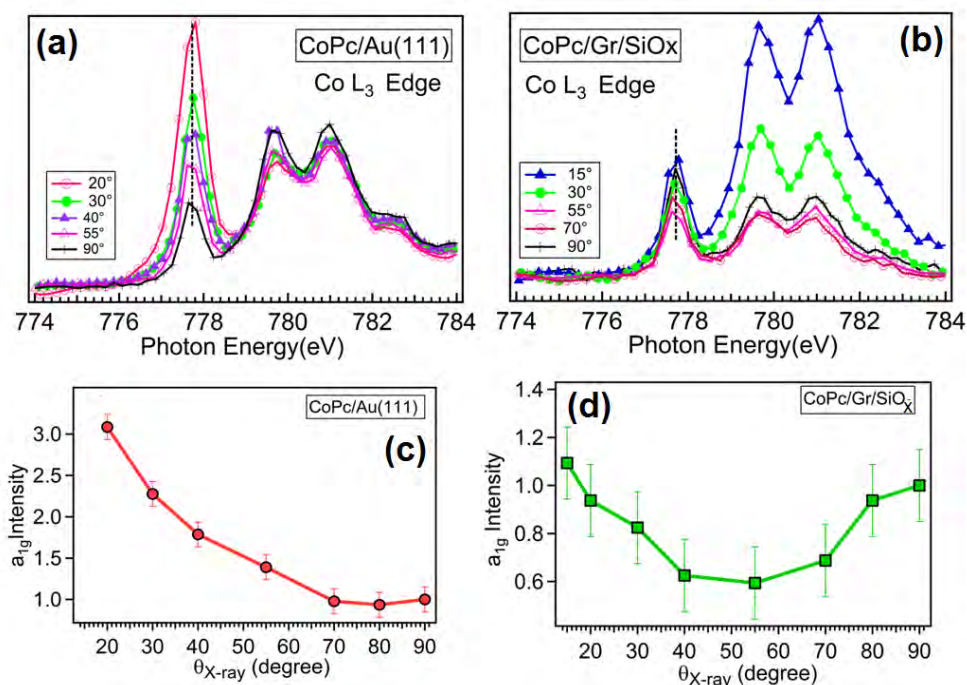

Figure 22 Co L_3 edge for the deposition of CoPc on (a) Au(111) and (b) Gr/SiOx along with intensity variation of a_{1g} state with angle of incidence for (c) CoPc/Au(111) and (d) CoPc/Gr/SiOx.

A brief description of pump probe experimental set up is given in chapter 2. In general, ultra short laser pulses are prerequisite to investigate ultrafast relaxation processes, which occur on a timescale of a few femtoseconds. The pump pulse interacts with the system of interest, after which the time-dependent transient changes of the absorption of the system is monitored by the probe beam. This transient change contains clues to both structural information and dynamics. The time resolution of the system is defined by the pulse duration.

In our experimental set up, probe beam is a covers from 450nm to 1100 nm. The measurements of the CoPc TFs were performed in reflection mode as shown in chapter 2. Typically, after excitation by laser, transient changes in the TFs are examined by probe pulse at a specific delay time, by measuring the ntensity variation of the reflected light by the sample. Two consecutive reflected spectra with pump on and pump off are collected and the wavelength dependent absorbance difference is measured for each delay.

Specifically, the differential reflection rate $\Delta R/R$ measurements (i.e. the variation of reflection ΔR during time delays and normalized to the un-pumped reflection R) are carried out by evaluating differential changes in the intensity of the probe pulses reflected by the pumped and un-pumped sample.

$$(I_{Pumped} - I_{unpumped})/ I_{Unpumped} = \Delta I/I$$

Such a signal is then measured as a function of the delay between the two pulses.

Figure 23(a,b) shows the differential reflection rate $\Delta R/R$ for the CoPc thin films on Gr/SiOx and Au(111) for various time delays as a function of probe wavelength. The excitation photon wavelength ($E = hc / \lambda$)in both the cases is 512 nm. It is evident that time resolved spectra show absorption bleaching (positive values) as well as induced absorption (negative values) in the region of Q-band, as shown in the bottom panel. The spectral shape of the curves varies with time delays. Similar variations in the spectral shape of time resolved spectrum has been observed for other metal phthalocyanines. It can be inferred that absorption bleaching intensity shows maxima around 558nm for 0.5ps time delay while at longer time delays the absorption bleaching becomes maximum at around 676nm.

The structure of absorption bleaching is quite broad and exhibits similarity to the linear absorption of the CoPc films in agreement with previous measurements of metal phthalocyanine films. As shown in Figure 23 the absorption bleaching exhibits broader maxima at different time delays. It indicates that after the excitation pump pulse, the probe investigates states with different population having distinct nature (singlet or triplet) and life time.
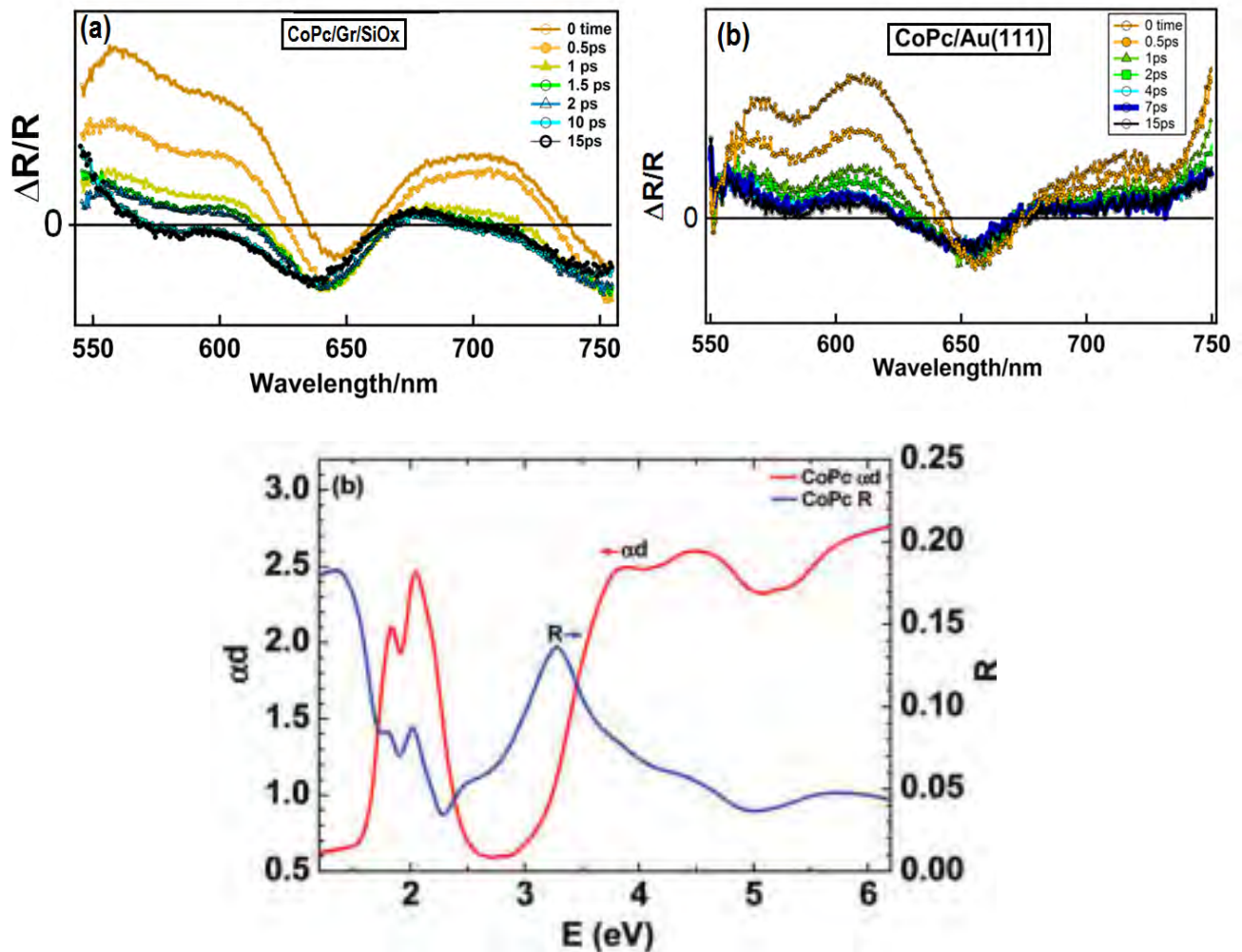
Figure 23 Top: Differential reflection rate ΔR/R for the CoPc thin films on (a) Gr/SiOx and (b) Au(111) for various time delays as a function of probe photon energy. Bottom: Optical absorption and reflection spctra in CoPc film in the ultraviolet and visible photon energy regions.[57]

We can rationalize the decay process of CoPc TF utilizing a proposed model [57] as shown in Figure 24. According to the model CoPc films excitation involves transition from ground state (S_0) to excited states (S_1, T_1). The vibronic states associated with molecular electronic states are also shown. The absorption bleaching observed at about 610 nm can be associated to the Pauli blocking in the S_1 state. It results in the decrease of transition probability from the S_0 state. Induced absorption is due to the population in the S_1 which decay to Triplet state by intersystem crossing and populate T1. It leads to transition from triplet state T_1 to higher energy triplet state T_2. The induced absorption observed at about 646nm is not observed for metal free phthalocyanines.[57]
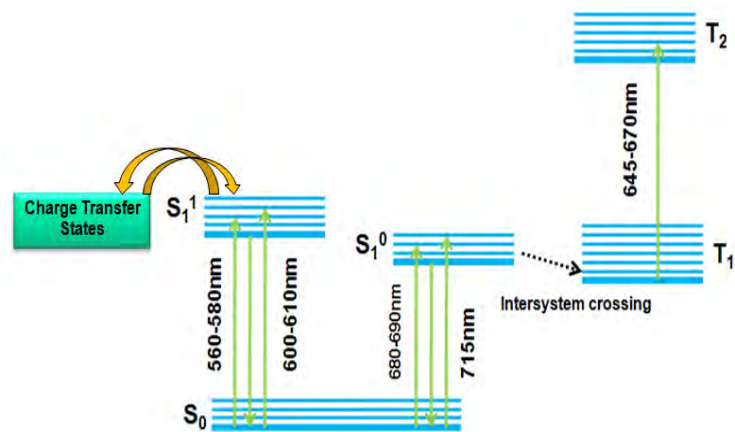
Figure 24 Energy-level model describing the induced absorption or transmission structures for CoPc films.

Analysis of the temporal variation of the differential reflection rate ΔR/R shows that for decay around 610 nm a double exponential function is needed to improve the fit quality (Figure 25). It suggests that more than one type of decay mechanism is active in this spectral region. It is worthwhile to mention that CoPc films show much faster relaxation dynamics of excited states as compared to metal free phthalocyanines. Moreover, presence of Co ion in the macrocycle significantly modifies the HOMO states of molecule. Therefore, the hybridization of central metal atom 3d orbitals with the π-orbitals of macrocycle provides extra decay channels or fast relaxation is also possible by charge transfer states. The analysis is still in progress, tentatively we assign the first decay time of 0.4 to 0.6 ps to internal conversion involving electron–phonon coupling[57] whilethe second process much slower could be associated to the charge transfer due to the delocalized exciton states.(Table 4)
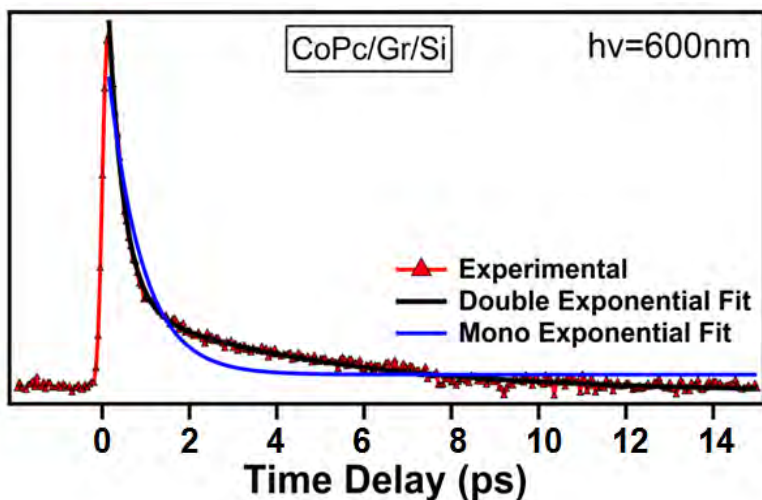
Figure 25 Analysis of the temporal variation of the differential reflection rate ΔR/R for decay around 610nm

Induced Transmission	λ (nm)	τ_1 (ps)	τ_2 (ps)
CoPc/Au(111)	610	0.51 ± 0.28	3.34 ± 0.39
	688	0.59 ± 0.28	No data
	715	0.71 ± 0.28	No data
CoPc/Gr/SiOx	600	0.35 ± 0.28	4.62 ± 0.28
	678	0.45 ± 0.28	No Data
	710	0.54 ± 0.28	No Data

Table 5

The Figure 26 shows the excitation dynamics of CoPc thin films deposited on Gr/SiOx and Au(111) for the delay time of 0.5ps. It is evident that there is a blue shift (higher energy, lower wavelength) in the Gr/SiOx spectrum in the 610 nm range as compared to Au(111). The model suggest that the transition in the 610nm range involes singlet states S_0 and S_1 sates. We tentatively assign the blue shift measured to the dissimilar molecular stacking in the herringbone and brickstone structural phases. Further analysis along with theoretical calculations is still in progress.
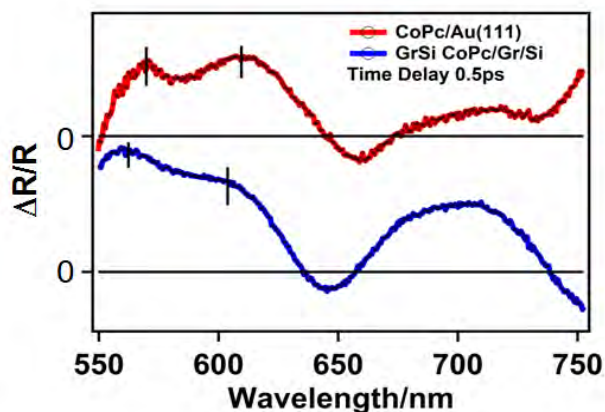
Figure 26 Excitation dynamics of CoPc thin films deposited on Gr/SiOx and Au(111) for the delay time of 0.5ps.

References

[1] M. Pfeiffer, K. Leo, X. Zhou, J. S. Huang, M. Hofmann, A.Werner, Blochwitz-Nimoth, J. Org. Electron. 4, 2003, 89−103.

[2] M. V. Martinez-Diaz, G. de la Torre, T. Torres, Chem. Commun. 46, 2010, 7090−7108.

[3] J. G. Mei, Y. Diao, A. L. Appleton, L. Fang, Z. N. Bao, J. Am. Chem. Soc. 135, 2013, 6724–6746.

[4] S. Reineke, M. Thomschke, B. Lussem, K. Leo, Rev. Mod. Phys. 85, 2013, 1245–1293.

[5] F. Schmitt, J. Sauther, S. Lach, C. Ziegler, Anal. Bioanal. Chem. 400, 2011, 665−671.

[6] T. Kroll, R. Kraus, R. Schönfelder, V. Y. Aristov, J. Chem. Phys. 137, 2012, 054306.

[7] I. E. Brumboiu, S. Haldar, O. Eriksson, H. C. Herper, B. Brena, B. Sanyal, J. Chem. Theory Comput. 12, 2016, 1772−1785.

[8a] N. Marom, O. Hod, G.E. Scuseria, L. Kronik, J. Chem. Phys. 128, 2008, 164107.
[8b] N. Marom,· L. Kronik, Appl Phys A 95, 2009,159–163

[9] N. Papageorgiou, Y. Ferro, E. Salomon, A. Allouche, J. Layet, L. Giovanelli, G. Le Lay, Physical Review B 68, 2003, 1–10.

[10] T. Kroll, V. Y. Aristov, O. V. Molodtsova, Y. A. Ossipyan, D. V. Vyalikh, B. Buchner, M. Knupfer, J. Phys. Chem. A 113, 2009, 8917–8922.

[11] T. Kroll, R. Kraus, R. Schonfelder, V. Y. Aristov, O. V. Molodtsova, P. Hoffmann, M. Knupfer, J. Chem. Phys. 137, 2012, 054306.

[12] A. Rosa, E. J. Baerends, Inorganic Chemistry 33, 1994, 584–595.

[13] P. Gargiani, G. Rossi, R. Biagi, M. Pedio, S. Fortuna, A. Calzolari, S. Fabris, J. C. Cezar, N. Brookes, M. G. Betti, Phys. Rev. B 87, 2013, 165407.

[14] F. Bartolomé, O. Bunəu, L. M. García, C. R. Natoli, M. Piantek, J. I. Pascual, I. K. Schuller, T. Gredig, F. Wilhelm, A. Rogalev, J. Bartolomé, J. Appl. Phys. 2015; 117, 735.

[15] T. Zhang, I. Brumboiu, V. Lanzilotto, J. Lüder, C. Grazioli, E. Giangrisostomi, R. Ovsyannikov, Y. Sassa1, I. Bidermane, M. Stupar, M. de Simone, M. Coreno, B. Ressel, M. Pedio, P. Rudolf, B. Brena and C. Puglia , J. Phys. Chem. C20171214726372-26378

[16] S. Fortuna, P. Gargiani, M. G. Betti, C. Mariani, A. Calzolari, S. Modesti, S. Fabris, J. Phys. Chem. C 116, 2012, 6251–6258.

[17] L. Floreano, A. Cossaro, R. Gotter, A. Verdini, G. Bavdek, F. Evangelista, A. Ruocco, A. Morgante, D. Cvetko, J. Phys. Chem. C 112, 2008, 10794-10802

[18] Munataka, T. Ueba, J. Park, R. Terawaki, Y. Watanabe, T. Yamada, T. Munakata, Surface Science 649, 2016, 7–13.

[19] J. Xiao, P. A. Dowben, J. Mater. Chem. 19, 2009, 2172.

[20] J. Uihlein, H. Peisert, H. Adler, M. Glaser, M. Polek, R. Ovsyannikov, M. Bauer, T. Chassé, J. Phys. Chem. C 118, 2014, 28671–28678.

61

[21] G. Rojas, X. Chen, C. Bravo, J. Kim, J. Phys. Chem. C 114, 2010, 9408.

[22] L. Floreano,A. Cossaro, R. Gotter, A. Verdini, G. Bavdek, F. Evangelista, A. Ruocco, A. Morgante, D. Cvetko, J. Phys. Chem. C 112, 2008, 10802.

[23] P. Gargiani, G. Rossi, R. Biagi, M. Pedio, S. Fortuna, A. Calzolari, S. Fabris, J. C. Cezar, N. Brookes, M. G. Betti, Physical Review B 87, 2013, 165407.

[24] M. G. Betti, P. Gargiani, R. Frisenda, R. Biagi, A. Cossaro, A.Verdini, L. Floreano, C. Mariani, J. Phys. Chem. C 114, 2010, 21638–21644.

[25] F. Evangelista, A. Ruocco, R. Gotter, A. Cossaro, L. Floreano, A. Morgante, F. Crispoldi, M. G. Betti, C. Mariani, J. Chem. Phys. 131, 2009, 174710.

[26] P. Gargiani, M. Angelucci, C. Mariani, M. G. Betti, Physical Review B 81, 2010, 085412.

[27] D. E. Barlow, L. Scudiero, K. W. Hipps, Langmuir 20, 2004, 4413.

[28] F. Petraki, H. Peisert, I. Biswas, T. Chasse, J. Phys. Chem. C 114, 2010, 17638.

[29] A. Ruocco, F. Evangelista, R. Gotter, A. Attili, G. Stefani, J. Phys. Chem. C 112, 2008, 2016.

[30] M. Gorgoi, W. Michaelis, T. U. Kampen, D. Schlettwein, D. R. T. Zahn, App. Surf. Sci. 234, 2004, 138.

[31] C. M. Gorgoi, D. R. T. Zahn, Organic Electronics 6, 2005, 168.

[32] F. Evangelista, A. Ruocco, V. Corradini, M. P. Donzello, C. Mariani, M. G. Betti, Surface Science 531, 2003, 123.

[33] R. A. Bartynski, R. H. Gaylord, T. Gustafsson, E. W. Plumme Physical Review B 33, 1986, 3644.

[34] P. L. Cook, W. Yang, X. Liu, J. M. García-Lastra, A. Rubio, F. J. Himpsel, J. Chem. Phys. 134, 2011, 204707.

[35] M. Szybowicz, W. Bała, S. Dümecke, K. Fabisiak, K. Paprocki, M. Drozdowski, Thin Solid Films 520, 2011, 623.

[36] A. C. Cruickshank, C. J. Dotzler, S. Din, S. Heutz, M. F. Toney, M. P. Ryan, J. Am. Chem. Soc. 134, 2012, 14302.

[37] J. Bartolomé, C. Monton, I. K. Schuller, Molecular Magnets Physics and Applications, 2014 Springer.

[38] C. Defeyt, P. Vandenabeele, B. Gilbert, J. Van Pevenage, R. Cloots, D. Striva*y, J. Raman Spectros*c. **2**012*;* 43, 1772.

[39] A. O. F. Jones, B. Chattopadhyay, Y. H. Geerts, R. Resel, Adv. Funct. Mater. 26, 2016, 2233

[40] H. Peisert, X. Liu, D. Olligs, A. Petr, L. Dunsch, T. Schmidt, T. Chassé, M. Knupfer, J. Appl. Phys. 96, 2004, 4009.

[41] K. Vasseur, K. Broch, D. Cheyns, ACS Appl. Mater. Interfaces 5, 2013, 8505.

[42] H. Peisert, T. Schwieger, J. M. Auerhammer, M. Knupfer, M. S. Golden, J. Fink, P. R. Bressler, M. Mast, J. Appl.Phys. 90, 2001, 466.

[43] G. Scavia, L. Barba, G. Arrighetti, S. Milita, W. Porzi*o, Eur. Polym.* **J. 2**012*;* 48, 1050.

[44] M. Krzywiecki, L. Grzadziel, J. Phys. D 47, Appl. Phys. 2014, 335304.

[45] K. Vasseur, K. Broch, D. Cheyns, ACS Appl. Mater. Interfaces 5, 2013, 8505.

[46] C. Jennings, R. Aroca, A.-M. Hor, R. O. Loutfy, J. Raman Spectrosc. 15, 1984, 34.

[47]. D. R. Tackley, G. Dent, W. E. Smith, Phys. Chem. Chem. Phys. 3, 2001, 1419

[48] R. Prabakaran, R. Kesavamoorthy, G. L. N. Reddy, F. P. Xavie*r, Phys. Stat. S*o**l. 2**002*;* 229, 1175.

[49] S. Heutz, S. M. Bayliss, R. L. Middleton, G. Rumbles, T. S. Jone*s, J. Phys. Chem.* **B 2**00*0;* 104, 7124.

[50] H. Peisert, I. Biswas, M. Knupfer, T. Chass*é, Phys. Status Solidi Basic R*e**s. 2**00*9;* 246, 1529.

[51] M. Szybowicz, J. Makowieck*i, J. Mater. S*c**i. 2**012*;* 47, 1522.

[52] H. Peisert, I. Biswas, L. Zhang, M. Knupfer, M. Hanack, D. Dini, D. Batchelor, T. Chass*e, Surf. S*c**i. 2**006*;* 600, 4024.

[53] I. Biswas, H. Peisert, M. Nagel, M. B. Casu, S. Schuppler, P. Nagel, E. Pellegrin, T. Chass*e, J. Chem. Phy*s**. 2**00*7;* 126, 174704.

[54] S. Karan, B. Mallik, Solid State Comm. 143, 2007, 289–294.

[55] G. M. Pierantozzi, M. Sbroscia, A. Ruocco, Surface Science 669, 2018, 176–182.

[56] K. Banerjee, P. Hakkinen, A. Harju, P. Liljeroth, Nano Letters 13, 2013, 3199−3204.

[57] A. Gadalla, J.-B. Beaufrand, M. Bowen, S. Boukari, E. Beaurepaire, O. Cre´gut, M. Gallart, B. Honerlage, P. Gilliot, J. Phys. Chem. C 114, 2010, 17854–17863.

Chapter-4

Weakly interacting Octaethylporphyrin systems: Influence of intermolecular interactions on physical properties

4.1 Introduction

Metal octaethyl porphyrin (MOEP) molecules are an important class of transition metal complexes due to their favorable optical and electronic properties. Metal octaethyl porphyrin molecular thin films have been explored for optoelectronic applications such as solar cells and light emitting diodes. [1] However, device performance strongly depends on quality of the molecular films and their interface with electrodes. Therefore, detailed understanding of various factors influencing optical, vibrational and electronic properties of molecular thin films such as molecular order, crystallinity and intermolecular interactions is important.[2] Intermolecular interactions play a major role and are notably influenced by the type of central metal atom as well as nature of peripheral groups.[2] In case of metal octaethyl porphyrin molecules ethyl groups can adopt different orientations in order to minimize steric hindrance and to obtain energetically stable configuration.[3] Similar to MPc molecules, the different 3d filling of central metal atom in case of MOEP molecules can notably impact the molecular orbitals MOs energy level alignment, thereby influencing the interaction of porphyrin molecules with underling substrate.[4] It is worth noting that the splitting of 3d-orbital energy levels in ligand fields described for MPc take place also in porphyrins, and depends on the oxidation state of the central atom and the marocycle different symmetries.(See appendix)

In order to gain thorough understanding of the impact of central metal atom 3d character, we have compared the gas phase valence band spectrum of the octaethylporphyrin molecules investigated in this thesis. As shown in Figure 1 the valence band spectrum of H_2OEP is notably modified as compared to metal octaethylporphyrin molecules spectrum close to HOMO level energy position. However, there is apparent similarity in the ZnOEP and CuOEP valence band spectra in the energy region between 6-9eV. A strong modification of valence band spectrum is observed in case of NiOEP highlighting the fact that insertion of Ni in the OEP macrocycle dramatically affects the electronic structure.

Here, we investigates the basic mechanisms in the ordering of single layers of large molecules onto surfaces and the role played by the central atom in octaethylporphyrin molecules in their interaction with substrate and the effect of intermolecular interaction.

Molecular self assembly in ultrahigh vacuum conditions can provide good quality molecular films and interfaces. Thin film growth is governed by the fine interplay between molecule-

molecule and molecule-substrate interactions. In the absence of strong molecule-substrate interactions, intermolecular interactions among molecules such as non directional and feeble van der Waals plays crucial role in the molecular stacking. In addition, surface roughness, topographic and electronic properties of substrate also determines adsorption geometry and interaction strength. These factors strongly influence the interfacial electronic properties and energy level alignment.[5] As gold contacts are important for optoelectronic device fabrication and SiOx/Si and ITO are widely used in semiconductor industry, we have selected these substrates in our study. Moreover, these substrates interact weakly with MOEP so the impact of intermolecular interactions will be pronounced. As discussed in previous chapter the physical properties of MOEP TFs also have significant dependence on crystal structure and molecular stacking which in turn depends on substrate roughness and TF growth conditions.

Here, ZnOEP, CuOEP and NiOEP are here utilized to investigate weakly interacting porphyrin/substrate interfaces. Our spectroscopic investigation (photoemission, Inverse Photoemission, NEXAFS) reveals that these molecules interacts weakly with Au(111) substrate indicating that central metal atom orbitals are not involved in hybridization with underlying substrate. For this reason these molecules are chosen to highlight the influence of intermolecular interactions in the absence of strong substrate driven interactions such as hybridization, charge transfer and back donation of charge density etc.
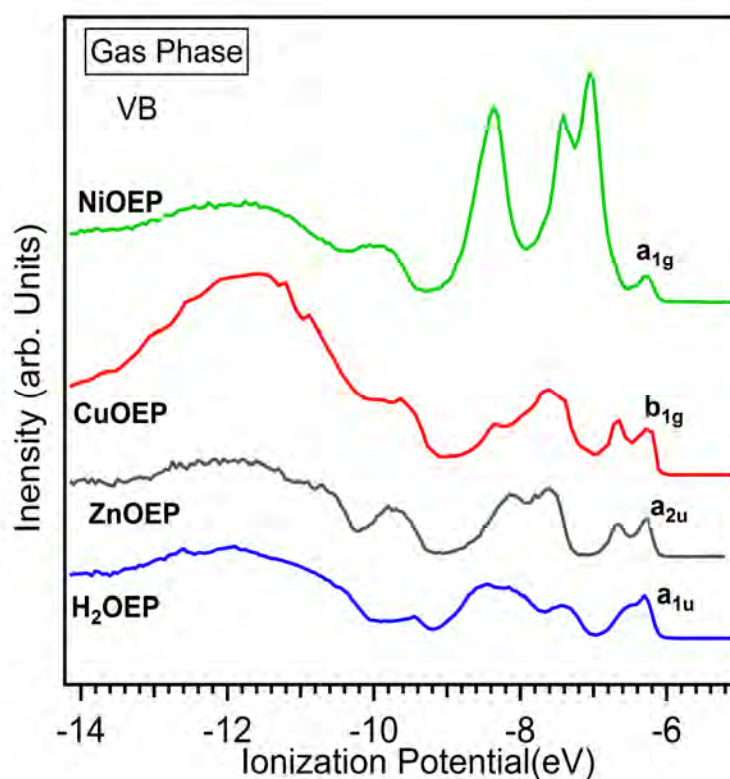

Figure.1 Gas phase valence band spectra of OEP molecules. (HOMOs are labeled) * Curtsey Andrea Goldoni

STM studies reveal that MOEP molecules arrange in well ordered structures in monolayer and multilayer regimes.[6] MOEP molecules are characterized by small peripheral ethyl groups. Due to which we could expect that they do not present strong conformational changes due to adsorption induced distortions in contrast to tetraphenyl porphyrins.[2] Actually DFT energy calculations (ruffling in NiOEP) were applied for the vibrational force calculation and contrary to other literature calculations the structural and vibrational analysis of NiOEP presents a more complex framework due to the various possible ethyl group orientations (NiOEP has 200 possible conformations with respect to the ethyl orientation of which 25 are unique, non redundant conformers).

STM analysis for the deposition of CoOEP and H_2OEP on Ag(111) show that the ethyl groups do not lead to adsorption induced structural distortions of the molecule in contrast to tetraphenyl porphyrin molecules.[7] Moreover, ethyl groups point away from the substrate and appear as four double-protrusions symmetrically surrounding the center suggesting that molecular conformational changes are independent of central metal atom and arrange in hexagonal lattice. Similar behavior has been observed for CoOEP on Au(111) and NiOEP on HOPG and Au(111).[5,8]

Detailed information about the HOMO and LUMO is important for the efficient use of molecular thin films in optoelectronic devices. Inverse photoemission spectroscopy provides access to the direct measurements of LUMO. Moreover, as discussed in the experimental techniques chapter, due to delocalization of unoccupied density of states, influence of molecular conformational changes can be investigated with IPES. We investigate the MOEP interfaces with Au(111) with IPES in order to study the impact of electrostatic and polarization effects on energy level alignment.

4.2 Weakly interacting MOEP interface with metallic substrate

Here, we present the formation of the interface between the Au(111) single crystal surface and the MOEP, namely CuOEP (copper(II) octaethyl porphyrin) and NiOEP. These interfaces are taken as model systems of weak interaction. Au(111) presents a prototypical model substrate to understand weakly interacting metal-molecule interfaces and relevant in organic electronics due to its applications in optoelectronic devices. In the adsorption of transition metal complexes in Au(111) generally the formation of interface dipole notably controls the energy level alignment at the interface.[6] However, in the absence of a strong metal–molecule interaction, electrostatic effects such as cushion effect plays significant role in interface dipole formation and energy level alignment. (See also chapter1).

The investigation of the surface reconstruction of the first monolayer adopted by molecules at the molecule-substrate interface is fundamental to enlighten the basic mechanism of their interaction with underlying substrate and interfacial electronic properties. Structural studies on these systems have been often based on scanning tunneling microscopy. However, the structural and

67

binding features of the contact region are not directly accessible by STM since this technique images the surface electron density of states, which, in the case of large molecules, is in general complicated for the buried interface electronic structure. Therefore, we chose inverse photoemission spectroscopy, though its result are averaged and not local as in STM to enlighten the impact of unique surface structural phases (domains in the 100 Å scale range) adopted by MOEP molecules on energy level alignment of frontier orbitals.

We focus our study on Inverse Photoemission characterization to enlighten the effect of the single layer aggregation and the possible impact of intermolecular interactions on MOs energy level alignment. As already mentioned the interest of such studies is due to the observation that empty orbitals are more sensitive to the intermolecular interaction due to their higher delocalization around the macrocycle. These states exhibits notable energy separation as compare to filled states induced by alterations in the molecular arrangements which makes inverse photoemission spectroscopy technique more sensitive to molecular perturbations.

4.2.1 CuOEP on Au(111)

Similarly to other substrates [9] adsorption of the CuOEP on the Au(111) is not related to hybridization (governed by weak interaction). No significant chemical shift and/or alterations in Au $4f^{7/2}$ and $4f^{5/2}$ high resolution core level spectral line shape have been observed after the deposition of CuOEP in monolayer regime and the MOEP single layer is completely removed after annealing at about 600 K. It confirms the weaker interaction of CuOEP with Au(111) similar to CuPc on Au(111).In general, appearance of core level shifts of the substrate would be a signature of chemical interaction. Figure 2 shows the LEED pattern for the single layer (1ML) CuOEP on Au(111). Most of the LEED spots can be interpreted by the two quasi hexagonal domains similar to √28 R 19.1°, in agreement with ref [10].
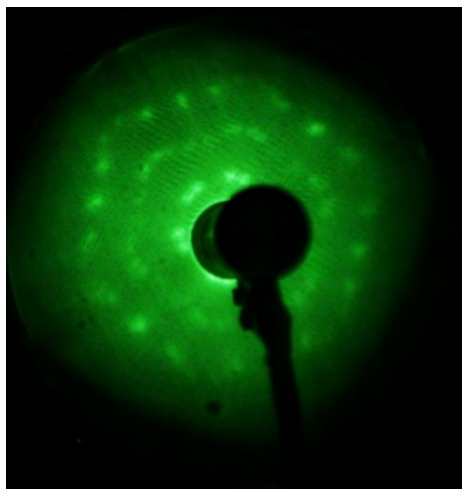

Figure 2 LEED image of 1 ML CuOEP on Au(111)

It is worth noting that the CuOEP deposition up to coverages < 0.75 ML does not lead to ordered molecular domains, and no reconstructed LEED is observable.

In order to obtain a comprehensive analysis of the impact of the weaker electrostatic and Van der Waals interactions on the energy level alignment, we analyzed the deposition of CuOEP on Au(111) with combined UPS in normal emission (performed at the CITIUS Laboratory, University of Nova Gorica) and normal incidence IPES. The precise determination of HOMO and LUMO energy positions, obtained by combined UPS-IPES can provide information about the HOMO-LUMO energy separation, an important parameter for optoelectronic devices [11].

Figure 3 shows the combined UPS-IPES spectra for the deposition of CuOEP on Au(111). It is evident from Figure 3 that for the deposition on CuOEP on Au(111) the emission near Fermi level is not suppressed completely for until ~1ML. The clean Au(111) IPS spectrum is characterized by an intense peak close (0.2 eV) to the Fermi level that corresponds to the surface states of the substrate; and the feature labeled Is at about 4.8 eV is the image states, in agreement with literature results.[12] The empty molecular states become prominent as the coverage increases beyond monolayer regime, as shown for the 3ML spectrum, and show slight energy shift. In particular the LUMO feature at 0.8 eV shows a small but notable shift towards the Fermi level as the coverage increases to about 3ML. These results suggests that there is no significant intermixing of 3d orbitals of central metal atom with the underlying substrate is detected confirming that the molecule-substrate interaction is weak in case of CuOEP /Au(111) system, without hybridization.

In case of CuOEP DFT calculation show that LUMO has a e_{2g} character predominantly related Cu 3d character in case CuOEP and separated by about 1.2 eV from the LUMO+1.[13] The energy position between LUMO and LUMO+1 in the IPES spectrum is approximately 1.2 V apart in agreement with DFT calculations.

IPES spectrum shows LUMO shifts towards the Fermi level for the deposition of CuOEP on Au(111) at 3ML coverages as shown in Figure 3. The energy separation is different in the monolayer regime which can be due to electrostatic and polarization effects (see Appendix). Similar shifts has been observed for the deposition of CuPc on weakly interacting H-Si(111) and can be attributed due to the change in molecular orientation of CuPc at higher coverages. As discussed in previous chapter coverage dependant shift of LUMO have been observed for CuPc deposition on Au(110). Importantly, it has been observed that change in the molecular orientation with thickness results in energy level shifts at the interfaces and significantly influences device performance.
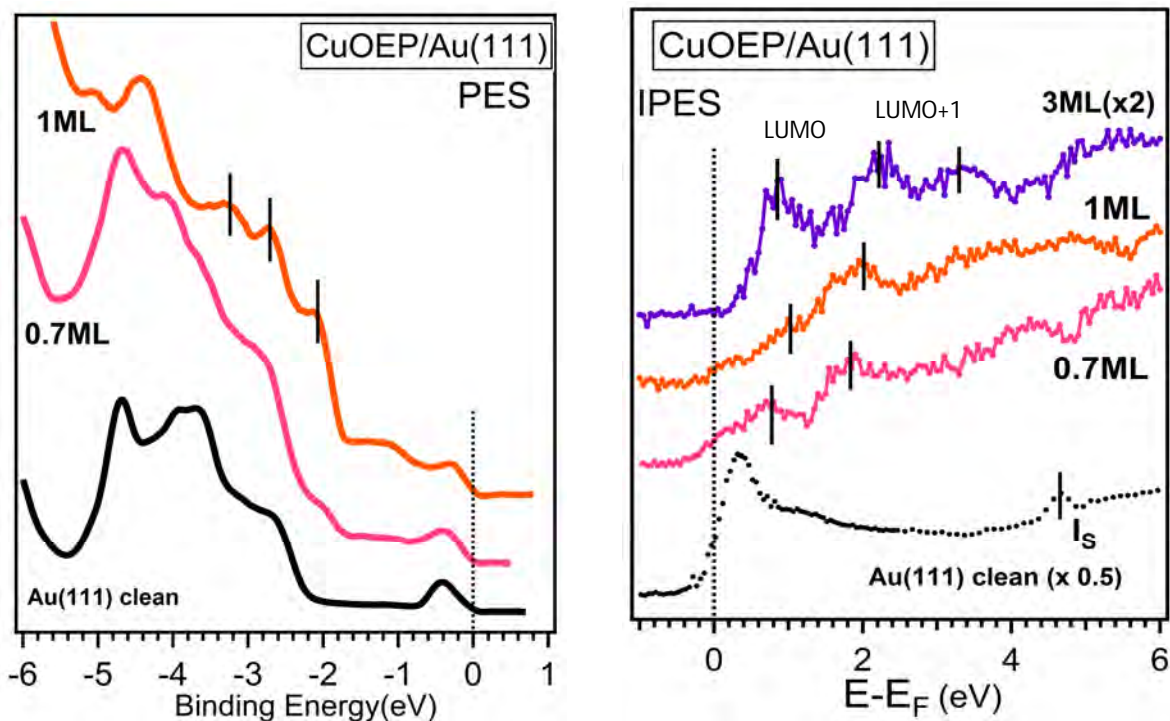
69

Figure 3 Valence band* and Normal Incidence Inverse photoemission spectra for CuOEP/Au(111)   * Courtsey Barbara Ressel

DFT calculations for CuOEP show the presence of two almost degenerate states near Fermi level having $a_{1u}(\pi)$ and $a_{2u}(\pi)$ symmetry. The CuOEP gas phase spectrum shown in Figure. 1 exhibits two sharp features between 0.8 eV and 1.8eV in accordance with DFT calculations.[38-40] Therefore, broader feature near Fermi level can be tentatively assigned to filled molecular ortbitals with a_{1u} and a_{2u} symmetry. Here, it is worthwhile to mention that energy level ordering at metal-organic interfaces also depends theoretical framework adopted for calculations.[9]

The peak at 2.8eV is due to gold substrate. It is worthwhile to mention that monolayer spectrum for the deposition of strongly CoOEP on Ag(111) shows a feature at about 0.6eV,which is due to the interaction of Co with underlying substrate and absent for H_2OEP on Ag(111). However, no such feature is observed for the deposition of CuOEP on Au(111) further excluding molecule-substrate hybridization. Thus, in the absence of stronger molecule-substrate interactions, weaker intermolecular interactions play significant role in molecular thin films. The filled states peak assignments are in good agreement with the literature results.[10] The peaks at about 2eV and 3.2eV can be assigned to HOMO and HOMO-1 and show good agreement with literature results for the deposition of CuOEP on Ag(111) and Ag(100). [6] STM studies show that ethyl group points 'up' i.e. they tend to orient away from the substrate to adopt stable configuration.

Our preliminary DFT calculations performed by Arrigo Calzolari (CNR-SPIN, Modena) found that CuOEP molecules with the conformer with all the ethyl group up, exhibit 2.25 D of dipole moment due to ethyl groups up configuration. It leads to slightly negatively charge porphyrin

70

ring while ethyl groups acquire positive charge. Finally we found that the work function of 1ML CuOEP/Au(111) is decreased of about 0.65 eV with respect to the clean Au(111). It indicates that in the absence of strong molecule-substrate interactions, electrostatic effects can impact the energy level alignment.

4.2.2 NiOEP on Au(111)

In continuation with our study to investigate the impact of intermolecular interactions in weakly interacting MOEP systems, interfacial electronic properties for the deposition of NiOEP on Au(111) has been investigated. In this case two different ordered molecular layers are observed in the submonolayer regime, in contrast to CuOEP. The cavity size for the prophyrin ring is 0.2nm and due to smaller size of Ni ion , N-Ni bond get shortened and pyrrole groups are pushed towards the centre of the ring resulting in macrocycle distortions.[5] Although, NiOEP molecule posses structural similarity with CuOEP, however, due to different central metal atom the intermolecular interactions can be significantly distinct.

The fact that the NiOEP molecules adopt two different structural phases on Au(111) can be ascribed, together with the weak bond with the substrate, to dissimilar intermolecular interactions, that impacts the charge distribution at the organic-inorganic interface, and the molecular orbital alignment.
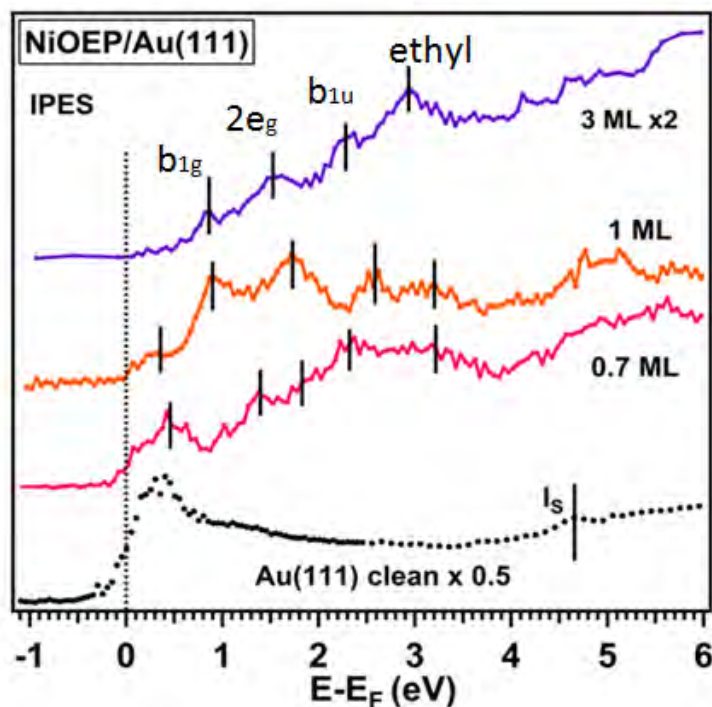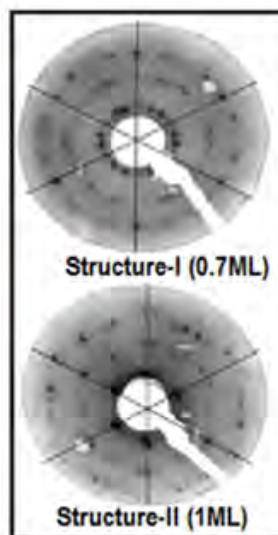

Figure 4(a)   Figure 4(b)

Figure 4(a)   IPES spectrum for the depsotion of NiOEP on Au(111) as function of coverage .(b) LEED images corresponding to 0.7ML and 1ML coverage

Figure 4(b) shows the LEED images of NiOEP molecules on Au(111) substrate corresponding to submonolayer and monolayer regime. It is evident that the molecular arrangement is unique for two coverages and there is clear signature of changes in molecular arrangment with submonolayer coverages. STM studies [5] confirm the ethyl-up configuration even in this case. DFT calculations found for this conformer a dipole of 0.64 D, lower with respect to the CuOEP similar case. In the monolayer regime the LEED spots can be interpreted by the two quasi hexagonal domains similar to CuOEP. However, LEED analysis indicates that in contrast to CuOEP where no ordered phase is found up to 0.75 ML, NiOEP adopts in two dissimilar molecular arrangements probably due to the balance between molecular dipole and intermolecular interactions among NiOEP molecules induced by different central metal atom.

Figure 4(a) shows the normal incidence IPES spectra taken as a function of NiOEP film thickness. The clean Au(111) and the 3ML NiOEP spectra are shown for comparison. The unocuppied molecular states becomes prominent with increasing film thickness of NiOEP molecules on Au(111).

More in detail, the empty orbitals of NiOEP are characterized by three peaks that originate by the Ni central atom and the porphine macrocycle ring. The assignments of the experimental features are labeled in Figure 4(a) according to the results obtained by our calculations. The first feature is assigned to the b_{1g} state that is related to the orbital with mainly Ni $3d(x^2 - y^2)$ character; the second is assigned to the $2e_g(\pi^*)$ degenerate orbital with organometallic character mainly due to the ligand N orbitals in the porphine cycle and partly to the C $2p^*$. The third peak is a b_{1u} orbital. The states at higher energies result densely distributed in energy and are mainly attributed to the external ethyl groups. In particular, we single out a strong contribution of the ethyl group to the intense IPES feature at 2.8 eV.

Theoretical calculations (Dr. Arrigo Calzolari) have been performed to calculate filled and unoccupied density of states for the assignments of IPES spectral features. The IPES spectrum solid line labeled 3 ML results more resolved. The broadening and/or shifting of the spectral features in the 15 ML is due to charge screening and polarization effects induced in the thick molecular film. Disordered molecular stacking at higher coverages could also contribute in broadening of spectral features The energy separation between LUMO and LUMO+1 is about 0.6eV which is in good agreement with IPES multilayer spectrum as shown in Figure 5(a) According to theoretical calculations the spectral features related to peripheral ethyl groups are between 3 to 4eV. As shown in Figure 4(a) emission near the Fermi level still persists without broadening at 1ML coverage, similarly to valence band spectra [10] indicating that there is no significnat intermixing of molecular frontier orbitals with underlying substrate. It can be inferred that similar to CuOEP, NiOEP also exhibits weaker intraction with Au(111). It is evident that energy separation between LUMO and LUMO+1 is notably different for 1ML as compared to 0.7ML coverage corresponding to two distinct ordered NiOEP structures. It shows that unoccupied density of states are sensitive to structural changes in the molecualr arrangements induced by intermolecular interactions. Simulation are in progress to rationalize these results.
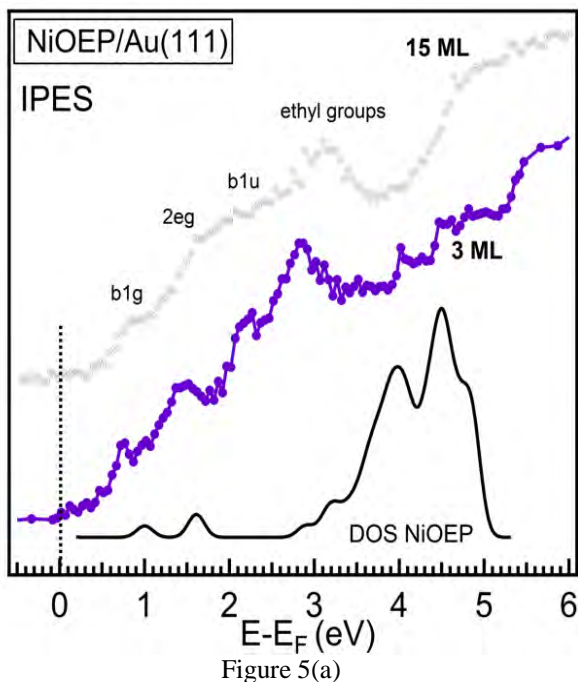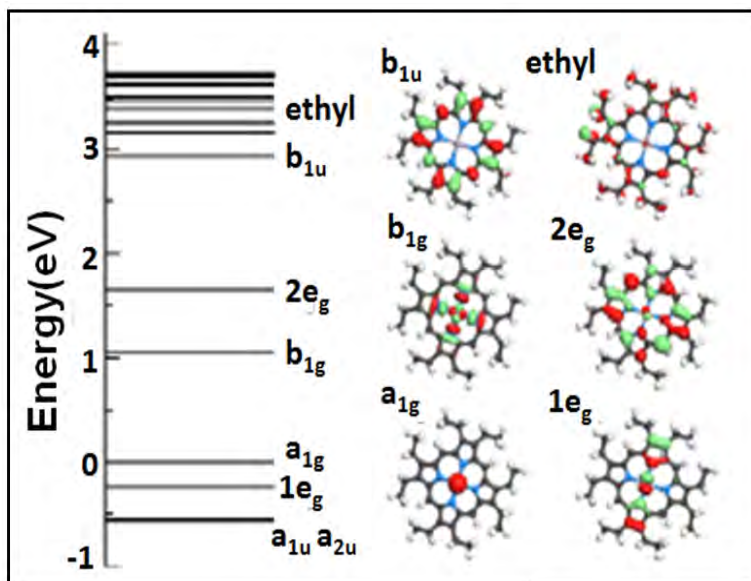
Figure 5(a)   Figure 5(b)

Figure 5(a) Comparison of calculated density of states for NiOEP with multilayer IPES spectrum,(b) Calculated density of states along with nature of molecular orbitals.

Photoemission analysis of NiOEP molecular conformer

STM studies for the deposition of metal octaethylporphyrin on metallic substrates establish that ethyl groups adopt an 'up' configuration as shown in Figure 6(a,b) in the monolayer regime.[6] However, in the gas phase, ethyl groups adopt a 'flat' configuration in the absence of substrate induced interactions. In order to investigate the impact of different conformer adopted by NiOEP XPS C1s spectra are investigated. As shown in Figure 6(a) there are different inequivalent carbon atoms in the octethylporphyrin molecule belonging to pyrrole carbons (C_1, C_2), bridge carbons (C_3) and ethyl groups carbon atoms(C_4, C_5).

Theoretical calculations suggest that energy separations between C_1 and C_3 carbon atoms is small, both in 'up' conformer as well as in 'flat' conformer. Secondly, the energy separation between ethyl groups carbon atoms C_4, C_5 and C_2 is higher in flat conformer as compared to up conformer. C1s XPS Curve fitting are performed for gas configuration as well as for the NiOEP deposition on Au(111) in monolayer regime as shown in Figure 7. The curve fitting analysis show that energy separation among different components follow almost similar trends as predicted by theoretical calculations for 'up' as well as 'flat' conformer.

73
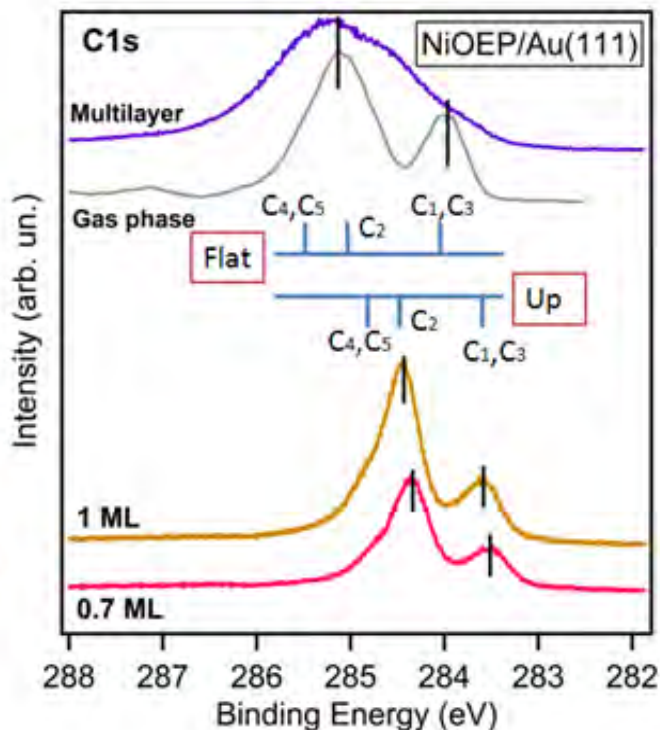
Figure.6   Figure.7

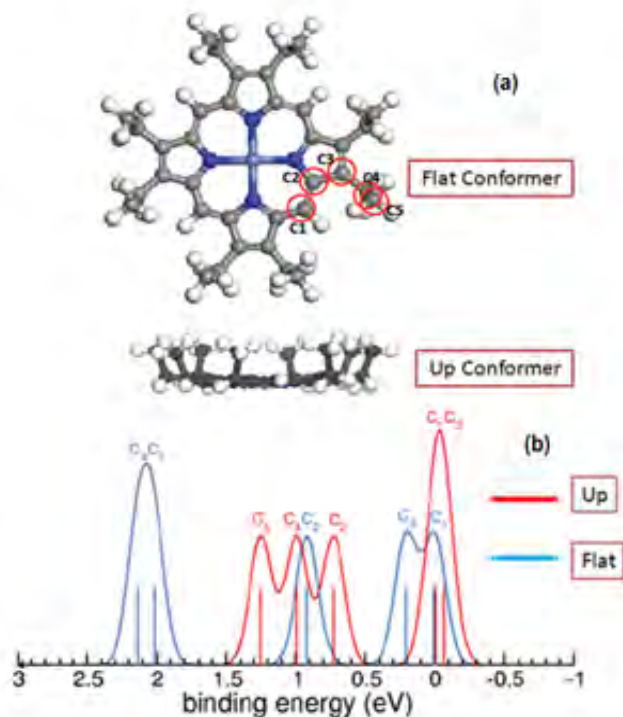Figure.6(a) Schematic representation of 'Up' and 'Flat' conformer(b) Calculated relative binding energy separation between different C 1s components Figure.7 XPS C1s spectrum for the deposition of NiOEP on Au(111) as function of coverage along with gas phase spectrum.

4.3 Octaethylporphyrin Thin Films

In order to utilize organic molecules for novel functional devices it is crucial to gain understanding of various factors influencing the physical properties of thin films in addition to interfacial electronic properties. One of the important parameter which notably influences the optoelectronic properties of the molecular thin films is the electron affinity of the molecular TF, i.e. the energy of the LUMO (See chapter 1). The information about the energy position of LUMO is significant due to its implications on the transport band gap. The energy position and nature of LUMO as well as other unfilled orbitals is notably influenced by the nature of central metal atom as it controls the hybridization with porphyrin ring MOs.[6]

We employed inverse photoemission spectroscopy to investigate the energy position of LUMO corresponding to various octaethyl porphyrin molecules investigated in the study. As we have discussed previously this technique has the ability to provide information about the unoccupied density of states therefore, provides direct access to determine the energy position of LUMO. In addition to IPES, X-ray absorption is also widely used to investigate the nature of LUMO, though the presence of the hole in the process strongly perturbs the final energy of the system. Often in the literature the energy position of LUMO is determined by knowing the energy

position of HOMO, assuming an unchanged transport gap (E_{gap}=LUMO-HOMO), or from measurements of electron affinity of similar systems. Figure 8 shows the occupied as well as unoccupied molecular orbitals for the MOEP molecules. In case of metal octaethyl porphyrin molecules 3d metal atom orbitals hybridize with porphyrin ring MOs and under D_{4h} symmetry transform into $a_{1g}(dz^2)$, $b_{1g}(dx^2\text{-}y^2)$, $e_g(d_\pi)$, $b_{2g}(d_{xy})$.

As shown in Figure 8 multilayers of OEP molecules were deposited along with H_2OEP to gain information about the energy position of LUMO and other orbitals. H_2OEP molecule is presented as a reference so that impact of insertion of transition metal atom in the macrocycle can be determined. It is evident that energy position of Molecular orbitals is notably modified by the insertion of transition metal atom. There is an apparent similarity in the energy position of unoccupied density of states for ZnOEP and CuOEP molecular thin films. In order to determine the nature of MOs involved in HOMO, LUMO and LUMO+1, we compared our IPES measurements with the DFT [13] calculations performed to determine the nature of molecular orbitals in porphyirn molecules. In case of ZnOEP and CuOEP the LUMO is $2e_g(d_\pi)$ MO while LUMO+1 has empty porphyrin b_{1u} MO character. $b_{1g}(dx^2\text{-}y^2)$ MO in case of NiOEP is strongly anti bonding and lies below $e_g(d_\pi)$, making it LUMO. DFT calculations show that ethyl groups lie between the energy range of 3 to 4eV as shown in Figure 8. Although NiOEP is diamagnetic and exhibits a closed shell configuration similar to ZnOEP however, the orbitals character as well as energy position is notably different due to dissimilar empty orbitals involved in the hybridization. b_{1g} MO lies below $2e_g$ MO in case of NiOEP and becomes LUMO. However, in case of ZnOEP HOMO has no contribution from metal 3d orbitals and has porphyrin ring a_{2u} character. Due to absence of central metal atom HOMO and LUMO has porphyrin ring MOs (a_{1u} and a_{2u}) character. The orbitals assignments are according to DFT calculations for isolated porphyrin molecules. However, it is worthwhile to mention that solid state packing of molecules can lead to shift in the energy position of frontier orbitals leading to decrease in the HOMO-LUMO gap ref Ishii (see Introduction). The cause of changes in the electronic properties of molecular thin films as compared to molecular phase can be due to geometrical distortions within the molecule and/or enhancement of electronic screening. It has been reported that many body perturbation theory calculations using GW method can better estimate the HOMO-LUMO gap in thin film phase as compared to DFT calculations.[14] Nevertheless, DFT calculations for the isolated molecule provide useful information about the assignment of MOs and their character.

An accurate determination of transport gap is crucial for the utilization of porphyrin molecules for solar cell applications. Theoretical calculations show that optical properties of porphyrin molecules are strongly dependent on the π conjugation network.[15] ZnOEP molecular thin films have been investigated due to high photo-absorption coefficient in the visible region and their applicability in photovoltaic applications. Moreover, ZnOEP is an efficient electron donor for the OPV cells and multilayer structure of ZnOEP with C_{60} has been found as a promising system for photovoltaic applications with good efficiencies.[16] Moreover, ZnOEP molecules have the

ability to arrange in well ordered structure and easy experimental availability by cost effective thermal evaporation technique.[16]
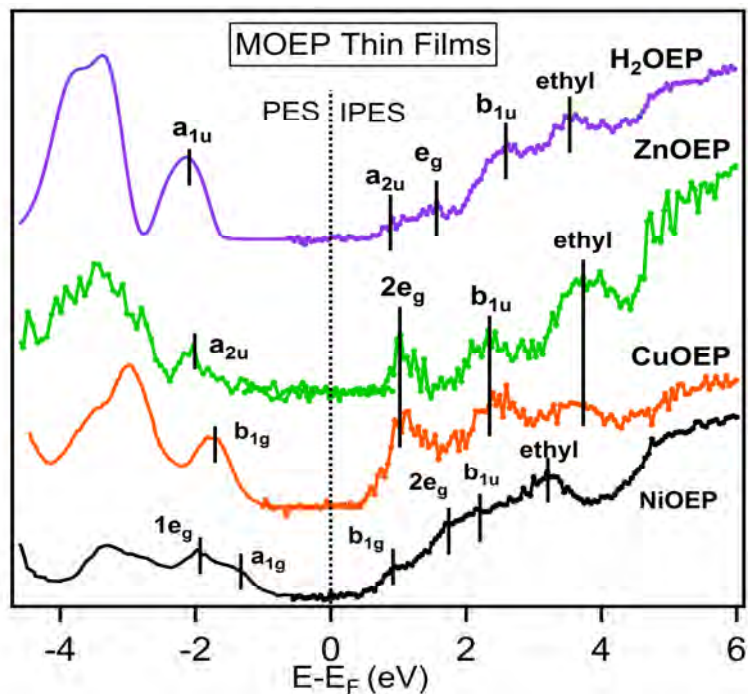
Figure 8 Combined UPS and IPES spectrum for the MOEP multilayer

As shown for NiOEP and CoPc multilayers measurements (Figure 8 this chapter and Figure 3 MPc chapter) IPES measurements revealed variations in the broadening and energy position in differently layered molecular TF, and the high sensitivity of the Empty orbitals from thickness, order, screening, polarization etc. in accordance with ref. 17. Controlled growth ZnOEP TF on technologically important substrates (quartz, ITO, Au poly etc) are planned in the next future to determined the Electron Affinity and the Transport Gap, in comparison with the optical gap and long range order.

4.4 ZnOEP thin films as model systems: Interconnection between structural and physical properties

We investigated the physical properties of ZnOEP on technologically important substrates such as SiOx/Si and ITO. The objective of this study is to establish an interconnection between structural and physical properties of ZnOEP thin films. ZnOEP molecule presents a closed shell configuration with completely filled d shell ($3d^{10}$).Therefore, strong hybridization effects with underlying substrate are not expected in case of ZnOEP similar to CuOEP on Au(111) investigated in the previous section. Here, we have investigated about 40nm thick ZnOEP molecular films on technologically important substrates such as SiOx/Si and ITO substrates in

order to explore the impact of solid state packing on physical properties and intermolecular interactions.

The spectral features are boarder as compared to solution and gas phase spectrum probably due to molecular distortions in the thin film phase. It has been observed that the elongation of the π conjugation and loss of symmetry in porphyrins cause broadening and a red shift of the absorption bands together with an increasing intensity of the Q bands (500-600nm) relative to that of the Soret band (near 400 nm).[18] Light harvesting ability and transport of porphyrin thin films are influenced by the molecular packing and long range order. It is evident that relative intensity of Q bands is higher than Soret band for semiordered crystalline ZnOEP films on the transparent substrate ITO as compared to disordered film. Further, the optical absorption spectra obtained in solution and gas phase are notably different than semiordered crystalline ZnOEP films on ITO highlighting the impact of unique molecular packing and long range order.[18,19]
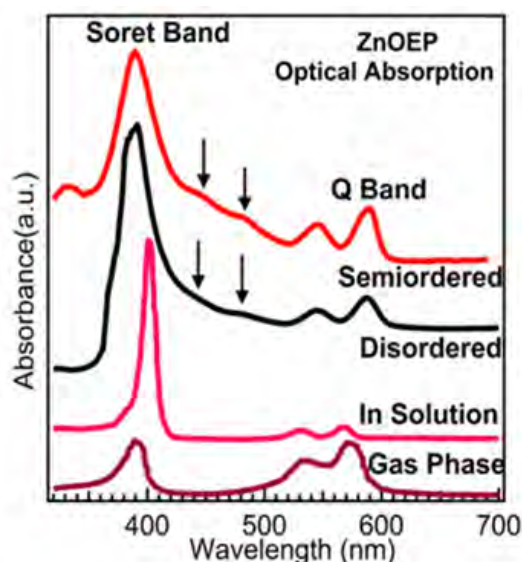
Figure 9 The optical absorption spectra of disordered and semiordered ZnOEP TF on ITO are compared with literature spectra of gas phase and solution ZnOEP dissolved in dichloromethane . Peaks labeled with arrows are related to the inter-molecular charge-transfer excitons in the films

The impact of solid state packing on physical properties is evident from the comparison of ZnOEP molecules solution phase optical absorption spectrum with ZnOEP thin films spectrum deposited on ITO (Figure 9). [19] The photoenergy conversion efficiency has been found to be related to long-range order in ZnOEP films In case of C_{60}-ZnOEP heterojunctions the hole mobility in the ZnOEP film becomes higher by crystallization increasing the number of inter-molecular charge-transfer (IMCT) excitons and enlarging the mobility of carriers. It results in significant improvement of photoabsorption band efficiency under illumination.[16]

ZnOEP molecule can adopt two conformers that differ in mutual orientations of ethyl groups. These are alternatively oriented for the isolated free molecule, labeled SM flat in Figure 10 (gas

phase and solutions). In the solid triclinic structure, labeled SM TR the ethyl-groups are in a *trans* configuration with respect to the basal plane with four ethyl groups pointing upward, while the other four pointing downward, probably to reduce steric (and repulsion) effects in solids. Generally, porphyrins present a pronounced tendency of polymorphism in crystal packing. At variance the ZnOEP is considered as a good model system, which has no structural polymorphism in the single crystal and present the triclinic structure, labelled TR in Figure 10.

ZnOEP has a relatively simple structure with eight ethyl groups linked to the pyrrole ring surrounding the M-N macrocycle, in close relation to the native porphirine, presenting two different conformers, in the free molecules (gas phase and solutions) and in the solid aggregation related to the ethyl groups orientation. Though, in general the outer groups orientation is considered a minor factor in the energy alignment of orbitals, theoretical calculations of NiOEP aggregations found that the ruffling of the ethyl groups induces perturbation on the electronic properties.
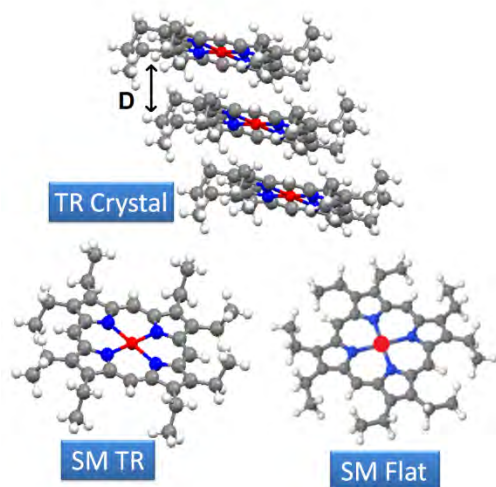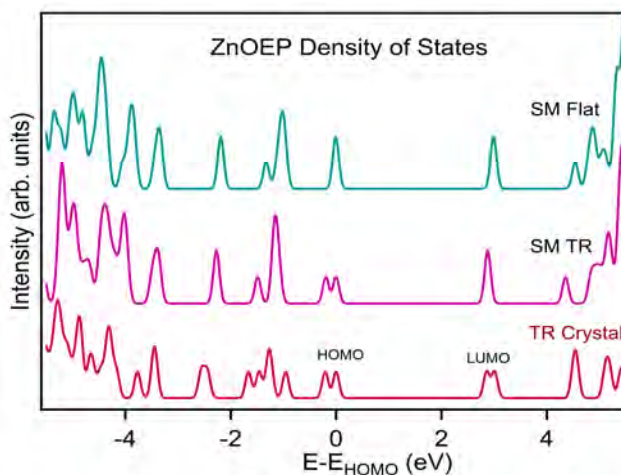
| Figure 10 | Figure 11 |

Figure.10 The ZnOEP conformers: SM Flat isolated flat molecule, SM TR ZnOEP with out of plane ethyl groups orientation within the triclinic structure, TR Crystal the same conformer in the triclinic structure. D indicates the adiacent plane distance(~ 3.4 Å). Figure11 Comparison of the DOS* of ZnOEP triclinic crystal and single molecule in isolated (flat) and Triclinic (SM TR) comformers   *courtesy Arrigo Calzolari.

DFT calculations for the density of states (DOS) shows that electronic properties of the two conformations present differences in the Molecular orbitals energies. HOMO-LUMO gap which is reduced for SM TR configuration by ~100 meV with respect to SM flat configuration. The different spatial orientation of the lateral C-H group also imparts a modification of the intrinsic molecular dipole, which is μ=0.20 D for SM flat conformer as compared to μ =0.25 D for the SM TR confomrer. Moreover the triclinic crystal present π-π intermolecular interactions due to ordered stacking of molecules in adjacent planes which are reflected in the modification of density of states. It is worthwhile to mention that DFT calculations can overestimate the HOMO-

LUMO gap and GW calculations taking into account many body perturbation effects are more suitable to estimate the HOMO-LUMO gap.[14] Nevertheless, DFT calculations do reflect alterations in density of states corresponding to SM flat and SM TR molecular conformer.

In order to highlight the impact of unique molecular packing and long range order to π conjugation network, we adopt multi-technique characterization to gain complementary information on vibrational properties and the degree of order/dimension of the crystallites in the film using Raman spectroscopy, grazing incidence X-ray diffraction (GIXRD) and atomic force microscopy (AFM). X-ray absorption fine structure (XAFS) plays an important role in elucidating the local atomic structure by using the protocol established for the molecular characterization in TF in literature. Our results indicate that the degree of order in the ZnOEP films is determined by the substrate, its treatment and by the growth procedures. We found that the increasing of long range order, leading to greater overlap of π orbitals, is also related to the symmetry reduction of ZnOEP conformers involving the outer C_α and C_β and ethyl carbon atoms.

In this study, ZnOEP thin films of about 40nm thickness were deposited on SiOx/Si and ITO at a deposition rate of ~ 2 Å/min (base pressure 2 10^{-10} mbar, pressure during deposition 5 10^{-9} mbar) from resistively heated quartz crucibles containing ZnOEP powders. The thickness was measured by oscillating quartz microbalances. The ITO substrates were rinsed in acetone before introducing them in the UHV chamber. In order to increase the ordering, the annealing of the TF was performed after deposition at temperature far below the sublimation point at 80 °C for 10 hours in UHV.The ZnOEP TFs deposited on ITO at RT are labeled as "disordered" and "semiordered" on SiOx/Si. While annealed TFs on ITO are labeled as "semiordered" and annealed TF on SiOx/Si are labeled as "ordered".

4.4.1 Structural and morphological Characterization ZnOEP thin films

Figure 12 shows the bidimensional diffraction patterns for the different classes of ZnOEP films, which clearly reflect differences in the long range order. Several diffraction spots are clearly detectable for the annealed ZnOEP TF on SiOx/Si demonstrating a highly crystalline and ordered structure. The diffraction spots are comparatively wider and relatively less intense at higher diffraction angles for the ZnOEP TF deposited at RT on SiOx/Si, therefore termed "semiordered". Annealing was also effective in obtaining a better ordering in TFs deposited on ITO. The rings in the bottom panels c) and d) are related to randomly oriented polycrystalltes in the ITO substrate while Si bulk reflections are also visible in the upper panels.
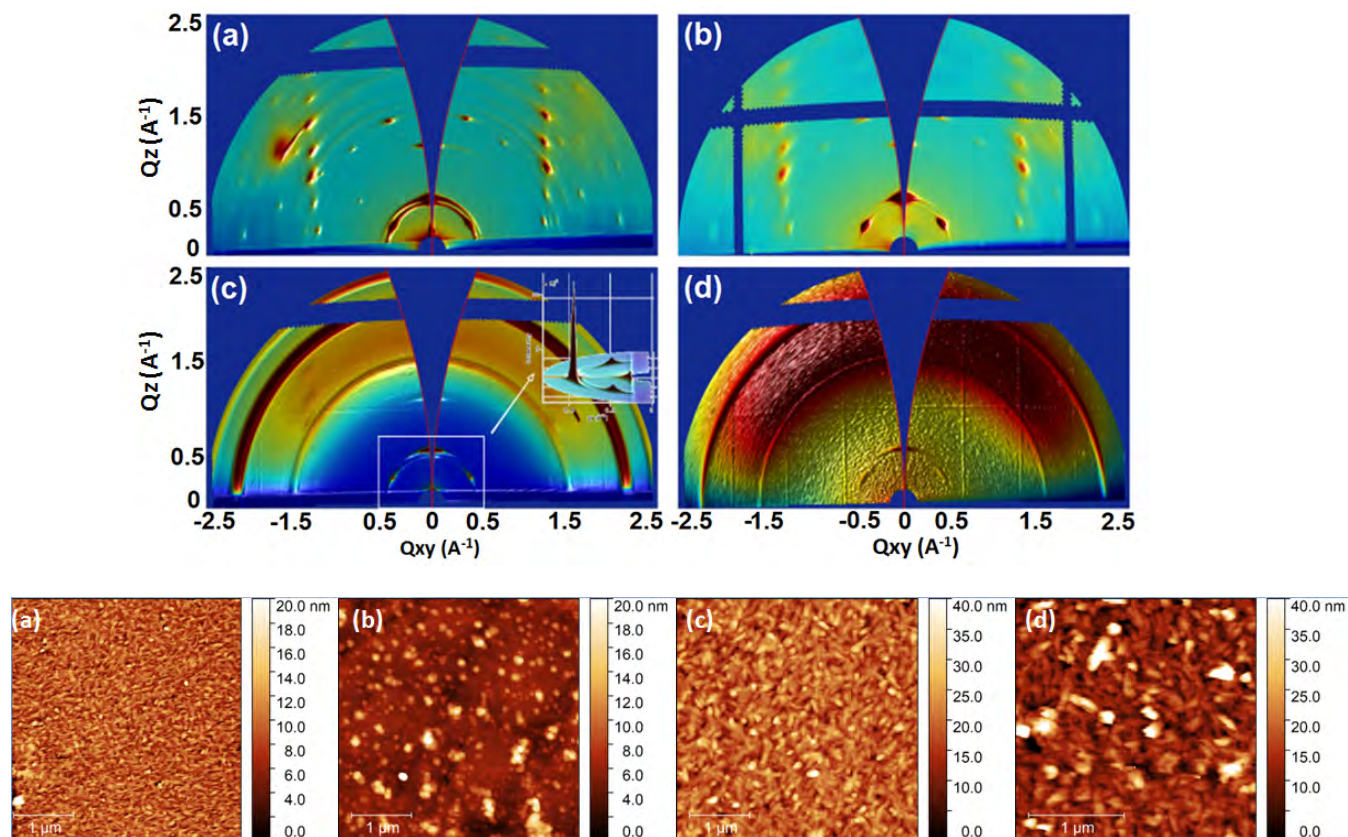
Figure 12 Top Panel : Bidimensional diffraction patterns on the ZnOEP films a) ordered sample on SiOx/Si, b) semiordered on SiOx/Si c) semiordered annealed sample on ITO and d) disordered sample on ITO. The indexing has been assigned through the powder simulated XRD pattern (Mercury code) from reported data[20]. Bottom Panel: AFM images of ZnOEP films deposited on (a) ordered (b) semiordered/Si (c) semiordered/ITO and (d) disordered film.

GIXRD analysis shows that ZnOEP TFs adopt a triclinic structure with a =4.692 Å, b =13.185 Å, c =13.287 Å, α=113.94, β=91.177 and γ=92.16. The patterns are compatible with the reported triclinic structure [20-22] of the ZnOEP single crystal. [20] In all the cases, including the disordered sample, the first order (higher intensity) reflections are detectable and exhibits good resemblance to the results obtained by laboratory sources.[23] The dominant orientation of crystallites for ordered, semiordered and disordered ZnOEP thin films is such that the [0 -1 1] direction is perpendicular to the substrate surface. No polymorphs were detected, while a certain degree of random misorientation of the crystallites was present, especially in annealed TF on Si, giving rise to a faint powder-like component of the patterns. The cell parameters were checked against reference data [20] by means of the Mercury [24] and SimDiffraction[25] codes. Peak positions were extracted by means of Fit2d in association with WinPlotr.[26] The results for the average crystallite size are summarized in Table 1 for comparison with AFM observations.

The average crystallite size is lower for the semiordered film on the SiOx/Si substrate compared to ITO; this can be attributed to the different growth mechanism induced by different surface roughness and molecule-substrate interactions. AFM images were analyzed using average

crystallite size and root mean square (rms) parameters as listed in Table 1 and reveal smaller grain size and lower surface roughness for the ordered film testifying higher order of ZnOEP crystallites on SiOx/Si surface as shown in Figure 12.

Sample	GIXRD Average crystallite volume weighted Size nm	AFM Average grain size nm	AFM RMS (Roughness) nm
Ordered	24.0 nm	20.2	2.25
Semiordered/Si	25.8 nm	39.3	2.52
Semiordered/ITO	28.5 nm	39.4	4.42
Disordered/ITO	No data	45.5	7.39

Table-1 Comparison of average grain size as obtained from GIXRD and AFM analyes along with surface roughness

The evaluated crystallite size of the ordered ZnOEP TF is 20.2 nm while for the semiordered (both for ITO and SiOx substrates) it is about 39.4 nm. While the grain sizes measured by AFM and GIXRD have a similar dependence on the TF preparation, the values determined by AFM are in most cases greater. This is because AFM provides information about agglomerated crystallites, i .e. domains of crystallites.[28] Instead, crystallite sizes determined by GIXRD are related to the coherent scattering domains having perfect molecular order in the specified crystallographic direction. Thus, both GIXRD and AFM show that the crystallite size of ZnOEP TFs is lowest for of ordered films.

4.4.2 Consequences of long range molecular order on vibrational properties: Raman spectroscopy analysis

Raman spectroscopy characterization (Figure 13) provides the vibrational properties of the ZnOEP TF. Ab-initio calculations have been performed to simulate Raman spectra after the structural optimization of ZnOEP molecule at B3LYP-D* level. ZnOEP structural optimization confirms the *trans* configuration (Fig. 10). The detailed assignment of the peaks along with calculated Raman bands can be seen in table 2.[30,31] As shown in Figure13 (a), absence of Raman shift for the vibrational modes involving central metal atom bound to 4 N atoms in the macrocycle suggests that in spite of dissimilar molecular stacking, no significant structural changes occur in the macrocycle.

Moreover, intermolecular interactions in the closely packed ordered films (triclinic structure) do not lead to macrocycle deformation. However, for skeletal carbon atoms (C_β, C_m, C_α) vibrational modes, we observe small but notable Raman shift indicating a probable structural deformations related to (C_β, C_m, C_α). Such Raman shifts related to vibrational bands at 1561 cm^{-1}($C_\beta C_\beta$), 1621 cm^{-1}($C_\alpha C_m$) and 1376 cm^{-1}($C_\alpha N$) due to π-π interactions have been observed for CuOEP [32] and

zinc(II) and palladium(II) octakis(βdecoxyethyl) porphyrins.[33] Notably, there is a significant decrease in the intensity of vibrational modes related to C-N-Zn ($357cm^{-1}$) and Zn-N_4 ($254cm^{-1}$) and 1561 cm^{-1} ($C_\beta C_\beta$), 1621 cm^{-1} ($C_\alpha C_m$) and 1376 cm^{-1} ($C_\alpha N$) for disordered film as compared to ordered film.

Due to dissimilar molecular stacking and higher disorder of ZnOEP molecules, the intensity of Raman bands is least for disordered TFs deposited at RT on ITO. Such a sensitive dependence of macrocycle vibrational band intensities for the disordered film has been reported for Titanyl Phthalocyanine[34] TF grown on amorphous quartz plates at different temperature. Disordered molecular stacking of iron and cobalt phthalocyanine (FePc and CoPc) TFs deposited on ITO has been revealed by the dependence of macrocycle vibrational band intensity on molecular order. In the low frequency range simulated Raman spectrum shows good agreement with the observed ordered film spectrum as shown in the Figure 13a.

Two distinguishable peaks at 225 cm^{-1} (calculated $234cm^{-1}$) and 245 cm^{-1} (calculated $249cm^{-1}$) are related ethyl groups vibrational modes. In addition, modes at $1320cm^{-1}$ and $1492cm^{-1}$ are also related to peripheral ethyl group vibrations. Calculations reveal that the anti-phase bending motions of the CH_3 and CH_2 moieties give rise to the set of peaks concentrated around 1500 cm^{-1} that has been experimentally observed as a single peak at 1492 cm^{-1} only in case of the ordered film deposited in SiOx/Si. As shown in Fig. 13 (a) and (b) vibrational modes corresponding to external ethyl groups are much broader and exhibit lower intensity for disordered film as compared to ordered ZnOEP film further highlighting the influence of molecular order on vibrational properties of the film.

Moreover, Bader analysis of charge density reveals the formation of weak ionic-like inter-molecular interactions between protons belonging to the CH_3 moieties in different lattice planes. Such interactions are not anticipated for disordered film with randomly oriented ZnOEP molecules, justifying that intermolecular interactions are prevalent for ordered ZnOEP film which can have significant implications on the charge transport properties of ZnOEP films.

Thus, differences in molecular packing lead to significant changes in intermolecular interactions, which are revealed by the Raman spectra. In order to establish structural deformations related to the (C_β, C_m, C_α) for the as deposited ZnOEP TFs a detailed structural analysis is needed to shed more light on this issue. We address this issue in the next section devoted to comprehensive X-ray absorption analysis.
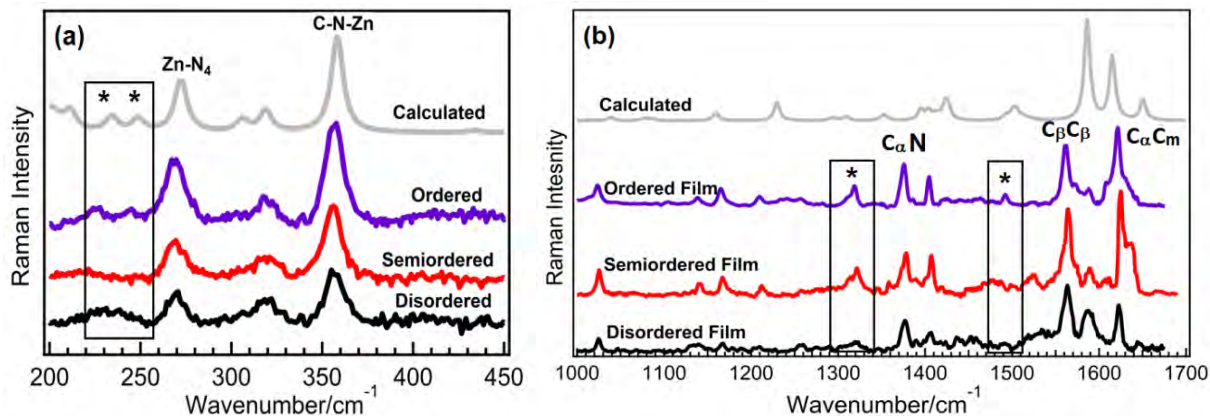
Figure.13(a)   Figure.13(b)

Figure 13 The Raman spectra of ZnOEP films acquired at 532 nm excitation wavelength in the ranges(a) 200-450 cm^{-1}and (b) 1000 -1700 cm^{-1} compared totheoretical calculations of the frozen ZnOEP molecule. Peaks labeled as * are related to peripheral ethyl group vibrational modes.

Assignment	Experimental frequency cm^{-1} (ordered film	Calculated frequency cm^{-1} (Frozen Molecule)
(C_1C_2)	1023	1038
$(C_\alpha C_\beta)$	1139	1174
(C_mH)	1210	1229
CH_2twist	1257(weak)	1285
$(C_\beta C_1H)$	1320	1368
$(C_\alpha N)$	1376	1360
$(C_\alpha N)$	1404	1392
(C_1H-C_2H)	1492	1492-1511
$(C_\beta C_\beta)$	1561	1587
$(C_\beta C_\beta)$	1588	1615
$(C_\alpha C_m)$	1621	1650

Table -2 Peak assignments are according to references 30, 31.

4.4.3 Molecular orientation and intermolecular interactions: X-ray absorption results

Based on GIXRD and AFM results it is evident that molecular stacking, grain size and order are notably different in ZnOEP TFs. In order to further corroborate the molecular orientation of

ZnOEP molecules with respect to underlying substrate and implications of ordered π-π stacking on intermolecular interactions detailed X-ray absorption analysis on ZnOEP thin films has been performed. An asymmetrical stretching of skeletal carbon atoms of the porphyrin conformer has been observed and attributed to the ordered molecular stacking and intermolecular interactions. A detailed MXAN fitting analysis[36] of X-ray absorption near edge structure (XANES) establishes a symmetry reduction in the molecular conformer involving skeletal carbon atoms of the porphyrin ring for the ordered films highlighting the consequences of increased π stacking of ZnOEP molecules adopting triclinic structure.

The Figure 14(a) depicts the Zn K edge spectrum normalized at 9720 eV for the ordered, semiordered and disordered samples taken at the magic angle 55°.In case of disordered film the line shape of peak D appears distinct while peak L around 9660 eV shows notable decrease in intensity. N K edges (Figure14b) were taken on the same ex-situ grown samples. No valuable differences were found in the XAS of in-situ grown samples. A slight shift in the Lowest Unoccupied Molecular Orbital (LUMO) position and a general broadening is detected for disordered films as compared to semiordered and ordered films for N K edge spectra. The feature D above the N K edge appears distinct for the disordered sample. The spectral line shape is in agreement with the data reported in the literature [35] with the feature labeled L corresponding to the transition to the (LUMO).
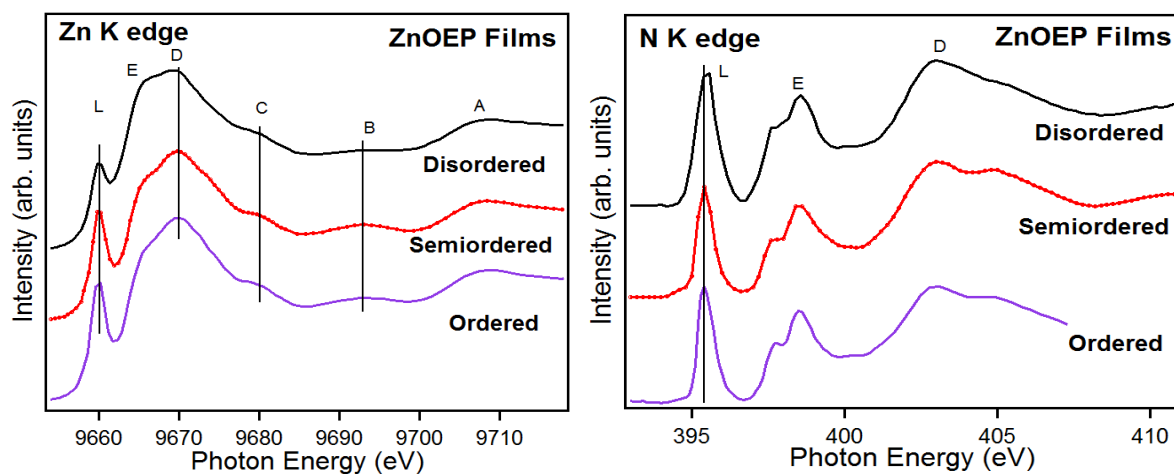
Figure 14 (a)   Figure 14(b)
Figure 14(a) Normalized Zn K edge (b) N K edge XANES spectra of bulk and TF ZnOEP samples.

The average molecular orientation in molecular layers can be extracted by analyzing the LUMO dichroism of Zn K edge and N K edge NEXAFS collected at several incident angles for ordered and semiordered samples. The normalized Zn K edge and N K edge NEXAFS spectra of the ZnOEP TFs taken at different angles are reported in Figure15.
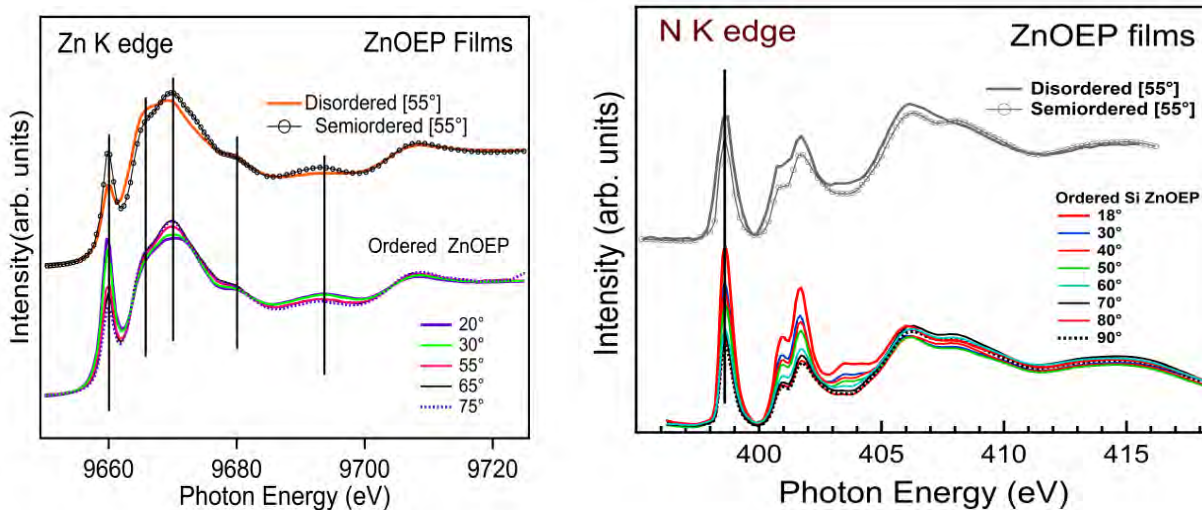
Figure 15 Normalized Zn K edge and N K edge XANES spectra of ZnOEP TF

Dichroic ratio R has been calculated to determine the average tilt molecular angle in TFs. Our quantitative analysis, taking into account the different light polarization in case of Hard X-rays Zn data (GILDA-LISA P ≈95%) and soft X-rays N spectra (BACH P=100%), found agreement from the two edges. For ordered ZnOEP TF, we observe a negative R factor of -0.33 to -0.36. If these films were completely crystalline, with a single crystal orientation, this tilt could be interpreted as a macrocycle plane tilt of ≈ 44° with respect to substrate. For semiordered samples analogous analysis provides an average angle of about 50° as shown in Figure 16.[33]

This value of average tilt angle for the semi ordered sample is in good agreement with the results discussed in ref 33. Therefore, annealing of the semiordered sample leads to a change of macrocycle plane tilt from 50° to 45° with respect to substrate. N K edges for the three differently ordered films are almost similar, suggesting that macrocycle structural variations are feeble. The result is complementary to the Raman spectroscopy observation where no significant Raman shift has been observed for macrocycle vibrational modes.

In order to gain insight into the impact of long-range order in the ZnOEP TFs on intermolecular structural alterations, curve fitting of Zn K edge spectrum was performed considering multiple scattering as shown in Figure 17 Though, XANES provides the averaged data within the films, the fits provide useful indications on the structural changes related to the differences in the XANES line shapes among the samples.
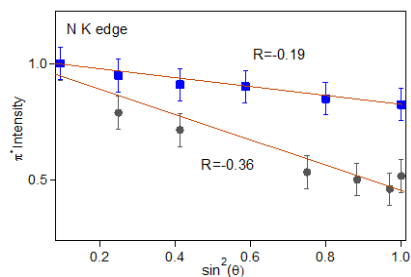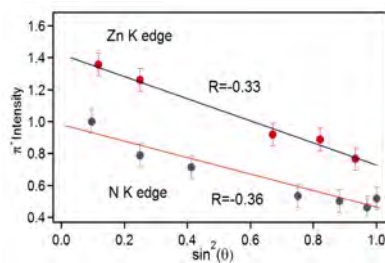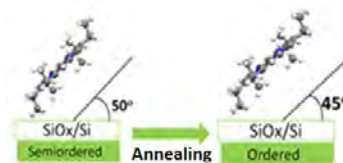
Figure 16(a)   Figure 16(b)   Figure 16(c)

Figure. 16 (a) Comparison of the LUMO intensity versus grazing angle for N K edges in the ordered (black point) and semiordered (blue squares) ZnOEP film. (b) Analysis of the LUMO intensity versus angle of incidence for both edges in case of ordered film(c) Schematic representation of ZnOEP molecular orientation for semiordered and ordered films based on XANES analysis.

The magic angle spectra of the films have been fitted adopting the structural coordinates as fitting parameters. Two different coordinate models have been used: the single molecule (SM TR) of Figure. 10 b, and the TR structural model consisting in the addition of the nearest C and N atoms (Figure.10 c) of the top and bottom ZnOEP molecules within the triclinic structure. Namely the coordinates of the C_β, C_1 and C_2 atoms are taken as variables of the fit procedure. Both SM TR and TR model fits indicate that the C_1 and C_2 ethyl groups present a broaden distribution of distances in a sort of confusion ring (Table 3) confirming the Raman observation related to peripheral ethyl groups vibrations.

Figure17 (a)   Figure 17(b)

Figure 17 Comparison of the Zn K edge experimental spectra (dots) and the MXAN simulations for the ordered (a) and disordered films (b) taken at magic angle at about 55°

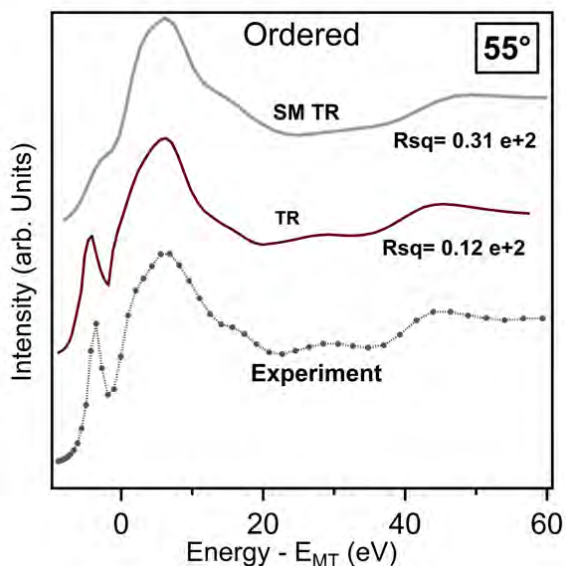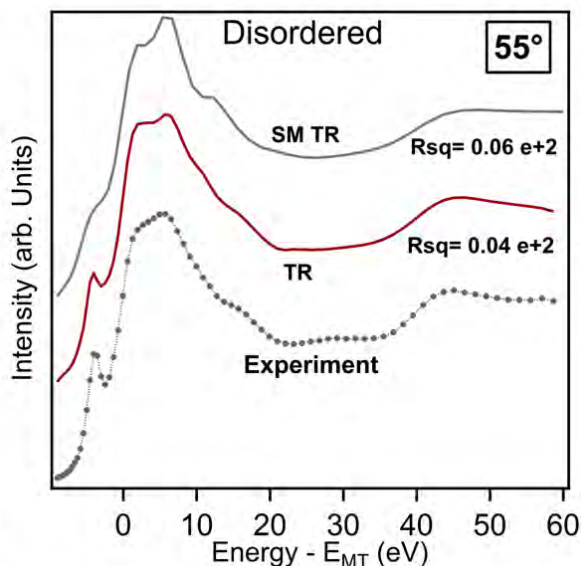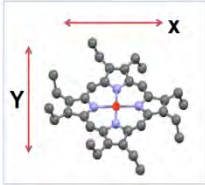|	Disordered	Disordered	Ordered	Ordered
Model	**SM TR**	**TR**	**SM TR**	**TR**
Best Fit Rsq Parameter	0.06 e 2	0.04 e 2	0.31 e 2	0.12 e2
Zn-C$_\beta$ /Å	4.29 along X 4.31 along Y	**4.29 along X** **4.30 along Y**	4.29 along X 4.33 along Y	**4.24 along X** **4. 36 along Y**
Zn-C1 /Å	Confusion 5.93 along X 5.53 along Y	Confusion 5.87 along X 5.55 along Y	5.95 along X 5.32 along Y	5.84 along X 5.50 along Y
Zn-C2/ Å	Confusion 6.58 along X 6.20 along Y	Confusion 6.57 along X 6.12 along Y	6.47 along X 6.00 along Y	6.42 along X 6.03 along Y

Table.3 List of the ZnOEP distances in Å, as found by the structural MXAN fit by using the different models described in the text (see Fig.1). The X and Y directions are described in the inset. Confusion indicates a substantial insensitivity of the simulation to the ethyl C_1 and C_2 coordinates.

Good quality simulations for the ordered ZnOEP TFs are obtained for angle 55°, indicating that the outer C atoms (C_α, C_β) present a deformed symmetry. The observation establishes a symmetry reduction of skeletal carbon atoms due to higher molecular order and increased π stacking of ZnOEP molecules adopting triclinic structure. As shown in table-3 outer C atoms (C_α, C_β) do not present a deformed symmetry for disordered films in contrast of ordered ZnOEP TFs. The observation highlights the implications of molecular order on electronic properties of ZnOEP TFs. The TR fits result improved with respect to the SM. The average of C_β distances remain practically unchanged, though a weak reduction of the square symmetry (C_{4v}) of the C_β, shell is found, with longer distances along the X direction (see inlet in Table 3) in the plane of macrocycle.

4.4.4 Consequences of long range molecular order on electronic properties: Photoemission analysis

Photoemission measurements have been conducted on ordered, semiordered and disordered samples with photon energy of 600 eV. The spectroscopic features of the ordered samples result well pronounced with respect to the semiordered films and even more with respect to the disordered film. The C1s presents a more complex structure due to the different species of C atoms in the molecule, as labeled in Figure. 18. The table below lists the experimental binding energies and the FWHM of the Gaussian contributions of the carbon atoms components obtained by the core level fit performed by standard procedures. A broadening has been evaluated for the semiordered sample which further increases in the disordered films. The possible cause of such broadening in the C1s can be due to inhomogenities caused by the disordered molecular stacking which influence vibrational and screening effects. [37] Such inhomogeneities can induce a variation of the charge density which may lead to changes in the local molecular environment of the emitting atoms inducing, a probability distribution of the molecular emission peaks and an experimental broadening of the spectra.

Films	E_{Cm}(eV) FWFM	E_α(eV) FWFM	E_β(eV) FWFM	$E_{C1,2}$(eV) FWFM
ZnOEP Disordered	284.5 1.2	285.9 1.1	285.0 0.8	287.1 2.3
ZnOEP Semiordered	284.2 0.7	285.5 0.9	284.75 0.7	286.3 0.7
ZnOEP Ordered	284.6 0.5	285.7 0.45	285.0 0.5	286.4 0.5
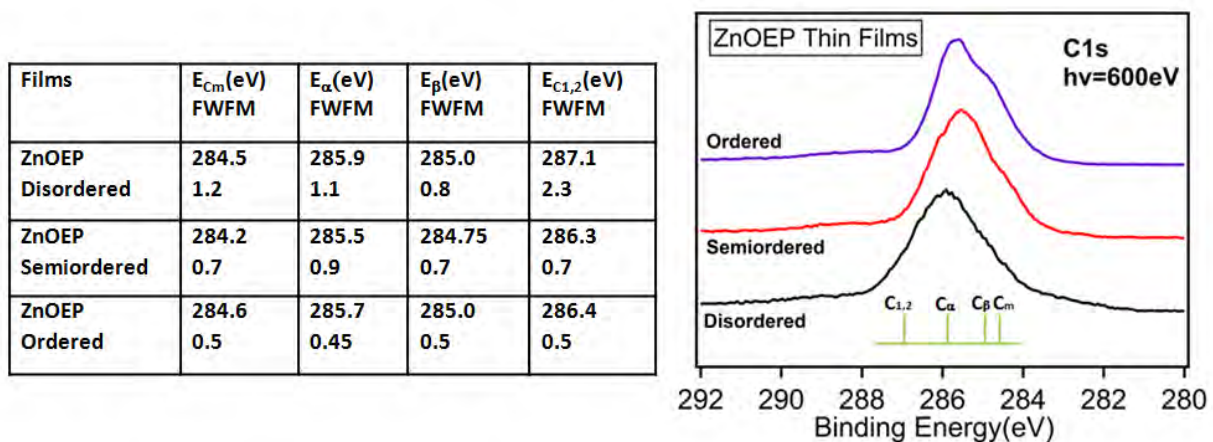
Figure 18 XPS C1s of ordered, semiordered and disordered ZnOEP TF along with table showing fitting components details

4.4.5 Discussion

It is evident from Figure 19(a) that an ordered stacking of molecules favours substantial π-π interactions. The calculated charge density contours depict the influence of π electron cloud on the neighbouring molecules in the triclinic ZnOEP framework as shown in Figure 19(b). Small Raman shifts observed in the higher frequency range corresponding to skeletal carbon atoms (C_β, C_m, C_α) for the ordered films as compared to disordered film can be attributed to alterations of π charge density. We note that it has been reported that molecular stacking induced alterations in the π charge density can lead to minor Raman shifts for the prophyrin thin films.[28]
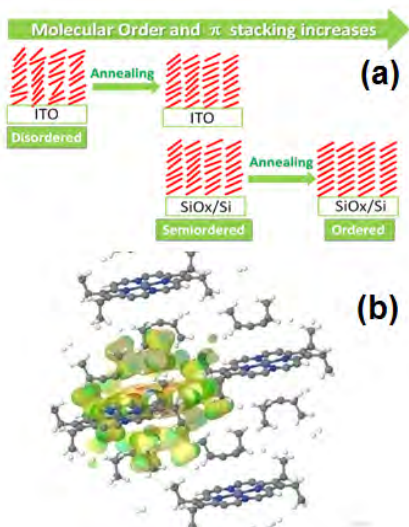
Figure 19 (a) Schematic representation of the enhanced molecular order of ZnOEP molecules depending on substrate and annealing (b)Charge contours as calculated in the triclinic ZnOEP structure between neighbour molecules

88

N K edge XANES spectra for the three differently ordered films are very similar, suggesting that macrocycle structural variations are very small. The result is complementary to the Raman spectroscopy observation in which no significant Raman shift has been observed for macrocycle vibrational modes.

The structural MXAN fits of the Zn K edge spectra reveal that spectral features for the disordered film can be reproduced considering 25 atoms instead of 31 atoms for ordered film, as indicated by the shell by shell analyses .It suggests that due to random molecular stacking in case of disordered films structural orientation of ethyl groups (C_1, C_2) with respect to C_β becomes less pronounced. As shown in Figure 13a two peaks at $225cm^{-1}$ and $245cm^{-1}$ related to ethyl group vibrational modes are absent for disordered films, revealing the impact of ethyl groups (C_1,C_2)random orientations due to molecular disorder. The observation highlights the influence of molecular order on electronic and vibrational properties of the molecular films.

 Using XRD, Melamed et al. reported that 40 nm thick ZnOEP TFs on SiOx/Si have orientation along [0 -1 1] direction perpendicular to the substrate, with ZnOEP molecules inclined by 50° with respect to the substrate. [33] These observations are in good agreement with ours, and agree with the observation that the XRD patterns of semiordered ZnOEP films on SiOx/Si substrate are similar to those deposited on ITO/glass. At variance with the semiordered film, we obtained an angle of about 45° for the ordered film with respect to substrate. It appears that annealing of the ZnOEP TF deposited on SiOx/Si at 80^oC improves the ordering along with small but notable change in angle of orientation, as shown in Figure16.

In addition, our detailed MXAN fitting analysis of XANES spectra establishes a symmetry reduction in the molecular conformer involving C_β and C_α carbon atoms highlighting the consequences of increased π stacking of ZnOEP molecules adopting triclinic structure. Such a strain in the structure is not observed in the macrocycle as shown in Table 3. These observations complement Raman analysis in which no Raman shift has been observed for the vibrational modes involving the macrocycle while small but detectable Raman shifts has been observed for the vibrational modes of skeletal carbon atoms for the ordered film as compared to semiordered and disordered film.

The probable cause of such asymmetrical stretching of skeletal carbon atoms can be related to intermolecular interactions due to proximity with neighboring molecules in the triclinic framework. Such alterations of the π conjugation network are not expected for disordered film grown on ITO at room temperature. Thus, we anticipate higher cell efficiency for the ordered ZnOEP thin films on SiOx/Si obtained by annealing films grown at room temperature.

References

[1] B. Chilukuri, U. Mazur, K. W. Hipps, Phys. Chem. Chem. Phys. 16, 2014, 14096–14107.

[2] L. G. Teugels, L. G. Avila-Bront, S. J. Sibener, J. Phys. Chem. C 115, 2011, 2826–2834.

[3] S. Ditze, M. Röckert, F. Buchner, E. Zillner, M. Stark, H. P. Steinrück, H. Marbach, Nanotechnology 24, 2013, 115305.

[4] D. van Voerden, M. Lange, J. Schaffert, M. C. Cottin, M. Schmuck, R. Robles, H. Wende, C. A. Bobisch, R. Möller, Chem. Phys. Chem. 14, 2013, 3472–3475.

[5] L. Scudiero, D. E. Barlow, K. W. Hipps, J. Phys. Chem. B 106, 2002, 996–1003.

[6] M. Fanetti, A. Calzolari, P. Vilmercati, C. Castellarin-Cudia, P. Borghetti, G. DiSanto, L. Floreano, A. Verdini, A. Cossaro, I. Vobornik, E. Annese, F. Bondino, S. Fabris, A. Goldoni, J. Phys. Chem. C 115, 2011, 11560–11568.

[7] Y. Bai, F. Buchner, I. Kellner, M. Schmid, F. Vollnhals, H. P. Steinrück, H. Marbach, J. M. Gottfried, New J. Phys. 11, 2009, 125004.

[8] L. Scudiero, K. W. Hipps, J. Phys. Chem. C 111, 2007, 17516–17520.

[9] A. Alkauskas, L. Ramoino, S. Schintke, M. von Arx, A. Baratoff, H. J. Güntherodt, T. A. Jung, J. Phys. Chem. B 109, 2005, 23558–23563.

[10] A. Resta, R. Felici, M. Kumar, M. Pedio, Journal of Non-Crystalline Solids 356, 2010, 1951–1954.

[11] M. Toader, M. Knupfer, D. R. T. Zahn, M. Hietschold, Surf. Sci. 605, 2011, 1510–1515.

[12] D. P. Woodruff, W. A. Royer, N. V. Smith, Physical Review B 34, 1986, 764.

[13] P. L. Cook, W. Yang, X. Liu, J. M. García-Lastra, A. Rubio, F. J. Himpsel, J. Chem. Phys. 134, 2011, 204707.

[14] M. Marsili, P. Umari, G. Di Santo, M. Caputo, M. Panighel, A. Goldoni, M. Kumar, M. Pedio, Phys. Chem. Chem. Phys. 16, 2014, 27104–27111

[15] A. D. Phan, Physical review E 90, 2014, 062707.

[16] S. Ryuzaki, T. Kai, Y. Toda, S. Adachi, J. Onoe, J. Phys. D. Appl. Phys. 44, 2011, 145103.

[17] Y. Kashimoto, K. Yonezawa, M. Meissner, M. Gruenewald, T. Ueba, S. Kera, R. Forker, T. Fritz, H. Yoshida, J. Phys. Chem. C 122, 2018, 12090−12097.

[18] L. Edwards, D. H. Dolphin, M. Gouterman, J. of Molecular Spectroscopy 36, 1970, 90-109.

[19] J. H. Perng, D. F. Bocian, J. Phys. Chem. 96 (12), 1992, 4804-4811.

[20] A. Ozarowski, L. Hon Man, A. L. Balch, J. Am. Chem. Society 125, 2003, 12606-12614.

[21] S. Ryuzaki, J. Onoe, J. Appl. Phys. 103, 2008, 033516.

[22] S. Ryuzaki, T. Kai, Y. Toda, S. Adachi, J. Onoe, J. Phys. D. Appl. Phys. 44, 2011, 145103.

[23] S. Ryuzaki, T. Hasegawa, J. Onoe, J. Appl. Phys. 105, 2009, 113529.

[24] www.ccdc.cam.ac.uk

[25] D. W. Breiby, O. Bunk, J. W. Andreasen, H. T. Lemke, M. M. Nielsen, J. Appl. Cryst. 41, 2008, 262-271.

[26] T. Roisnel, J. R. Carvajal, Mater. Sci. Forum 118, 2001, 378.

[27] A. M. Hindeleh, R. Hosemann, J. Mater. Sci. 26, 1991, 5127–5133; R. Hosemann, A.M. Hindeleh, J. Macromol. Sci. Phys. B 34, 1995, 327–336.

[28] J. R. Ares, A. Pascual, I. J. Ferrer, C. Sánchez, Thin Solid Films 480, 2005, 477.

[29] A. Kumar, D. Naumenko, L. Cozzarini, L. Barba, A. Cassetta, M. Pedio, J. Raman Spectroscopy, 2018, 1-8.

[30] J. H. Perng, D. F. Bocian, J. Phys. Chem. 96 (12), 1992, 4804-4811.

[31] M. Abe, T. Kitagawa, Y. Kyogoku, J. Chem. Phys. 69, 1978, 4526.

[32] L. D. Sparks, W. R. Scheidt, J. A. Shelnutt, J. Am. Chem. Soc. 110, 1988, 12.

[33] D. Melamed, B. Darlington, D. J. R. Brook, H. L. Pan, A. Campion, M. A. Fox, J. Phys. Chem. 98, 1994, 8971-8976.

[34] N. Coppede, T. Toccoli, A. Pallaoro, F. Siviero, K. Walzer, M. Castriota, E. Cazzanelli, S. Iannotta, J. Phys. Chem. A 111, 2007, 12550-12558.

[35] C. S. Guo, L. Sun, K. Hermann, C. F. Hermanns, M. Bernien, W. Kuch, J. Chem. Phys. 137, 2012, 194703.

[36] G. Rossi, F. d'Acapito, L. Amidani, F. Boscherini, M. Pedio, Phys. Chem. Chem. Phys. 18, 2016, 23686-23694.

[37] R. Cimino, A. Giarante, K. Horn, M. Pedio, Europhys. Lett. 32 (7), 1995, 601-606.

[38] Susumu Kitigawa, et al., Inorg. Chem. 18, 1979, 5.

[39] M.-S. Liao, S. Scheiner, J. Chem. Phys. 114, 2001, 9780;

[40] N. Marom, L. Kronik, Appl. Phys. A Mater. Sci. Process. 95, 2009, 165.

91

Chapter-5

Interfacial Electronic properties of Iron Complexes on Graphene

5.1 Introduction

Metal complexes adsorption on surfaces with and without graphene buffer layers is a crucial issue for their interconnection between electronic and magnetic properties and a fine characterization of these interfaces is mandatory in their applications. Research on graphene (Gr) has experienced explosive growth in the last few years. [1] When associated to magnetic nanostructures the hybrid systems are expected to lead to the possibility of engineering the magnetic functionalities. Recent results of phthalocyanines deposited on ferromagnetic metallic surfaces and Gr buffer layers have revealed a substrate-molecular coupling mechanism, showing a delicate interplay between long-range interactions and local chemical bonding, magnetic moment. [2]

In this chapter, a combination of NEXAFS and Photoemission results are presented and employed to study the adsorption of Fe-complexes molecules, (ferrocene $Fe(C_5H_5)_2$ and Fe(III)tetraphenylporphyrin chloride, FeTPP-Cl) deposited on well characterized Gr supported by metal substrates and compared with their adsorption on HOPG substrate. The two molecules have been chosen for their different structural surrounding of the Fe ion and the different distance between Fe in the adsorbed molecules and the substrate. Inverse photoemission characterization is in progress in our group to get a complete description of these interesting systems.

5.1.1 Electronic properties of Tetraphenyl porphyrin

Tetraphenylporphyrins are an important class of tetrapyrrole complexes which exhibits high potential to be utilized as building blocks in modern electronic and spintronics devices. [2] Single molecule DFT calculations show also in this case the effect of the central metal atom 3d occupancy on occupied and unoccupied density of states as shown in Figure 1. The purpose of the IPES measurements shown here is to highlight the differences in the unoccupied density of states near Fermi level induced by the partially filled 3d orbitals (FeTPP-Cl, d^6 system) as compared to fully filled 3d orbital (ZnTPP, d^{10} system).

As discussed in previous chapters the degeneracy of metal 3d orbitals is removed due to D_{4h} ligand field symmetry. However, theoretical calculations for MTPP orbital energy level alignment show qualitatively that the sequence of energy levels are modified.[3] As shown in Figure 1, the degenerate d_π orbitals lie above the d_{z2} orbital and represents semi occupied HOMO. It is evident that unoccupied d–orbitals have also out of plane character in case of FeTPP. We have performed IPES measurements of thin molecular films grown by vapor deposition in UHV in order to investigate the unoccupied density of states as shown in Figure 2.

DFT calculations for the ZnTPP thin films show that the peak at around 4eV above the Fermi level is related to peripheral phenyl groups while peak at about 1.7eV is associated with unoccupied states of the porphyrin ring. [4]

Similar to ZnTPP spectrum, FeTPP-Cl and H_2TPP spectrum also have peak around 4eV and we tentatively assign these peaks to be related to peripheral phenyl groups unoccupied states.
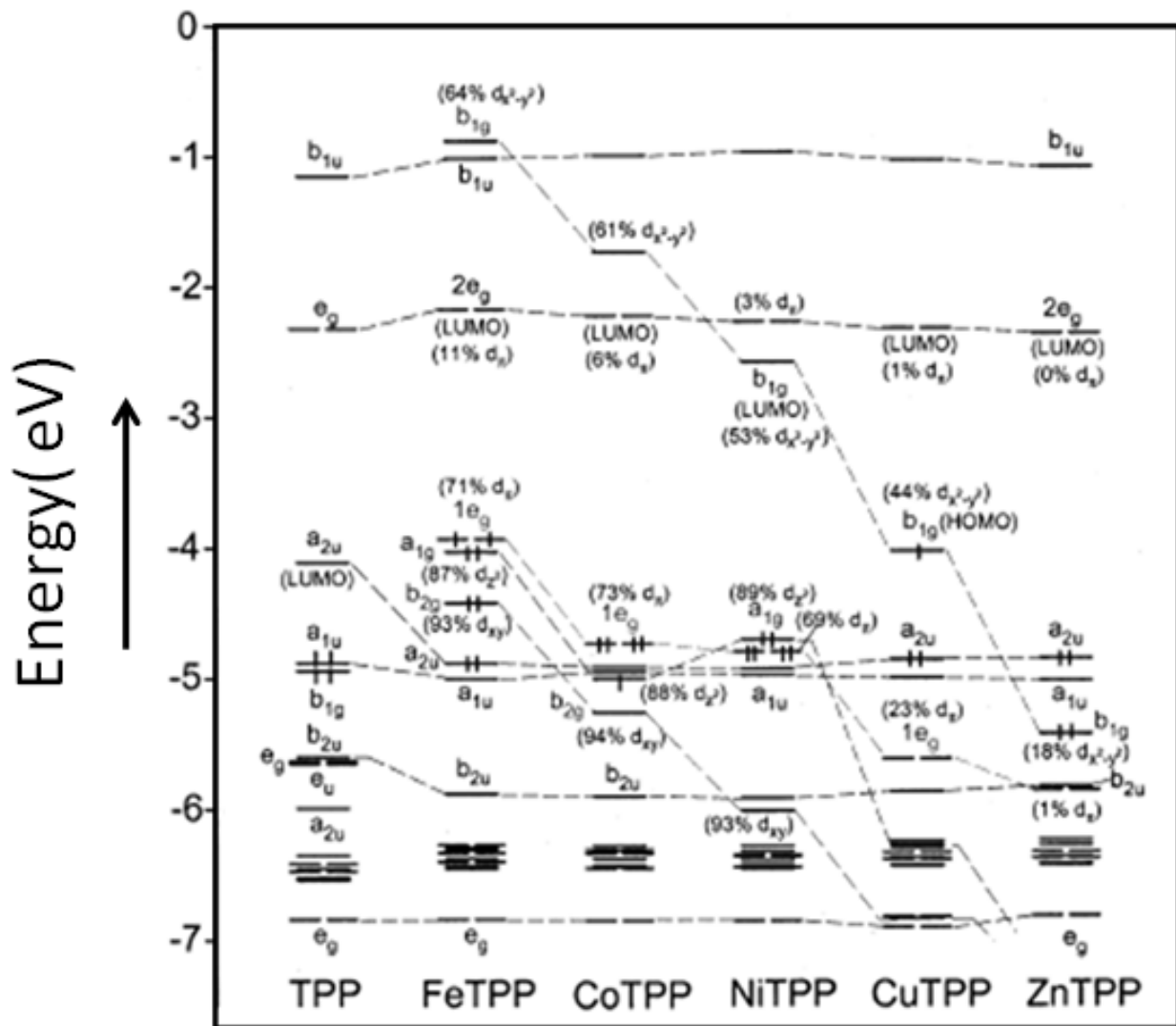
Figure 1 computed orbital energy levels for the outer orbitals of TPP and MTPP single molecules (Gas Phase). [Reproduced from ref.3]

In addition to the peak at around 4eV, the FeTPP-Cl spectrum shows addition peaks at about 0.7 eV and 2.4eV above the Fermi level. As expected from the theoretical calculations the unoccupied states near Fermi level are associated to unoccupied 3d central iron atom orbitals in case of FeTPP. Therefore, we can assign the first feature above the Fermi level to the singly unoccupied LUMO $1e_g$ state and second feature to the $2e_g$ state.[3] H_2TPP spectrum is shown for

comparison with MTPP spectrum in order to highlight the influence of partially filled 3d orbitals on unoccupied density of states. As per theoretical calculations the LUMO of H_2TPP is a_{2u} state with ligand character and we assign the peak at about 1.1eV to the LUMO of H_2TPP.
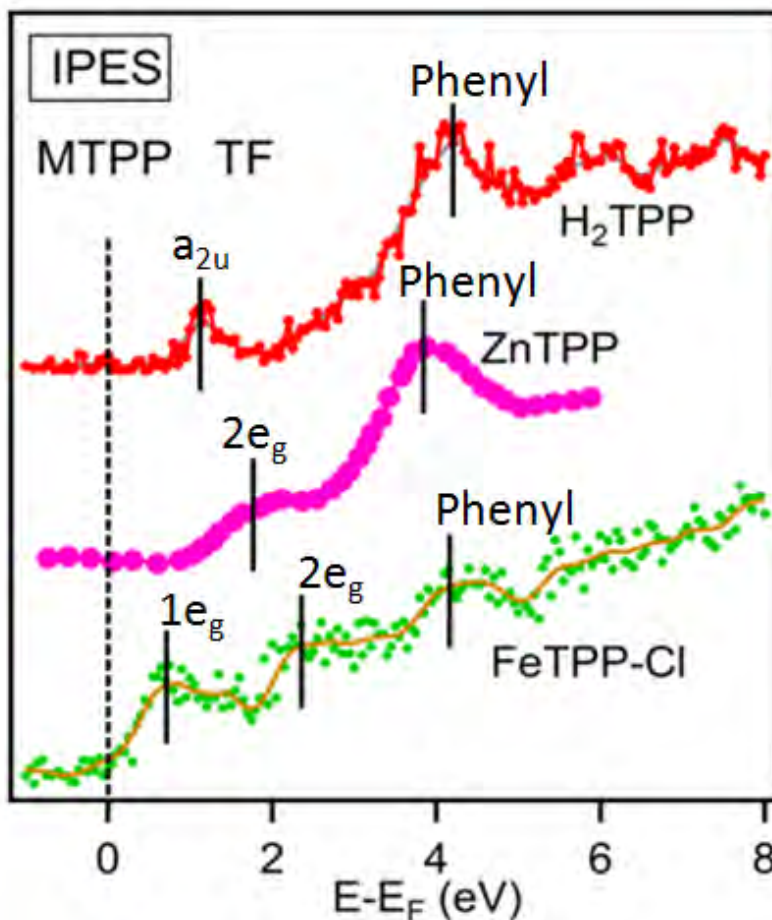
Figure 2 IPES spectrum for about 8nm FeTPP-Cl, ZnTPP and H_2TPP thin films

DFT calculations show that in the occupied states, the HOMO is assigned to the singly occupied e_g and lie above a_{1g} state in case of FeTPP.

5.1.2 MTPP Interfaces

As discussed in the first chapter, interfacial electronic properties at metal-molecule interfaces plays crucial role in the performance of molecular electronic devices. In this section, we explore the potential of graphene in altering the interfacial energy level alignment, influencing interfacial charge transfer, interface dipole, metal-molecule hybridization and charge injection barriers. Graphene can be grown on various metallic substrates such as Au, Ag, Co, Ni, and Pt etc. and presents peculiar behavior related to density of states, corrugation, work function changes and distance from underlying metallic substrate. We specifically choose Gr/Ni(111) and Gr/Pt(111) systems for our study due to different characteristics of graphene for these systems.

94

Another important issue is the conformation of Tetraphenylporphyrins molecules adopted on metallic substrates. Due to intramolecular strain between porphyrin core and peripheral phenyl groups, planar conformation is energetically not favorable. In the gas phase, phenyl groups align at about 74° with respect to porphyrin core which adopts aplanar configuration. However, on metallic substrates, porphyrin core adopts a saddle-shaped structure in order to minimize the steric hindrance, in the monolayer regime.

In general, metallo-tetraporphyrins adopt densely packed ordered structures on strongly interacting surfaces. STM studies for the adsorption of FeTPP, CoTPP on Ag(111) confirms the saddle–shaped molecular conformer.[5]

5.2 C-based Substrates

5.2.1 Graphene/Ni(111)

Graphene on Ni111) can be grown using hydrocarbons such as ethylene or propylene under UHV conditions by keeping Ni(111) at elevated temperature . Growth temperature and carbon content of the substrate notably influence the graphene growth [56] as indicated in Figure 3. Growth temperature and carbon content can lead to epitaxial graphene growth or with rotated domains with respect to underlying substrate. There is a probability of nickel carbide formation during growth of graphene on Ni(111) but with appropriate selection of growth conditions carbide formation can be avoided or it can be converted to graphene.
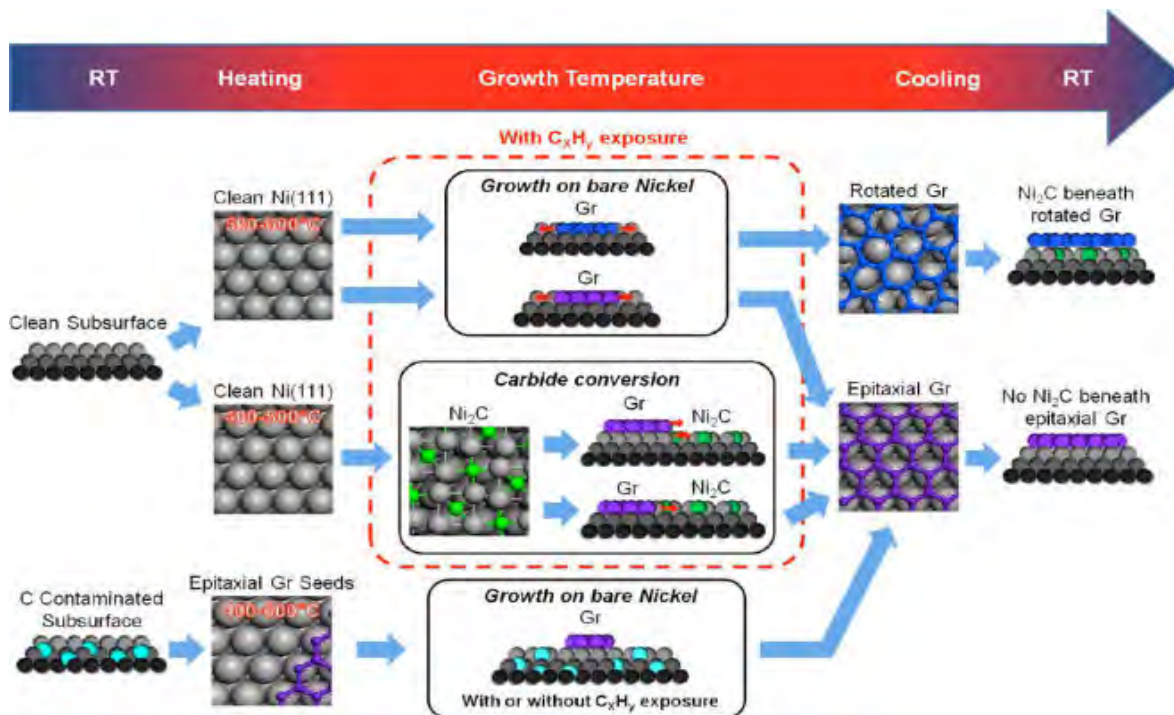

Figure 3 Schematic overview of the different graphene growth routes on Ni(111). [Reproduced from ref. 56]

Angle resolved photoemission measurements show that electronic structure of graphene is modified due to interaction with Ni(111). DFT as well as PES studies show strong chemical interaction between Ni and graphene resulting in hybridization of π states of graphene and Ni 3d band.[57] It results in 2.4eV down shift of π states of graphene and opening of gap in graphene. π-band is observed at a binding energy of 10.1eV with respect to Fermi level.

C Kedge NEXAFS shows that C 1s to π* transitions exhibits double peak feature as compared to single peak in case of graphite. This indicates two unoccupied interface states for epitaxial graphene–Ni(111) due to the hybridization of Ni(111) with graphene.
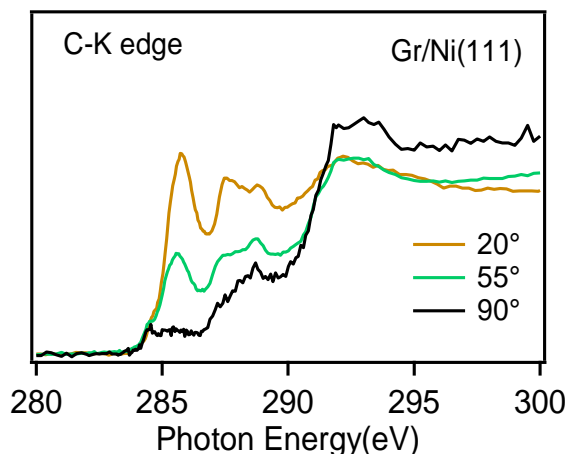

Figure 4

Figure 5

Figure 4 C K edge for the epitaxial Gr/Ni(111) at different X-ray angle of incidence and Figure 5 PES C1s for Gr/Ni(111) (This work) along with LEED.

C K edge NEXAFS at photon incidence angles of 20°, 55° and 90° is shown in Figure 4. The epitaxial Gr/Ni(111) C K edge is primarily dominated by two main peaks at 285.5V and 287.1eV. Theoretical calculations [61] indicate that the peak at 285.5eV originates by transitions from C1s to interface state above Fermi level formed due to Cp$_z$-Ni 3d hybridization. The other peak at 287.1eV is due to the dipole transition of an electron from the C1s core level to the interface state above the Fermi level formed by the hybridization of from Cp$_z$-Ni p$_x$,p$_y$,3d orbitals. C1s of graphene/Ni(111) exhibits a sharp peak at 284.8eV as confirmed by fitting analysis. The small contribution is at 284.4eV is due to graphitic carbon. [Figure 5]

5.2.2 Graphene/Pt(111)

Graphene growth of Pt(111) can be performed by thermal decomposition of hydrocarbons similar to graphene on Ni(111) however graphene growth requires higher substrate temperatures of above 1000K .Due to lower solubility and reactivity of carbon with Pt(111) as compared to Ni(111), carbide formation is not observed on Pt(111) in contrast to Ni(111).[59] The comparison of C1s fitting analysis for Gr/Pt(111) and Gr/Ni(111) clearly demonstrate the absence of carbide on Pt(111) as shown in Figure 7. Angle resolved photoemission studies

demonstrate that the electronic structure of graphene on Pt(111) is least perturbed as compared to free standing graphene. DFT calculations suggest that due to difference in work function of free standing graphene and Pt(111) substrate, graphene on Pt(111) is p doped. [58] The LEED images show clearly six spots due to Pt(111) surface due to six fold symmetric structure. Moiré patterns are observed due to possible rotation of graphene lattice domains with respect to Pt(111) lattice. There is a good resemblance of the LEED image with the literature.[58] C Kedge NEXAFS shows that C 1s to π^* transitions exhibits single peak feature in contrast to Gr/Ni(111) suggesting a weaker interaction of graphene with Pt(111). [58]
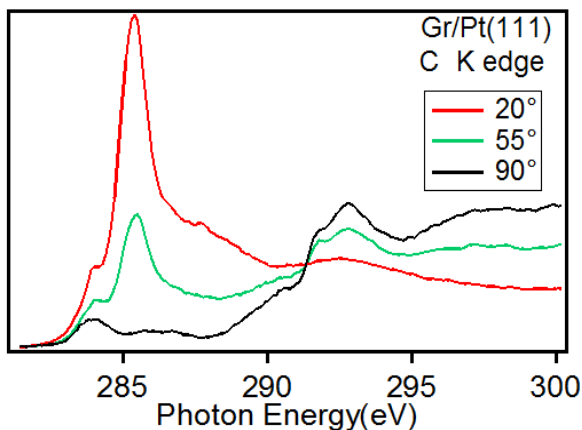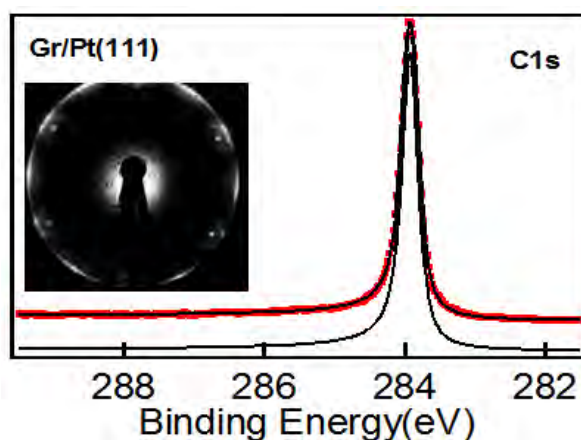
Figure 6   Figure 7
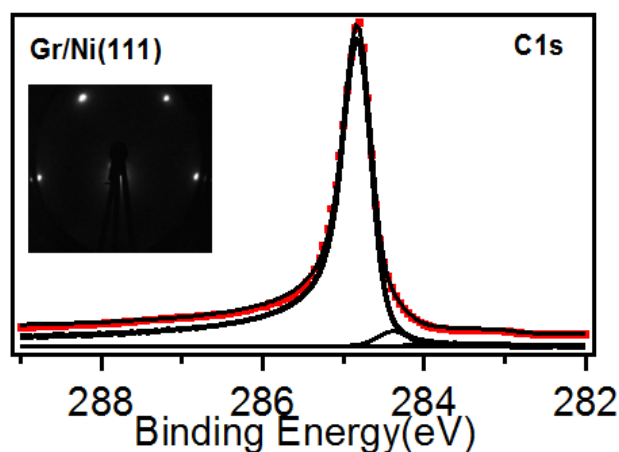
Figure 6 C K edge for the Gr/Pt(111) at different X-ray angle of incidence and Figure 7 FPES C1s for Gr/Pt(111) along with LEED (This work).
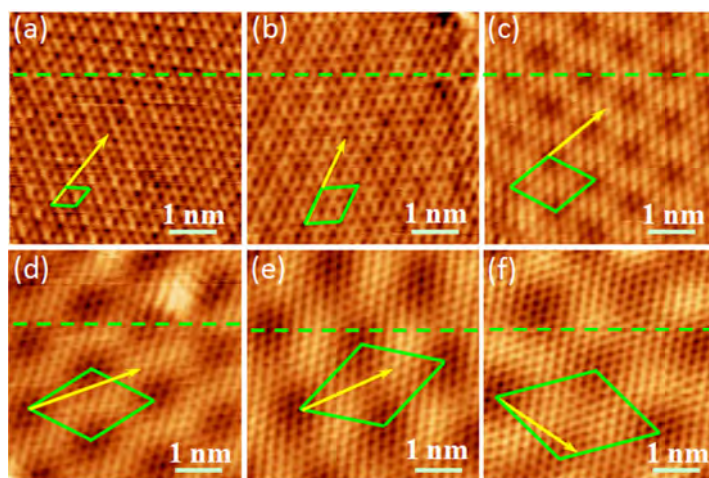
Figure 8 Atomic resolution STM image of six rotational domains with different moiré supercell with respect to primary graphene lattice (Vs=−0.4 V, I=0.2 nA): (a) 2×2, (b) 3×3, (c) 4×4, (d) ($\sqrt{37}\times\sqrt{37}$) R21°, (e) ($\sqrt{61}\times\sqrt{61}$) R26°, and (f) ($\sqrt{67}\times\sqrt{67}$) R12°. The $\langle 21\bar{1}\bar{1}0\rangle$ direction of graphene lattices is indicated by the yellow arrows and moiré unit cells are in green rhombus. [reproduced from ref.60]

It is worthwhile to mention that there are considerable differences in the epitaxial graphene on Ni(111) and Pt(111) induced by lattice mismatch with underlying substrate. STM studies confirm that corrugations of graphene domains are 0.02nm in case of Gr/Ni(111) with least lattice mismatch between graphene honeycomb lattice and Ni(111) hexagonal lattice underneath.[15] However, in case of Gr/Pt(111) STM studies show that the presence of two categories of moiré superstructures In the first category, the lattice vectors of moiré superstructures are parallel to the lattice vector of graphene as shown in Figure 8. The corrugation of these domains is within 0.03 nm, indicating the graphene film is very flat without much distortion in vertical direction. In the second category, there are angles between the lattice vectors of moiré superstructures and graphene as shown in Figure. The corrugation of these domains increased to 0.05–0.08 nm.[60] The corrugation difference originates from the different rotation angles of each domain with respect to the Pt substrate.

STM combined with C1s core level photoemission, shows that the presence of defects and the morphological properties on graphene grown on Ni(111) [14] . Moreover, it has been observed that graphene is more corrugated on Pt(111) as compared to Ni(111).[60] The Gr layer separation is 0.31 nm in case of Pt(111) and 0.21nm in case of Ni(111).[15]

5.2.3 HOPG

Highly oriented pyrolytic graphite is layered carbon material with highest degree of three-dimensional ordering in C-axes perpendicular to the surface of the substrate. It is obtained by graphitization heat treatment of pyrolytic carbon or by chemical vapor deposition at temperatures above 2500°K. The sp^2 hybridized adjacent layers of carbon are separated by 0.34nm and exhibits van der waals interaction. It is evident that C Kedge of HOPG is primarily dominated by two main peaks at 285.4eV and 291.8eV. The C Kedge spectrum of pristine HOPG shows a sharp resonance at a photon energy of 285.4 eV, corresponding to a C 1s - π* transition. While the second dominant feature at 292 eV shows a double peak, corresponding to C 1s - σ*. This double resonance arises from excitonic (the sharp resonance at 291.8 eV) and band-like contributions (the broader signal at around 293 eV).[61] This region between (286eV to 290eV) is related to interlayer states as confirmed theoretically [61]. Band structure calculations for HOPG predicts the presence of three dimensional states in the gap between the bonding and antibonding states at the Brillouin zone center. These three-dimensional states exist in the gap between the carbon layers.

The C Kedge spectrum of pristine HOPG shows a sharp resonance at a photon energy of 285.4 eV, corresponding to a C 1s - π* transition.(Figure 9) While the second dominant feature at about 292 eV shows a double peak, corresponding to C 1s - σ*. This double resonance arises from excitonic (the sharp resonance at 291.8 eV) and band-like contributions (the broader signal at around 293eV).[46,51] The region between 286eV and 290eV is related to interlayer states as confirmed by theoretical calculations.[51] Band structure calculations for HOPG predicts the presence of three dimensional states in the gap between the bonding and antibonding states at the

Brillouin zone center. These three-dimensional states exist in the gap between the carbon layers. Therefore, existence of such states provides useful information about the confinement of specie into HOPG layered structure.
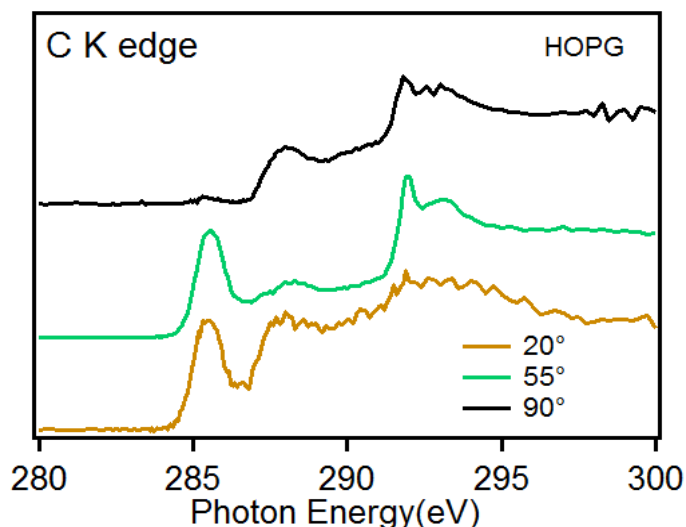

Figure 9 C K edge for the HOPG at different X-ray angle of incidence (This work).

5.3 Interfacial Electronic properties of Tetraphenyl porphyrin/Graphene interface on ferromagnetic surface

5.3.1 Influence of Graphene-Substrate Coupling On Interfacial Electronic Properties

Graphene holds the potential to alter the molecule-substrate interaction effects, including hybridization, charge transfer etc. thereby, notably influencing charge transport at interfaces and energy level alignment. [4] Graphene has been found to decouple FePc from Ir(111) while FePc-Ni(111) interaction has been suggested for FePc on Gr/Ni(111) system.[7] An intermediate graphene layer has been found to alter the molecule-substrate hybridization. The presence of an interfacial state is ascribed in the literature to the hybridization of central metal atom orbitals with the substrate.[7] An interface state at 0.3 eV has been observed for FePc on Gr/Ni(111) system in contrast to Gr/Ir(111) where no interface state has been observed. Similar interfacial state has been observed for other tetrapyrrole complexes systems such as FePc on Au(111), CoOEP on Ag(111) and related systems.[6]   In addition, interaction of central metal atom with underlying substrate is also influenced by different filling of the $3d$ orbitals, which influences the properties of the substrate-molecule interface.[8]

Metal(III) porphyrin complexes occur with chloride ligands such as AuTPP-Cl, MnTPP-Cl and FeTPP-Cl where the axial Cl ligand exhibits oxidation state of -1 (we have Fe 2+ without Cl and Fe 3+ with Cl) and result stable enough for thermal evaporation. However, it has been reported that chloride ligand can be removed by annealing or by interaction with substrate resulting in a change of the central metal atom oxidation state and leading to possible spintronics

99

application.[9] Although, the dechlorination of FeOEP-Cl and FeTPP-Cl on metallic substrates has been studied using STM however a detailed model is still lacking. Dechlorination of FeOEP-Cl is observed on epitaxially grown Ni on Cu(100) with a change of the I ron oxidation state and consequently leading to a ferromagnetic coupling with the substrate. DFT calculations performed for this system indicate that a ferromagnetic coupling is possible only after dechlorination which leads to change of iron oxidation state from +3 to +2 as depicted by XAS analyses.[10] Recent STM studies for the adsorption of FeOEP-Cl on Cu(111) cooled at 80K [11] and onto Au(111) [12] reveal a partial dechlorination of the molecules after adsorption. In case of Cu(111), STM images show the presence of both dechlorinated FeOPE-Cl molecules as well as intact molecules. The one type of species with a central protrusion are reported to be intact FeOEP-Cl molecule with the chlorine atom oriented away from the surface while other species with a central depression was assigned as the dechlorinated FeOEP.[11] In addition, DFT calculations reveal that molecules with chlorine pointing upward are energetically more favorable. STM studies reveal the presence of chlorine on substrate in case of MnTPP-Cl on Co(001) and AuTPP-Cl on Au(111).

  In this section, we investigate the interfacial electronic properties for the deposition of FeTPP-Cl on epitaxial Gr/Ni(111), Gr/Pt(111) and HOPG. These substrates are selected to explore the processes influencing the interfacial charge transfer in order to highlight the impact of dissimilar graphene-substrate coupling. HOPG has been found to interact weakly with tetrapyrrole complexes, therefore is taken as the reference substrate to compare interaction of FeTPP-Cl on Gr/Pt(111) and Gr/Ni(111). Dispersion corrected DFT calculations confirm these findings [21].

Due to these dissimilarities the molecule–substrate coupling, the charge transfer and the energy level alignment are expected to be notably distinct. In order to highlight the consequences of this unique substrate driven interactions   and interface energetics we analyze the FeTPP-Cl adsorption on the mentioned Gr/Ni(111), Gr/Pt(111) and HOPG substrates, in the monolayer and multilayer regime utilizing a multi-technique characterization approach employiing X-ray photoemission and X-ray absorption spectroscopy. Recent theoretical calculations [17] propose that, among the MTPP, only the FeTPP molecule should induce an opening of the Graphene gap when deposited. If confirmed this could be a promising topic in the graphene technological applications. This issue is one of the motivations of our work.

5.3.2 Valence band analysis

Figure 10(a,b) shows the evolution of the valence states of FeTPP-Cl on Gr/Ni(111), Gr/Pt(111) and HOPG in the monolayer and multilayer regime. The valence band spectra for the deposition of FeTPP-Cl on Gr/Ni(111) and Gr/Pt(111) are shown in Figure 10a. The two grey curves, related to the uncovered Gr/Ni(111) and Gr/Pt(111) reveal that graphene related features are clearly detectable at about 10eV for Gr/Ni(111) and at about 8eV for Gr/Pt(111) related to the different Gr doping. As mentioned above, due to the significantly different nature of graphene-substrate interaction and corrugation, the interfacial electronic properties are notably distinct in

the two cases. In order to single out the impact of intermediate graphene layer on metal-molecule interaction in case of FeTPP-Cl/Gr/Ni(111) and FeTPP-Cl/Gr/Pt(111) interfaces, we analyzed in more details the spectral region close to Fermi level as shown in Figure 11. The FeTPP-Cl adsorption on Gr/Ni(111) leads to a new feature at about 0.3 eV near Fermi level along with reduction of the Gr feature and the Ni 3d band. This peak can be observed for the 0.5ML and ~1ML coverage of FeTPP-Cl deposited on Gr/Ni(111) at RTand disappears at higher converages which is the behavior of an interfacial state [7]. The interfacial state can be due to the overlapping of the partially empty out-of-plane d like orbitals of Fe with the hybridized d–π states of Ni-Gr. The existence of an interfacial state can be associated with the charge transfer from substrate to the molecule. As noted previously, the presence of such interfacial state shows the coupling of molecule with substrate as observed for the adsorption of FePc on Gr/Ni(111)[7]. and for adsorption of other tetrapyrrole complexes on metallic substrates such as CoTPP on Ag(111)[3], FePc and CoPc on Au(111)[19]. On the other hand in contrast to Gr/Ni(111). no interface state has been observed for the deposition of FeTPP-Cl on Gr/Pt(111) shown in Figure 12 suggesting that the presence of a weakly interacting graphene on Pt(111) decouple FeTPP-Cl from the underlying Pt(111) substrate The FeTPP-Cl/HOPG interfaces are shown in Figure 10(b). The presented valence band of HOPG is in agreement with literature; in particular it is dominated by the peak at about 7.6eV corresponding to π states of HOPG [20]. The intensity of HOPG valence states peaks decreases as the thickness of FeTPP-Cl thin films increases. It can be inferred that hybridization of empty Fe 3d orbitals with underlying Pt(111) and HOPG is feeble.
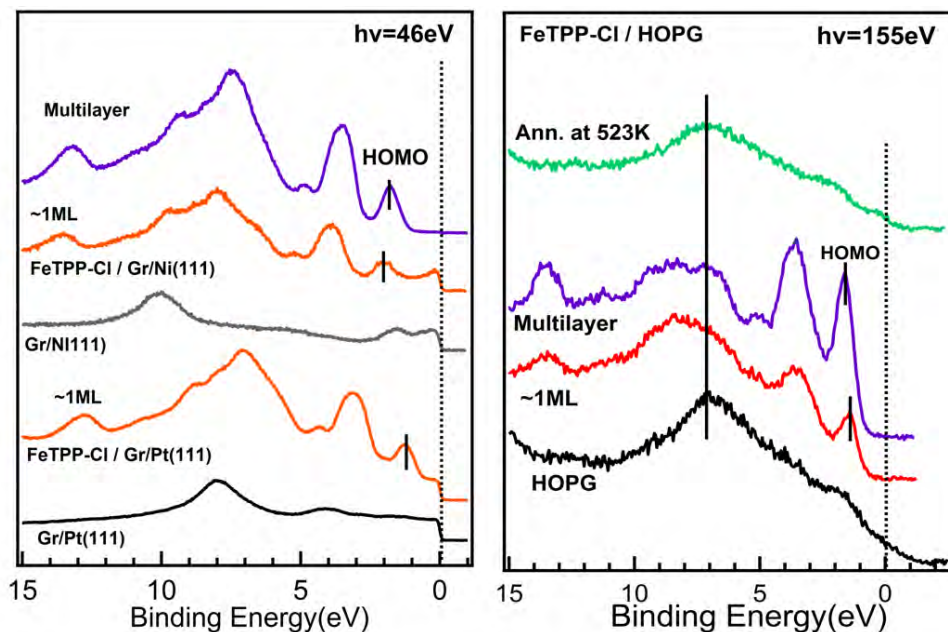

Figure 10(a)   Figure 10(b)

Figure 10(a) Valence band spectra for the depostion of FeTPP-Cl on Gr/Ni(111) and Gr/Pt(111) on monolyar and multilayer regime. (b) Valance band spectra for the depostion of FeTPP-Cl on HOPG in monolayer and multilayer regime.

At multilayer thickness the spectrum is primarily influenced by valence states corresponding to FeTPP-Cl molecule on HOPG. There is an apparent similarity between the valence band spectrums of the HOPG with that of annealed film at 523K as shown in the Figure 10(b). This result clearly indicates towards a weaker interaction of FeTPP-Cl with HOPG. No valence state corresponding to the FeTPP-Cl molecule can be detected which leads to the conclusion that FeTPP-Cl molecule is desorbed completely from the substrate.

It seems that the electronic structure of 1 ML FeTPP-Cl on HOPG is only weakly perturbed due to adsorption, but dechlorinated, as discussed in the next paragraph. The weak interaction is coherent with STM studies for the adsorption of porphyrins on HOPG which show that although porphyrin molecules lie flat on HOPG the interaction with the substrate not sufficient to form a stable chemical bond.[21] Importantly, no interfacial state has been observed for the deposition of FeTPP-Cl on HOPG. This result seems to be of more general significance as STM study for the adsorption of H$_2$OEP and CoOEP on HOPG confirms that the adsorption strength is directed by the interactions between the porphyrin ring and the HOPG surface while the central metal atom does not play a significant role in the interaction with HOPG.[21]
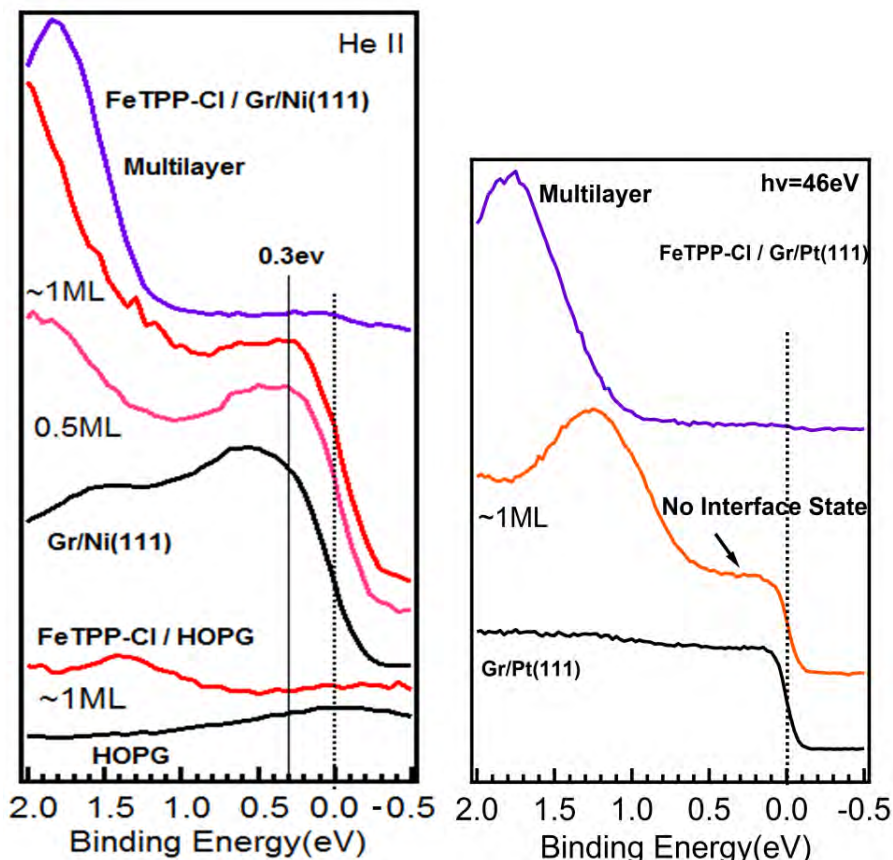

Figure 11   Figure 12

Figure 11 Valence band spectra for the deposition of FeTPP-Cl on Gr/Ni(111) and HOPG and (12) Gr/Pt(111). No interface state at 0.3 eV for FeTPP-Cl/Gr/Pt(111).

In order to investigate the presence of chlorine in the valence band spectrum, FeTPP-Cl valence band spectrum is compared with CoTPP monolayer spectrum obtained by annealing the CoTPP multilayer at 523 K as shown in Figure 13. Notably, FeTPP-Cl monolayer obtained by annealing multilayer at 523K shows good resemblance with CoTPP monolayer on Gr/Ni(111) and depicts absence of chlorine. Comparison of valence band spectrum of CoTPP molecule with room temperature deposited FeTPP-Cl thin films allows to assign peak at about 5eV above Fermi level to the chlorine. The annealing of FeTPP-Cl multilayer at about 523K does not result in complete desorption of FeTPP-Cl molecules form Gr/Ni(111) and Gr/Pt(111) indicating higher coupling strength with respect to HOPG. The presence of a peak at about 5eV above Fermi level in case of multilayer curve shows the presence of chlorine as shown in Figure 10(a).
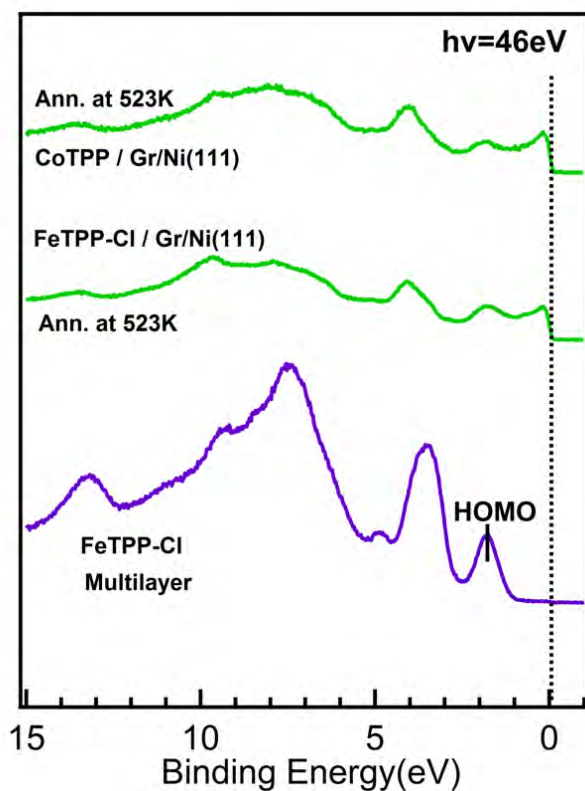
Figure 13 Valence band for the annealing of FeTPP-Cl and CoTPP multilayer on Gr/Ni(111) at 523K

In order to further investigate the energy level alignment at FeTPP-Cl/Gr/Ni(111), FeTPP-Cl/Gr/Pt(111) and FeTPP-Cl/HOPG interfaces, hole injection barriers and work function values are measured in the monolayer regime using secondary cutoff photoemission spectroscopy as shown in Figure 14. Hole injection barriers are obtained by measuring difference between Fermi level and HOMO onset binding energy positions. The difference between the substrate and molecular deposit system WF defines the interface dipole (Δ) (See Figure 1, Chapter 1). It is evident that interface dipole at FeTPP-Cl/Gr/Ni(111) interface is 0.5eV as compared to 0.25eV for FeTPP-Cl/Gr/Pt(111) interface. Importantly, hole injection barriers and interface dipole

values for FeTPP-Cl/HOPG interface show good agreement with that of FeTPP-Cl/Gr/Pt(111) interface. As discussed earlier, graphene on Pt(111) behaves as a free standing graphene and exhibits weaker graphene−substrate interaction. It results in a weaker molecule-substrate interactions for FeTPP-Cl/Gr/Pt(111) interface similar to FeTPP-Cl/HOPG interface (interplanar separation is 0.34nm). As shown in Figure 11 comparatively, FeTPP-Cl/Gr/Ni(111) interface exhibits stronger molecule-substrate interactions due to higher proximity of graphene to Ni(111) than Pt(111).

Due to such dissimilarities molecule–substrate coupling appears notably distinct in the two cases. The charge injection barriers and work function at FeTPP-Cl/Gr/Pt(111) are reduced almost by 50% as compared to FeTPP-Cl/Gr/Ni(111) interface. The probable cause of higher work function alterations for FeTPP-Cl /Gr/Ni(111) system can be attributed to the significant contribution from charge transfer, push back effect and hybridization effects.
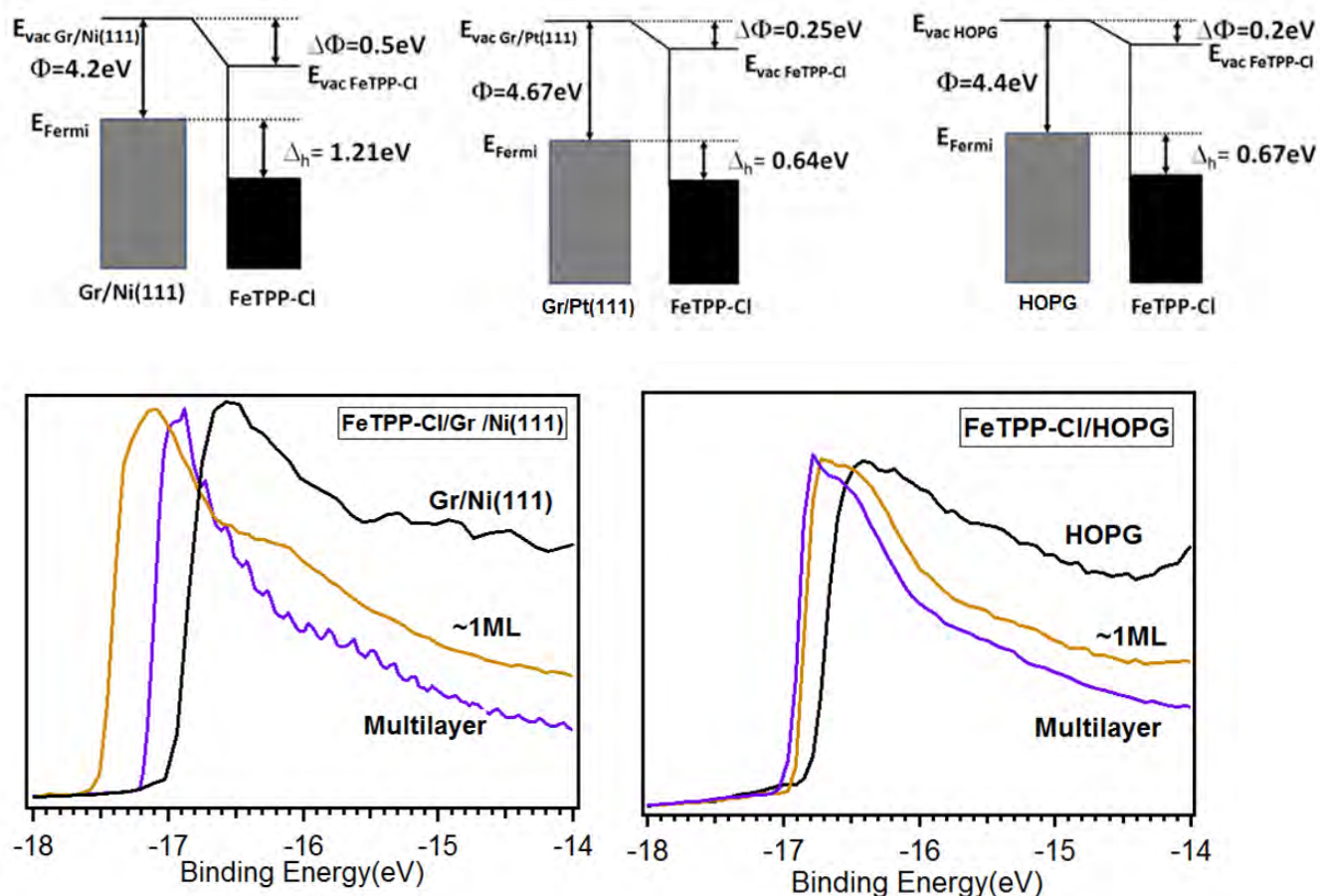

Figure.14 Schematic representation of energy level alignment and hole injection barriers for the deposition of FeTPP-Cl on Gr/Ni(111), Gr/Pt(111) and HOPG in the monolayer regime. Bottom panel: example of secondary cut off measurements of FeTPP-Cl deposited onto Gr/Ni(111) and HOPG

As previously discussed, due to smaller graphene-Ni(111) separation, FeTPP-Cl molecules are exposed to electron density from Ni(111) substrate, thereby enhancing possibility of push back effect. It is suggested by valence band analysis that there is notable hybridization of FeTPP-Cl with Gr/Ni(111) , which further contributes in lowering the work function in monolayer regime. On the other hand, in case of FeTPP-Cl/Gr/Pt(111) system, push back effect and hybridization effects are expected to be feeble due to higher graphene–Pt(111) separation as compared to graphene-Ni(111). It demonstrates the ability of graphene to alter interfacial electronic properties at metal-molecule interface. In general, adsorption of MTPP on metallic substrates results in significant lowering of work function. For example in MTPP interfaces the work function of Ag(111) has been found to decrease by 0.72eV ,0.91eV and 0.84eV for the adsorption of CoTPP, CoTTBPP and CoOEP receptively.[23] Notable hybridization and charge transfer at the interface are reported to contribute towards decrease of work function in case of metal substrates.

However, the situation is unique in case of Gr/Ni(111) and Gr/Pt(111) due to the presence of intermediate graphene layer that can influence metal-molecule hybridization and probably push back effect. On the other hand HOPG interaction is attributed by the presence of delocalized π electron, due to which the interaction between FeTPP-Cl and HOPG should be primarily Van der Waals in nature. Therefore significant push back effect and hybridization effects are not expected for FeTPP-Cl/HOPG system resulting in small work function changes of about 0.2eV.

Substrate	Thickness	Work function(eV)
Gr/Ni(111)	0	4.2
	~1ML	3.7
	Multilayer	4.1
HOPG	0	4.4
	~1ML	4.2
	Multilayer	4.1
Gr/Pt(111)	0	4.65
	~1ML	4.4
	Multilayer	4.1

Table-1 Work function variation for the deposition of FeTPP-Cl on Gr/Ni(111), Gr/Pt(111) and HOPG corresponding to monolayer and multilayer regime.

5.3.3 X-ray photoemission core levels analysis

We analyze Fe2p and Cl 2p core level XPS to clarify in detail the probable change of iron oxidation state due to dechlorination of FeTPP-Cl. Figure 15 shows the Fe $2p_{3/2}$ XPS spectrum for the deposition of FeTPP-Cl on Gr/Ni(111), Gr/Pt(111) and HOPG. Curve fitting of Fe $2p_{3/2}$

XPS spectrum is performed by Kol-XPD software for ~1ML and multilayer coverages in order to foster investigation of change in iron oxidation state due to loss of chlorine upon interaction with substrate. Although, Fe 2p core level exhibits complex multiplet structure described by utilizing Zeeman-like final state effect [24] or splitting of states based on total angular momentum [25], it is possible to model sublevels by two peaks while the third peak represents a satellite due to Plasmon loss as shown in Figure 15.[26]

Peak A and B corresponding to two sublevels are separated by 1.5eV while peak C related to Plasmon loss is close to 712 eV in the three 1ML cases. The presence of Plasmon loss peak at about 712 eV is a typical finger print of +2 oxidation state for iron.[25] In addition, multilayer Fe 2p spectrum (top panel in Figure. 15) does not show this plasmon loss peak within our resolution limits, indicating a change of Fe oxidation with film thickness. At FeTPP-Cl coverages above 1ML the Fe 2p core level multiplet structure becomes complex so more than two components are required for curve fitting.[25] Nevertheless, here the deconvolution of Fe 2p core level is intended to highlight the change of iron oxidation state utilizing the absence of plasmon loss peak at about 712 eV for multilayer coverage and does not necessarily represent the full complexity of these signals.

Analysis of Cl 2p XPS spectrum also provides useful information regarding interaction of chlorine with underlying substrates. Figure 16(a,b) shows the Cl 2p XPS spectra for the depsotion of FeTPP-Cl on Gr/Ni(111), Gr/Pt111) and HOPG. Surprisingly, Cl 2p XPS spectrum indicate towards complete dechlorination of FeTPP-Cl molecules for the adsorption on HOPG as no Cl 2p is detectable on HOPG at ~1ML coverage in contrast to Gr/Ni(111) and Gr/Pt(111).

Notably, the binding energy of Cl 2p is 197.9 eV on Gr/Pt(111) as compared to 198.7eV on Gr/Ni(111) at ~1ML coverage indicates that comparatively chlorine is strongly bound to Gr/Ni(111). However, at multilayer coverage the binding energy is at about 198.4eV in both cases, related to the Cl-Fe bond within the molecule.

Cl/N area ratio (~0.25 for FeTPP-Cl) for the spectrum taken at 515eV photon energy, extracted from our XPS data for FeTPP-Cl/Gr/Ni(111) and FeTPP-Cl/Gr/Pt(111) systems at the ~1ML coverage are found to be (~0.08) almost similar suggesting the extent of dechlorination on Gr/Ni(111) and Gr/Pt(111) is not significantly different. Moreover, comparing with the multilayer spectra this value indicate that the molecules dechlorinated are about 70% in both cases.
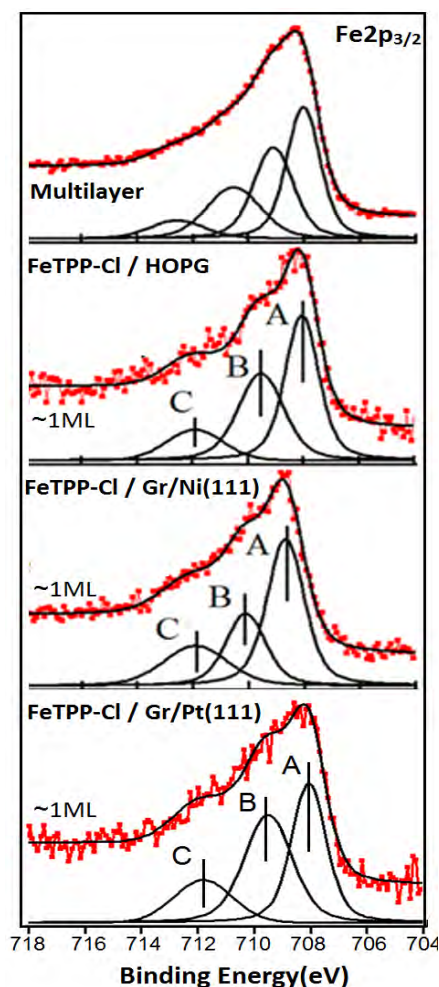
Figure.15 Fe 2p XPS for the deposition of FeTPP-Cl on Gr/Ni(111), Gr/Pt(111) and HOPG. Peak at about 712eV corresponds to plasmon loss for the +2 oxidation state of iron.

Partial dechlorination has been observed for FeOEP-Cl/Cu(111), FeTPP-Cl/Au(111), AuTPP-Cl/Au(111), MnTPP-Cl/Ag(111) and MnTPP-Cl/Co(001)[23,24] systems. STM analysis for the deposition of AuTPP-Cl on Au(111) reveals the presence of chlorine species on the Au(111) surface.[27] Similar observation has been reported for the adsorption of MnTPP-Cl on Co(001) thin film.[28,29]   In addition, STM based studies found partial dechlorination for FeTPP-Cl/Au(111) and FeOEP-Cl/Cu(111) systems. It appears that three possibilities can arise when FeTPP-Cl adsorb on metallic substrate.(i) FeTPP-Cl molecules do not get dechlorinated .(ii) Molecule get dechlorinated upon adsorption and chlorine get desorbed from the surface.(iii) Molecules get dechlorinated upon adsorption and chlorine get stabilized by the substrate as evident from STM investigation of AuTPP-Cl on Au(111) and MnTPP-Cl on Co(001). There is a possibility that chlorine get stabilized by the underlying metallic substrate. It may happen that in case of HOPG the chlorine does not get stabilized and desorbs. In this way complete absence of Cl 2p XPS signal can be justified. As discussed previously in the valance band analysis, Cl 2p core level shows that annealing at 523K leads to complete dechlorination of both single layers deposited on Gr/Ni(111) and Gr/Pt(111).
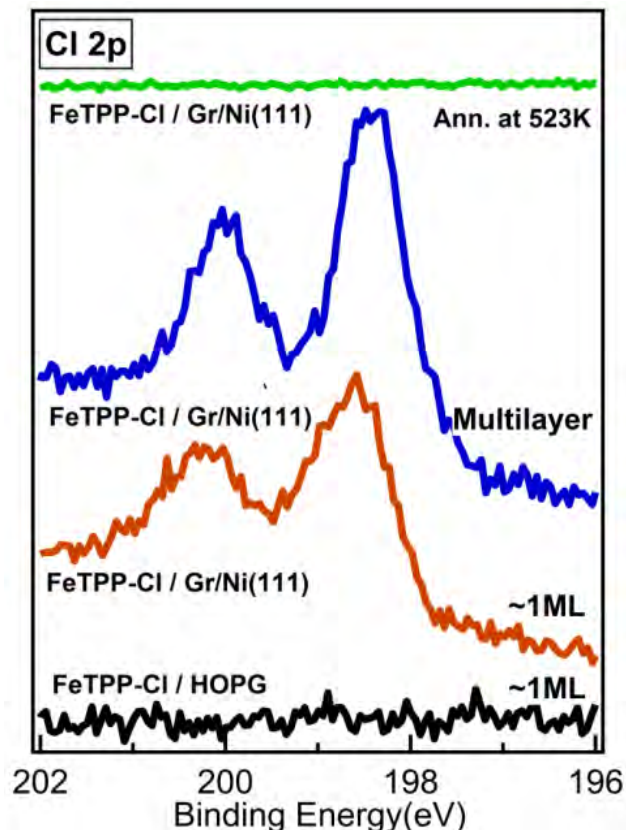
107
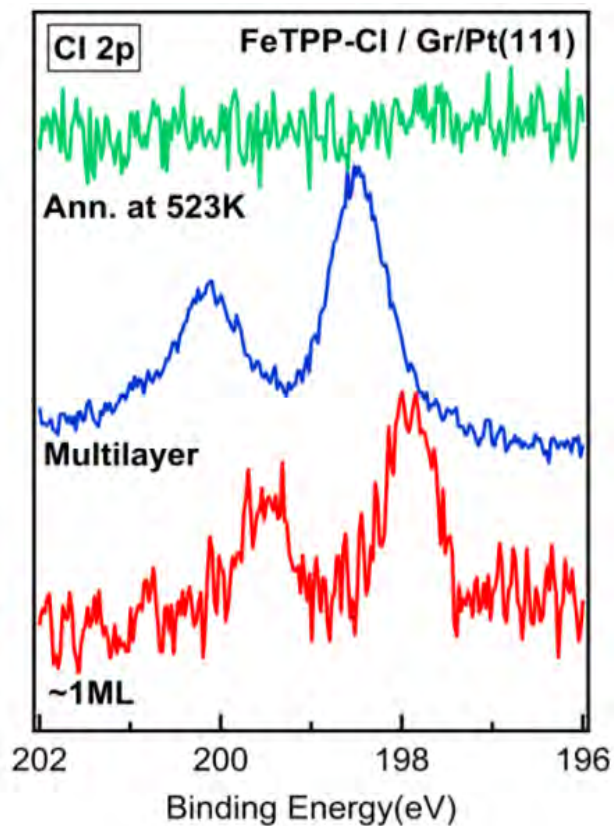
Figure 16(a)   Figure 16(b)

Figure 16(a) Cl 2p XPS for the depsotion of FeTPP-Cl on Gr/Ni(111) and HOPG,(b) Cl 2p XPS for the depsotion of FeTPP-Cl on Gr/Pt(111). Annealing at 523K results in comlete dechlorination of FTPP-Cl molecules.

C1s XPS analysis reveal notable dissimilarities for the deposition of FeTPP-Cl on Gr/Pt(111) and Gr/Ni(111) as demonstrated by distinct line shape of C1s line shape in monolayer regime. C1s fitting analysis reveals the causes for the significance differences in the C1s line shape at ~1ML coverage. Figure 17(a,b) shows the C1s spectra and their curve fitting for the deposition of FeTPP-Cl on Gr/Pt(111) and Gr/Ni(111). The deconvolution of XPS C1s spectrum for ~1ML and multilayer FeTPP-Cl coverages has been performed using four components due to presence of four inequivalent carbon atoms. The details of different components used for curve fitting is shown in table 2. Similar fitting model has been adopted for the adsorption of ZnTPP on Si(111) and Ag(110) [30].

 In case of FeTPP-Cl/Gr/Pt(111) system for ~1ML coverage the double peak is due to strong contribution from graphene C1s at   283.9eV(peak E) together with inequivalent FeTPP-Cl carbon atoms(See table 2). In case of FeTPP-Cl/Gr/Ni(111) system the line shape for ~1ML and multilayer coverage appears similar because the contribution from graphene C1s at 284.8eV(Peak F) merges with the signal from 24 phenyl carbon atoms at 284.8eV(Peak A) . In case of FeTPP-Cl/Gr/Pt(111)   the peak due to 8 pyrrolic C-C-C atoms(peak C)   merges with

peak E due to contribution from C1s of Gr/Pt(111) for ~1ML coverage due to proximity in the binding energy values. At multilayer coverage the signal from graphene C1s at 283.9eV is significantly suppressed and contribution from FeTPP-Cl carbon atoms dominates the spectrum. Therefore, C1s fitting involves four components corresponding to four inequivalent FeTPP-Cl carbon atoms and shows good agreement with ZnTPP multilayer fitting parameters on Si(111)[30]. An asymmetry of about 0.1 has been used for ~1ML coverage curve fitting using Doniach Sunjic convoluted Gaussian line shapes. FWHM for different components is found to be 0.4±0.1eV.
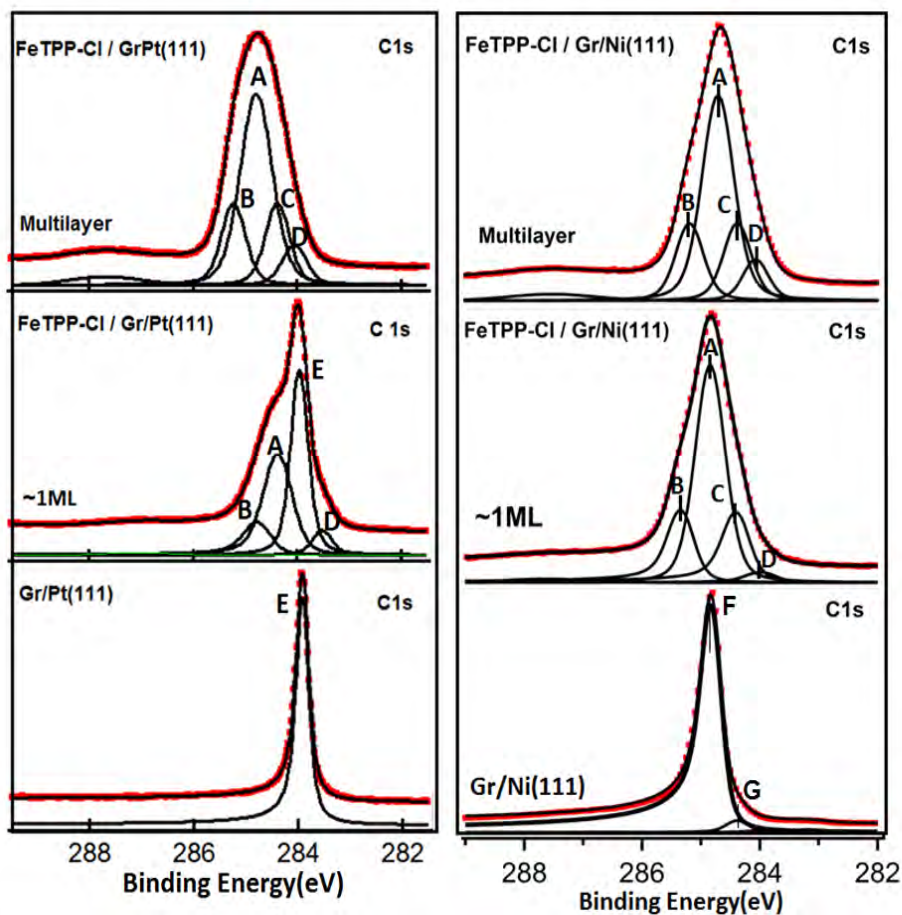
| Figure 17(a) | Figure 17(b) | Table 2 |
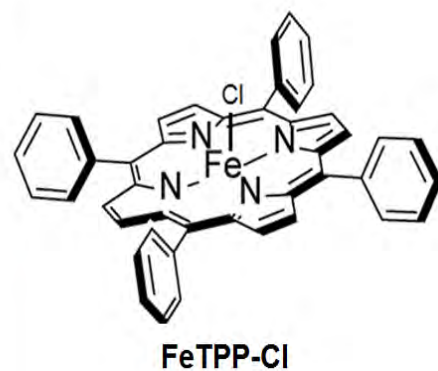
C1s Curve fitting components	
Peak A	C-Phenyl (24)
Peak B	Pyrrole C-C-N (8)
Peak C	Pyrrole C-C-C (8)
Peak D	C-bridge (4)
Peak E	C-Gr [Gr/Pt(111)]
Peak F	C-Gr [Gr/Ni(111)] (epitaxial carbon)
Peak G	C-Gr [Gr/Ni(111)] (Graphitic carbon)

Figure 17 (a) C1s XPS spectra for the deposition of FetPP-Cl on Gr/Pt(111) in monolayr and multilayr regime, (b) C1s XPS specra for the deposition of FetPP-Cl on Gr/Ni(111) in monolayr and multilayr regime.Table 2 shows the details of curve fitting components

Summarizing, the photoemission analysis reveals that dissimilarities in the coupling of FeTPP-Cl on Gr/Ni(111) and Gr/Pt(111) have significant implications on energy level alignment and overall charge redistribution at the interface.

Table-3 summarize the core level binding energy shifts for ~1ML and multilayer coverages and provides useful information about the charge transfer and energy level alignment at the interface for the deposition of FeTPP-Cl on Gr/Ni(111),Gr/Pt(111) and HOPG.

Fe $2p_{3/2}$ core level does not show notable chemical shift for ~1ML to multilayer thickness for FeTPP-Cl deposition on Gr/Pt (111) in contrast to Gr/Ni(111). It suggests that no significant charge transfer takes place from Gr/Pt(111) to FeTPP-Cl. Such a dearth of charge transfer across the interface induced by the graphene layer on Pt(111) can be attributed to the weaker interaction of Gr with the underlying Pt(111) substrate. This inference complements the absence of interface state in the valence band for FeTPP-Cl / Gr/Pt(111) system.

Substrate	Thickness	Fe $2p_{3/2}$ Binding energy(eV)	N 1s Binding Energy(eV)	C 1s Binding Energy(eV)	C l2p Binding Energy(eV)
Gr/Ni(111)	0			284.8	
	~1ML	708.6	399.0	284.8	198.7
	Multilayer	708.4	398.8	284.6	198.4
HOPG	0			284.4	
	~1ML	708.2	398.4	284.4	
	Multilayer	708.2	398.4	284.4	
Gr/Pt(111)	0			283.9	
	~1ML	708.2	398.2	283.9	197.9
	Multilayer	708.2	398.7	284.7	198.5

Table -3

In case of FeTPP-Cl/Gr/Pt(111) system, N1s and C1s PES core levels show a chemical shift towards higher binding energies which can be associated with core hole screening due to presence of metallic substrate and a difference in the charge transfer with respect to the Gr/Ni(111) case.

 Interestly, the Fe $2p_{3/2}$, N1s and C1s spectra do not show notable chemical shifts in case of FeTPP-Cl/ HOPG system which indicates a weak interaction of FeTPP-Cl with HOPG with almost no charge transfer and screening effects. It is worthwhile to mention that significant screening of core hole is generally observed for metallic substrates for the deposition of molecules in the monolayer regime.

Absence of chemical shift on HOPG can be associated to almost negligible core hole screening on HOPG due to its semi metallic character. The trend is similar to previous observations of weaker interaction of HOPG with tetrapyrrole complexes based on STM, DFT and Photoemission analysis [21].

On the contrary, Fe $2p_{3/2}$, C1s and N1s XPS data exhibit a chemical shift of about 0.2 eV towards lower binding energy for multilayer coverages in case of FeTPP-Cl/Gr/Ni(111). It can be inferred that although central metal atom interacts with Ni (111) as indicated by our previous

valence band analysis (6.3.2), there should be a redistribution of the charge due to different charge transfer channels involving the back donation of charge density from the molecular orbitals nitrogen to substrate. As summarized in Table 3 the trend of the C1s and N1s chemical shifts in case of FeTPP-Cl/Gr/Ni(111) interface is opposite to FeTPP-Cl/Gr/Pt(111), strongly suggesting additional mechanisms.

Given the possibility of charge back donation, there can be net transfer of charge density from molecule to substrate resulting in small but notable chemical shift of 0.2eV for Fe $2p_{3/2,}$ C1s and N1s towards lower binding energy for multilayer coverages. Actually, a back donation from nitrogen has been observed for CoOEP/Ag(111),CoTPP/Ag(100) and CoPc/Au systems resulting in redistribution of charge density across interface[31,32]. However, this point needs further exploration using DFT calculations in the future.

5.3.4 X ray Absorption analysis

Figure 18 shows the Fe L_3 edge spectra taken in PEY (Chapter 2) for FeTPP-Cl/Gr/Pt(111), FeTPP-Cl/Gr/Ni(111) and   FeTPP-Cl /HOPG systems in monolayer and multilayer regime. These data can enlighten the change of iron oxidation state due to dechlorination, found by core level phoptoemission.

It is worth noting that in these XAS measurements the transition from the initial 2p level has mainly the Fe 3d orbitals as final state (the p→s channel having 1/5 lower cross section) and dominate the spectrum. The line shape of spectrum changes from normal incidence to grazing incidence because of different orientation of empty (d_{z2}, d_{xy} etc.) orbitals. At grazing incidence orbitals with out-of.plane orientation such as d_{z2} dominate the spectrum as compared to in-plane orbitals such as d_{xy} and $d_{x2-y2.}$

It is evident that the line shapes of the spectra in monolayer regime are almost identical for the three substrates and indicates towards a prevalent +2 oxidation state for iron. The line shape for Fe +2 oxidation state is consistent with the deposition of Cl-FeOEP on Co/Cu(100) and Ni/Cu(100) substrate[10]. As discussed previously (5.3.3) core level analysis shows that almost 70% FeTPP-Cl are dechlorinated, therefore, we can expect that the majority of the molecules exhibits +2 oxidation state.

The relative intensity for the A_1 and A_2 peaks labelled in the Figure 18 reverses for the multilayer case, due to the change of the Fe oxidation state from +2 to +3 and coherent with the reported Fe L_3 line shape for +3 oxidation state.[10] We remind that in the FeTPP-Cl molecule the Fe central atom is bonded to two nitrogen and a chlorine atom with+3 oxidation state and a change of oxidation state is feasible only with Cl atom being detached from the iron. Thus, NEXAFS Fe L3 results indicate towards a substrate induced a dominant dechlorination of FeTPP-Cl for the three substrates.
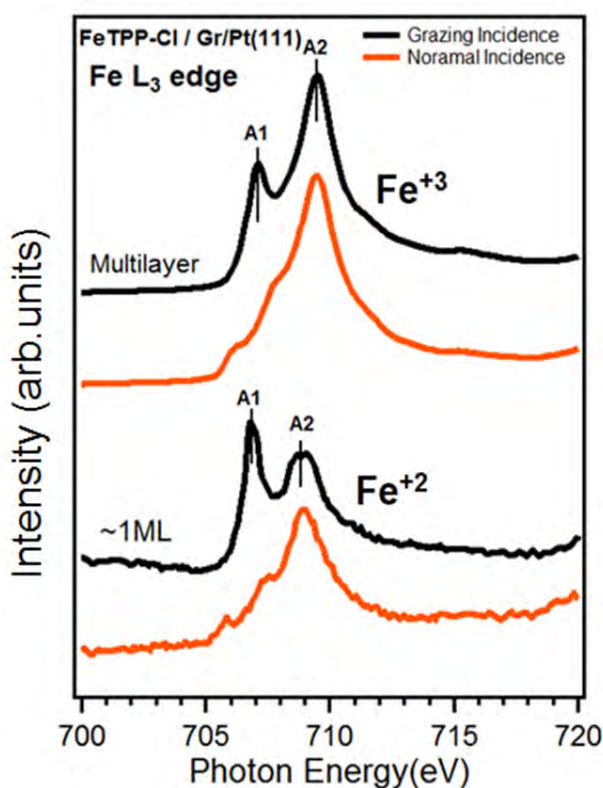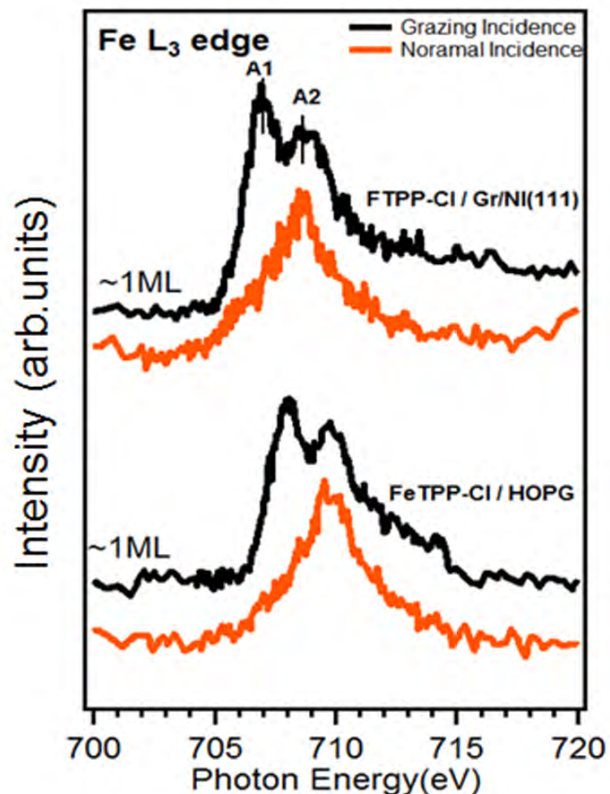
111

Figure 18(a)

Figure 18(b)

Figure 18(a) Fe L_3 edge NEXFS for the depsotion of FeTPP-Cl on Gr/Pt(111) in monolayer and multilayer regime; (b) Fe L_3 edge NEXFS for the depsotion of FeTPP-Cl on Gr/Ni(111) and HOPG in monolayer regime

Figure 19 shows the NEXAFS spectrum of the C K edge for the adsorption of FeTPP-Cl on Gr/Ni(111), Gr/Pt(111) and HOPG respectively. Due to the MTPP molecular flexibility stressed in 6.1 paragraph, the orientation of the phenyl rings is notably influenced by the type of substrate [30]. We have monitored the C K edge NEXAFS spectrum in the monolayer regime to investigate this point. The C K edge for the adsorption of FeTPP-Cl on Gr/Ni(111) is primarily dominated by two peaks at 284.55eV and 285.4eV in the low energy range. The intense peak at 285.4eV has a shoulder at about 285.65eV. The corresponding peak positions for the deposition on HOPG are shifted by 1eV towards higher photon energy and exhibits similar line shape in the low energy range. In case of Gr/Pt(111) the C K edge shows almost similar line shape to that of Gr/Ni(111) and HOPG. However, two peaks are at 284.1eV and 285eV in the low energy range present a more pronounced shoulder at 285.35V. In general there are three sets of equivalent carbon atoms in metalloporphyrins taking into account the symmetry considerations.[30] Based on DFT calculations the intense peak at about 285.4eV is assigned to C(1s) to π* involving phenyl rings, while the peaks at about 284.55eV and the weak shoulder at 285.65eV are due to the excitations of C(1s) to π* orbitals involving carbon atoms of the porphin ring [30].

At normal incidence the intensity of the peak at about 284.55eV corresponding to the macrocycle π transitions vanishes completely in comparison to grazing incidence for all the three substrate,s

confirming that FeTPP-Cl molecules lie flat on the Gr/Ni(111), GrPt(111) and HOPG. In addition the C K edge provides information about the orientation of the FeTPP-Cl phenyl groups after adsorption on to the three substrates. The dichroism of the intense peak at 285.4eV assigned to phenyl groups is less pronounced for the adsorption of FeTPP-Cl on Gr/Ni(111) and Gr/Pt(111) as compared to HOPG as shown in Figure 19. It suggests that there is higher randomness in the orientation of phenyl groups on Gr/Ni(111) and Gr/Pt(111) than on HOPG. Such a disorder in the orientation of phenyl groups is also observed for ZnTPP adsorbed on Si(111) while phenyl groups lie flat on Ag(110). Moreover the phenyl groups lie flat in the monolayer regime for the adsorption of 2H-TPP on Ag(111) after iron metalation, suggesting the influence of the electronic interaction with substrate on the phenyl group orientation.[30]

The observation that phenyl groups do not lie flat on Gr/Ni(111) and Gr/Pt(111) for ~1ML further highlights the influence of graphene on the interaction with adsorbed molecule. In the gas phase phenyl groups are almost orthogonal to the macrocycle in order to minimize the steric hindrance with the hydrogen atoms of macrocyle. [30] Considering large dichroism shown by phenyl group peak for FeTPP-Cl on HOPG, it can be inferred that phenyl groups are nearly orthogonal to the substrate as expected due to the weaker interaction with HOPG. Thus, intramolecular conformations of FeTPP-Cl seems to be influenced by the specific surface properties of the substrates.
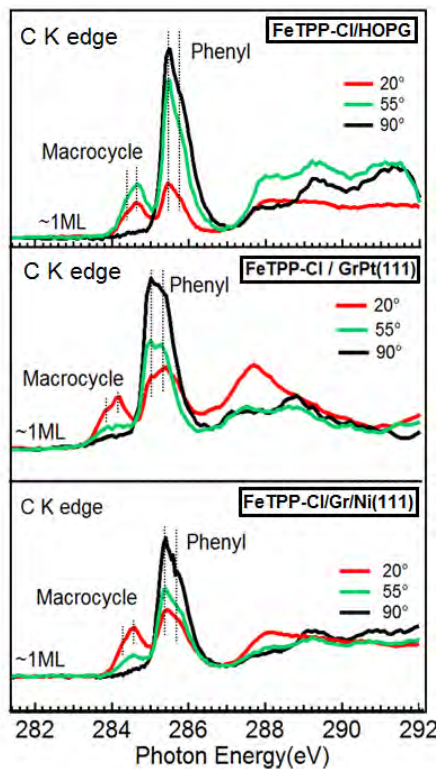

Figure 19 C-K edge NEXAFS for the deposition of FeTPP-Cl on Gr/Ni(111), Gr/Pt(111) and HOPG

In conclusion the FeTPP-Cl deposition on the three substrate preset notably differences between epitaxial Gr/Ni(111) and HOPG. The Gr/Pt(111) present an intermediate framework. We interpret these finding as due to π substrate orbitals and the Gr-metal separation. Notably the presence of an interface state at 0.3 eV below the EF measured in Gr/Ni(111) suggest the possibility of the gap opening previewed by the recent theoretical calculations [17], though the simulation is referred to a free-standing graphene layer. Notably the interface state is absent in the case of Gr/Pt(111) case. Further work is mandatory to confirm this point.

5.4 Electronic properties of Ferrocene/Graphene interface on ferromagnetic surface and pyrolytic graphite

Ferrocene (FeCp$_2$, table-1, Chapter-1) exhibits typical sandwich structure where two cylopentadienyl (Cp) rings lie above and below an iron ion with +2 oxidation state. Ferrocene have diverse applications as high-temperature lubricants, dopants to stabilize organics and polymers against UV degradation, photopolymerization catalysts etc. In recent years, considerable attention has been given to exploiting the potential of FeCp$_2$ molecular TFs for spintronic applications. Due to strong correlation between electronic and magnetic properties of organic molecules, we investigate the electronic structure of the FeCp$_2$interfaces with carbon based materials, graphene on ferromagnetic Ni(111) substrate and HOPG.

Among the motivation exposed previously (chapter-1) we aim at the study of the pertubation of the oxidation state of adsorbed ferrocene. Actually, magnetic and electronic properties of transition metal complexes adlayers on surfaces are strongly related to the oxidation state of the central metal atom. It motivates us to perform detailed characterization of electronic properties of Ferrocene/Graphene interface on ferromagnetic surface.

A variety of impactful applications has been explored for hybrid system composed of metallocene and carbon based materials ranging from biosensing, catalysis and spintronics.[33], including the metallocene interaction with carbon nanotubes[33], graphite[34], graphene[35], graphene nanoribbons [36] as well as graphene oxide.[37] Density functional theory calculations show that ferrocene adsorption on pristine graphene nanoribbons gives rise to perfect magnetoresistive effect. While for ferrocene adsorption on p-type graphene nanoribbons, the perfect magnetoresistive effect disappears but a high-efficiency spin-filtering effect can be observed.[36] Moreover, the electrical properties of CNTs can be altered by the intercalation of FeCp$_2$ or CoCp$_2$.[33] CNTs filled with iron, synthesized by the decomposition of ferrocene intercalation into CNTs have found applications in the biosensing.[33] Intercalation of ferrocene into layered carbon hosts such as graphene oxide (GO) or reduced graphene oxide (RGO) has been investigated, [37] demonstrating that the intercalated ferrocene compound presents an improved thermal stability due to the confinement effect arising from the π-conjugation system in the composite.

Importantly, such immobilization of organometallic compounds in a host material have shown potential to act as catalytic centers for heterogeneous catalytic reactions. Ferrocene adsorption on metallic substrates such as Ag(100), Cu(111) and Cu(100) has been investigated [38, 39]. It has been observed that ferrocene interacts weakly with Ag(100), dissociating under electron beam leading to strongly interacting iron containing species. STM study for the adsorption on Ferrocene on Cu(111) and Cu(100) shows that $FeCp_2$ adopts two-dimensional molecular arrangement having vertical as well as horizontal orientations. DFT calculations shows that a non covalent T shaped interaction is necessary for that stability of physisorbed molecular layer.[38] High resolution electron energy loss spectroscopy (HREELS) analysis reveals that ferrocene is stable on HOPG at 140 K and interacts weakly.[40] In addition, ferrocene has been utilized to form small metallic iron clusters on HOPG by depositing ferrocene on HOPG at temperatures above 1200K. In addition to layer carbon materials ferrocene has been found to intercalate into layered dichalcogenide material. Spectroscopic results confirm ferrocene intercalation and change of iron ion oxidation state due to charge transfer from $TiSe_2$ to ferrocene.[41]

Although, ferrocene adsorption has been investigated on metallic substrates, a photoemission and X-ray absorption based study for ferrocene adlayers on transition metallic substrate such as Ni(111) passivated by graphene is still lacking. In this paragraph, we employed photoemission and XAS to investigate the interfacial electronic properties of $FeCp_2$ interfaces with Gr/Ni(111) and HOPG. The study aims to provide insights into the strength of interaction and alterations in the oxidation state of iron due self assembly at well below desorption temperatures and at room temperature (RT). In order to achieve this objective, $FeCp_2$ multilayer was deposited on Gr/Ni(111) at about 200K and desorbed at RT . A coverage of ~1ML on Gr/Ni(111) was achieved by desorbing $FeCp_2$ multilayer at about 250K.

In order to depict the interaction of $FeCp_2$ /HOPG system, ~1ML $FeCp_2$ coverage on HOPG was achieved at about 250 K (labeled as 1ML at LT) and subsequently annealed at RT labeled as (desorbed at RT). Corresponding PES and NEXAFS measurements were performed at these coverages. Photoemission and XAS results indicates that oxidation state of iron ion does not change on Gr/Ni(111) and HOPG. Moreover, Fe $L_{2,3}$, C-K edge and valence band analysis strongly suggest that $FeCp_2$ molecules do not desorbs at room temperature on HOPG in contrast to Gr/Ni(111).

5.4.1 Valence Band Analysis

Figure 20 (a) shows the valence band PES spectra of $FeCp_2$ deposited on Gr/Ni(111) and HOPG in the monolayer regime, as obtained either after annealing a multilayer film at LT= 250K, and after annealing at RT. The presence of molecular induced peaks on Gr/Ni(111) at LT is followed by their disappearing after annealing at RT.

The multilayer of $FeCp_2$ on Gr/Ni(111) performed at 155eV and 400eV photon energies lead to the suppression of the Ni 3d peak intensity, as expected, and to prominent photoemission

features at approximately 2.3 eV, 4.4 eV, 7.9 eV, 12.3 eV and 17.2 eV with respect to the Fermi level (Figure12(b)). The assignments of various features are summarized in Table-3, [44]. There is general trend of lower intensity of all features for the spectra taken at hv=at 400 eV due to the decreased C 2p and Fe 3d cross sections in comparison with hv=155eV.

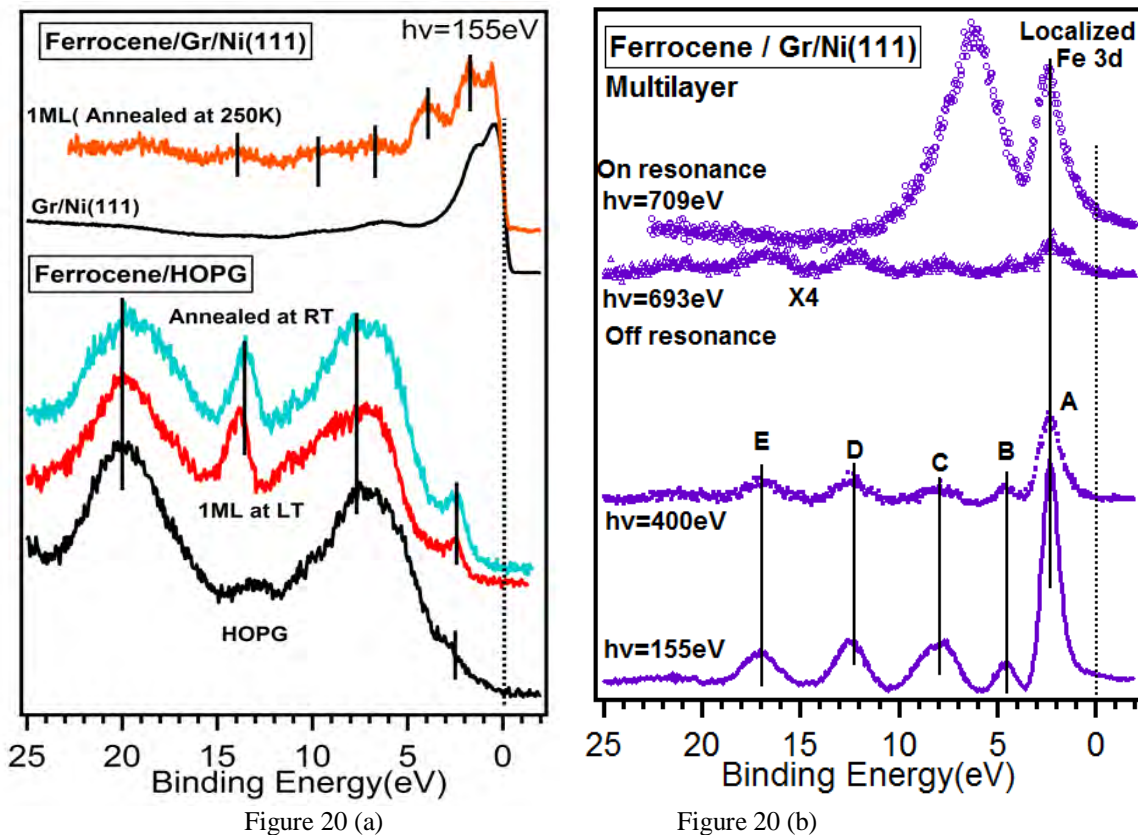Figure 20 (a)   Figure 20 (b)

Figure 20(a) Valence band photoemission spectra for the deposition of Ferrocene on Gr/Ni(111) and HOPG for two cases of 1 ML, as obtained by annealing of a FeCp$_2$ multilayer at the indicated RT and LT=250 K ;(b) Valence band spectra for the deposition of Ferrocene multilayer taken at different photon energies. (see text for labels)

The MOs $6a_{2u}$, $3e_{2u}$, $3e_{2g}$, $3e_{1g}$, $5e_{1u}$ and $7a_{1g}$ contribute to the feature at 7.9 eV, while $5a_{2u}$, $6a_{1g}$, $2e_{2u}$, $2e_{1g}$ MOs lead to the peak at 12.3eV, while the peak E at 17.2eV has C 2s origin [44]. Theoretical calculations show that the $4e_{1g}$ $7a_{1g}$ $6e_{1u}$ and $6a_{2u}$ MOs are associated with the hybridization of cyclopentadienyl orbitals π-Cp with Fe 3d states. The $8a_{1g}$ and $4e_{2g}$ MOs are associated with localized Fe 3d orbitals. As shown in Figure 20(b) the features at 2.3eV is prominent at resonance (hv=709eV) as compared to 'off resonance' (hv=693.2eV) confirming the contribution from iron metal atom associated orbitals to these MOs. There is a good similarity of the above photoemission features with the FeCp$_2$ adsorbed on Mo(112)[38, 43] where FeCp$_2$is reported to be weakly interacting with Mo(112) as compared to Ag(100) and Cu(100). MOs at 4.4eV and 7.9eV are associated with hybridization of Fe 3d and C2p of cyclopentadienyl ring. The valence band spectrum at 7.9eV shows a broader feature with

116

maxima at 6.2eV and can be associated to the 'on resonance' contribution from MOs at 4.4eV and 7.9eV due hybridized Fe 3d orbitals.

Valence band Peak assignments Fe(Cp)$_2$	Binding energy	Molecular orbitals [43]
Peak A	2.3eV	$8a_{1g}$ and $4e_{2g}$
Peak B	4.4eV	$6e_{1u}$ and $4e_{1g}$
Peak C	7.9eV	$6a_{2u}$, $3e_{2u}$, $3e_{2g}$, $3e_{1g}$, $5e_{1u}$ and $7a_{1g}$
Peak D	12.3eV	$5a_{2u}$, $6a_{1g}$, $2e_{2u}$, $2e_{1g}$
Peak E	17.2eV	C 2s

Table.3 Assignments of FeCp$_2$ Molecular Orbitals [44]

The MOs features in 1ML regime appear shifted and broader as compared to the multilayer case, due to molecule-substrate interactions, though, MOs of FeCp$_2$ appear less pronounced on HOPG as shown in Figure 20(a). The FeCp$_2$ MOs shifts in case of Gr/Ni(111) substrate are about 0.7eV with respect to the 1 ML on HOPG.

Valence Band of HOPG (Fig. 20a) is primarily dominated by peaks at 7.2eV and 20eV corresponding to HOPG orbitals with π and σ character respectively. Importantly, the peak at about 13 eV is present for the 1ML at low temperature (LT,), remaining persistent at RT. There are significant electronic and geometric structure differences in the HOPG basal and step edges planes. [13] The presence of this peak can be assigned to the C 2s valence emission from sp^3 hybridized carbon species.[44]

5.4.2 NEXAFS and XPS Analysis

Figure 21 shows the Fe L$_{2,3}$ edge spectra for the deposition of ferrocene on Gr/Ni(111) and HOPG for the 1ML LT and RT and the multilayer regime. The spectral line shape is in agreement with gas phase Fe L$_{2,3}$ edge spectrum, with two peaks in the region between 705eV and 715eV corresponding to transitions from Fe 2p$_{3/2}$ levels into $4e_{1g}$(-like) Fe 3d unoccupied orbitals and $3e_{2u}$(-like), Cp π*[46]. The features between 718eV to 726V are assigned to transitions from Fe 2p$_{1/2}$ levels. In order to eliminate the intensity variations effects due to light polarization and to highlight the alteration in the spectral features due to charge transfer and/or interaction with underlying substrate we have analyzed the spectrum at 55° (magic angle).

As shown in Figure 21 the line shape of $FeCp_2$ multilayer Fe $L_{2,3}$ XAS spectrum on Gr/Ni(111) exhibits good resemblance with ~1ML coverage spectrum obtained by desorbing multilayer at 250 K and confirms the Fe +2 oxidation state [46]. It suggests that ferrocene interacts weakly with Gr/Ni(111) with no significant charge transfer between the Fe central metal atom and the underlying substrate. As shown in Figure 21, desorption of $FeCp_2$ multilayer at RT results in an almost complete suppression of Fe $L_{2,3}$ signal confirming the weak molecule-substrate interactions.

The analysis of Fe $L_{2,3}$ XAS spectrum for the adsorption of $FeCp_2$ on HOPG reveals that the $4e_{1g}$ Fe 3d feature at about 710eV is weaker for ~1ML at RT as compared to ~1ML coverage obtained by depositing $FeCp_2$ on HOPG at about 250K (labeled ~1ML at LT). It indicates that $FeCp_2$ does not desorb from HOPG at RT in contrast to Gr/Ni(111).

Further insights on the interaction of Ferrocene with Gr/Ni(111), are provided by the C K edge NEXAFS at photon incidence angles of 20°, 55° and 90° as shown in Figure 22. The Gr/Ni(111) C K edge as discussed in 6.1, is primarily dominated by two main peaks at 285.5V and 287.1eV. Theoretical calculations [49] indicate that the peak at 285.5eV originates by transitions from C1s to interface state above Fermi level due to Cp_z-Ni 3d hybridization. The other peak at 287.1eV is due to the dipole transition of the photoemitted electron from the C1s core level to the interface state above the Fermi level formed by the hybridization of from Cp_z-Ni p_x,p_y,3d orbitals. These peaks are very close in energy to the C K edge peaks of ferrocene at 285.7eV and 287.21 eV.
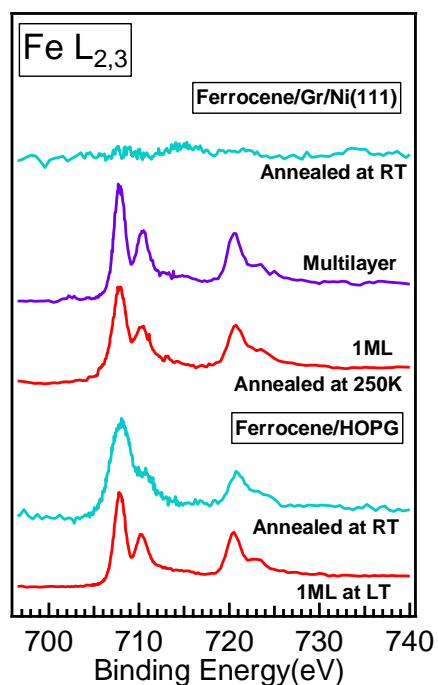

Figure21 Fe L edge NEXAFS spectra for the deposition of Ferrocene on Gr/Ni(111) and HOPG in the monolayer and multilayer regime CHECK THE LABELS; COHERENTLY WITH PREVIOUS FIGURES

Theoretical calculations on Ferrocene show that peak at 285.7eV originates due to transition to degenerate MOs formed by the overlap of ligand π^* orbitals hybridized with Fe $3d_{xz}$ (LUMO) or $3d_{yz}$ (LUMO+1) atomic orbitals. The second peak at 287.21eV corresponds to π^* orbital that is strongly localized on the Cp ring containing the excited carbon atom.[50] As shown in Figure 22 C Kedge peaks corresponding to Gr/Ni(111) exhibits strong dichroism as compared to FeCp$_2$ related peaks. At Normal incidence the intensities of C K edge peaks of FeCp$_2$ at 285.7eV and 287.21 eV do not vanish suggesting that FeCp$_2$ molecules do not adopt completely flat orientation on Gr/Ni(111). Notably, Ferrocene NEXAFS C K edge peaks does not present significant dichroism as shown in Figure 23 indicating that there is no preferred orientation of Ferrocene on Gr/Ni(111).
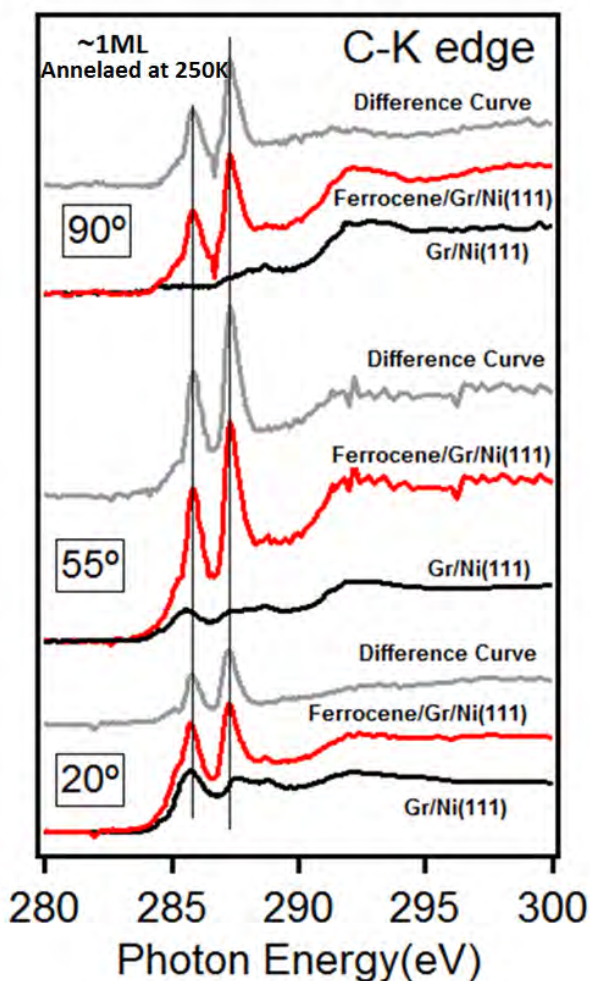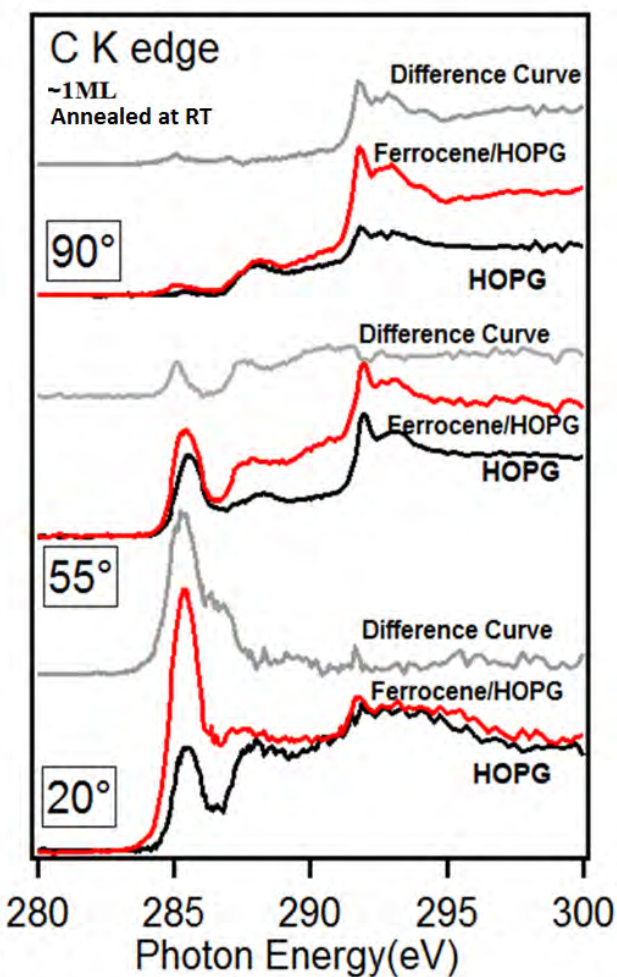

Figure 22

Figure 23

Figure 22 C K edge NEXAFS spectra for the deposition of Ferrocene on Gr/Ni(111) in the monolayer regime and Figure 23 shows C K edge NEXAFS spectra for Ferrocene monolayer at room temperature on HOPG(See text for labels)

119

This observation appears to be in good agreement with STM investigation of Ferrocene /Cu(111) system, where the STM study indicates that FeCp$_2$ adopts vertical as well as horizontal orientations on Cu(111) and T shaped interactions among molecules [38]. Moreover, there are no significant changes in the spectral line shape indicating that bonding environment of FeCp$_2$ carbon atoms does not change significantly. In order to minimize substrate influence and to highlight ferrocene C K edge related features difference curves are investigated as shown in Figure 22 and presents no notable difference in the spectral line shape and photon energy position indicating that FeCp$_2$ interacts weakly with Gr/Ni(111).

XPS C1s spectrum for the FeCp$_2$ multilayer at about 285eV binding energy is in good agreement with ferrocene multilayer on Ag(100).[54] It has been observed that ferrocene exhibits a layer by layer growth on metallic substrates. Moreover, no significant binding energy shifts have been observed with ferrocene growth on Ag(100) suggesting a weaker interaction with underlying substrate. Due to proximity of C1s binding energy of Gr/Ni(111) at 284.8eV with the ferrocene core level, these peaks are indistinguishable in monolayer regime within our experimental set up as shown in Figure 24. These results appear to compliment our Fe L$_{2,3}$ edge and C K edge observations that ferrocene interacts weakly with Gr/Ni(111).
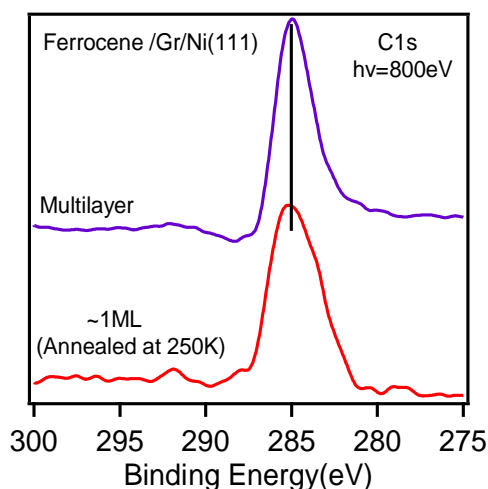
Figure 24 C1s XPS for the deposition of Ferrocene on Gr/Ni(111)

We analyzed C K edge spectrum for FeCp$_2$ ~1ML adlayer on HOPG desorbed at RT as shown in Figure 23. These spectra are compared with C K edge of pristine HOPG (discussed in 6.1) and difference curves have been made, so that information about Ferrocene interaction can be revealed. The ferrocene features in case of 1ML RT/HOPG result slightly in different energies and broadened.

The 3D interlayer states also indicate deviation from ideal 2D layered structure for HOPG. C K edge spectrum at 55°(magic angle) exhibits higher intensity corresponding to features related to interlayer states between 286ev to 290eV as shown in Figure 23.

Figure 25 C1s XPS for the deposition of FeCp$_2$ on HOPG (see text for labels)

Finally, we analyzed the XPS C1s for the deposition of Ferrocene on HOPG as shown in Figure 25. ~1ML of ferrocene deposited at about 250K (labeled as ~1ML at LT) exhibits a shoulder at 285eV corresponding to Ferrocene in addition to peak 284.4eV related to the strong contribution from HOPG C1s. When Ferrocene was allowed to desorb at RT, the shoulder at 285eV binding energy persists with an increased tail at higher binding energies indicating that ferrocene desorption is not prominent fo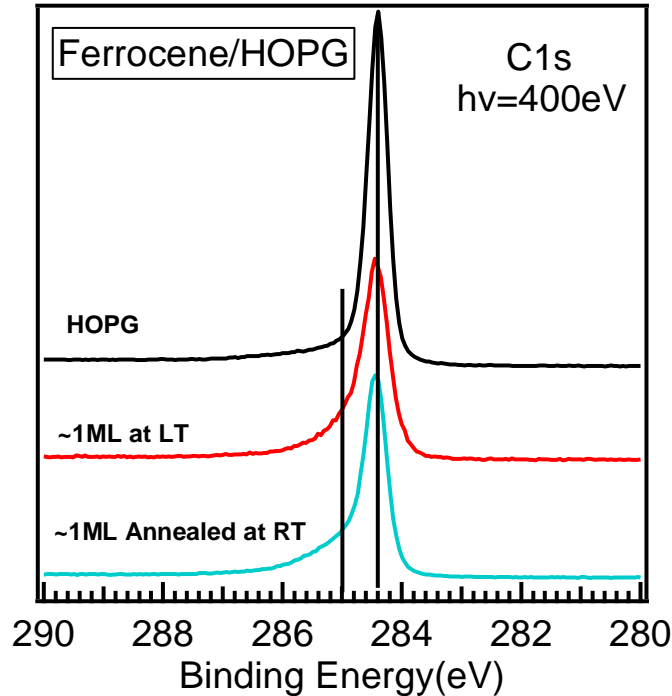r FeCp$_2$/HOPG system in contrast to FeCp$_2$/Gr/Ni(111) system. This inference compliments the Fe L edge observation that FeCp$_2$ desorption is not significant on HOPG. Therefore, our study highlights differences in the interaction of FeCp$_2$ on HOPG and Gr/Ni(111) and establishes that iron ion oxidation state does not change for both systems.

Summarizing, there is an evident change of Fe $L_{2,3}$ line shape similar to a fractional oxidation state intermediate between +2 and +3 in case of intercalation of ferrocene on TaSe$_2$ [41] related to charge transfer. This is in contrast to 1ML at LT FeCp$_2$ adsorption on HOPG and Gr/Ni(111). It provides an evidence that for HOPG and Gr/Ni(111) iron does not change oxidation state and FeCp$_2$is physisorbed. This result, together with the broadening of the C K edge, C1s core level and VB features indicates that residual ferrocene molecules at RT remains trapped on the HOPG surface. This phenomenon can be ascribed to a π–π interaction between sp^2 hybridized Carbon atoms of HOPG surface and FeCp$_2$. The sp^3 hybridized carbon species revealed in VB (Figure 20) can arise from defects in the sp^2 hybridized layered HOPG structure. The presence of such types of defects in the otherwise sp^2 hybridized carbon in graphite has been proposed to exist in

121

thermally reduced graphite oxide samples. [45] The peak at about 13eV in the valence band due to sp³ hybridized carbon species has also been observed for graphene-based transparent and conductive thin films fabricated by thermal reduction of graphite oxide, which exhibits very similar electronic and structural properties as highly oriented pyrolytic graphite.[44]

Among carbon based materials HOPG is peculiar due to its layered structure with interlayer distance of about 0.35nm. In general, HOPG surface is prepared by peeling off top layers of HOPG by adhesive scotch tap which induces external step edges in addition to internal step edges. Figure 26(a) shows the topographic STM image of HOPG clearly demonstrating internal and external step edges. It has been observed that external step have higher work function and chemical reactivity than internal step edges.[43]
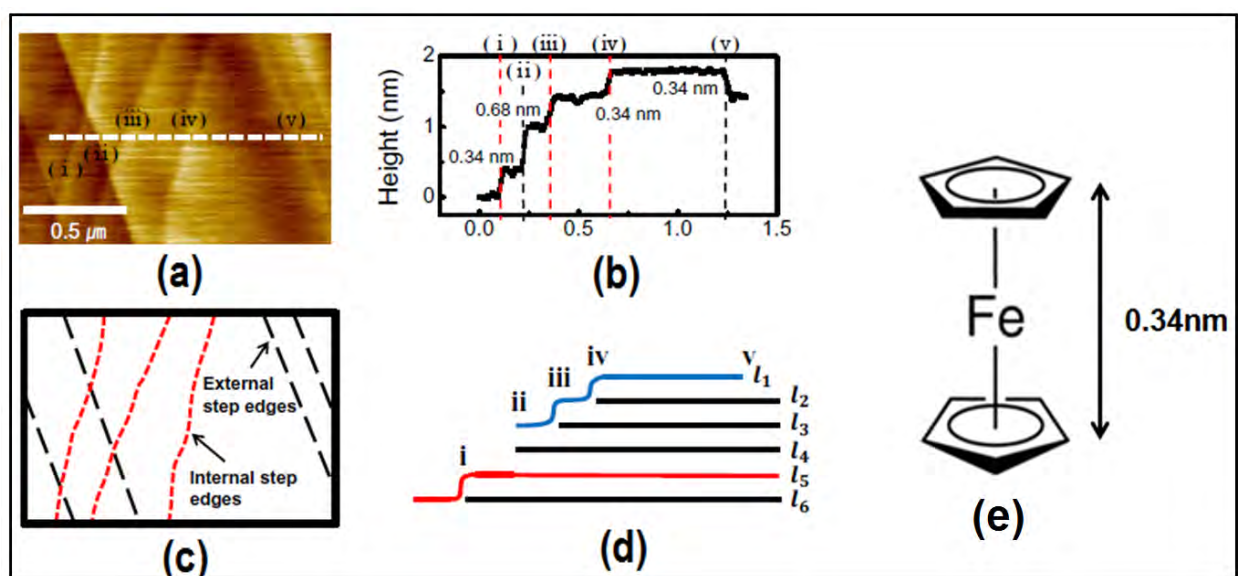

Figure.26(a) Topogrphy of HOPG(b) Line profile along the white dashd line for the step edges heights Labels (i) to (v) are used to represent the step edges of graphite marked in (a).(c) schematic representation of HOPG internal and external step edges of (a). (d) Schematic diagram showing a cross section along the horizontal dashed line in (a) and (b). The highest (l_1) and lowest (l_5) layers are indicated by the blue and red lines that cross over the subsurface layers (l_2– l_4 and l_6), respectively. Steps i, iii, and iv are internal step edges under the top single graphene layer. (e) Structure of Ferrocene. Reproduced from Park and Salmeron [43]

As shown in Figure 26 line profile in the HOPG topographic image shows that the height of these step edges is 0.34 nm for single atomic layer. The situation becomes interesting when ferrocene is adsorbed on the HOPG surfaces as the size of ferrocene is also 0.34 nm comparable to the step edges on HOPG surface. Due to the diffusion of ferrocene molecules on HOPG surface, there is a finite probability that ferrocene get trapped by the captive environment provided by HOPG interlayers facilitated by step edges. However, a detailed STM study can shed more light on this issue. Intercalation of $FeCp_2$ on layered carbon materials (graphene oxide and reduced graphene oxide) has been reported [37] and on layered $TiSe_2$ [41]. surface.

122

Summarizing, the results on RT for Ferrocene/HOPG system, the C 1s core level, the Fe $L_{2,3}$ edges and the VB data show a persistence of the molecule and a broadening of the molecular features. On the other hand Fe L edge, C K edge and valence band of Ferrocene/Gr/Ni(111) system strongly suggest that though, ferrocene molecules do not change oxidation state similar to HOPG but at RT there is almost complete desorption on Gr/Ni(111). These finding strongly suggest notable difference in the surface properties of Gr/Ni(111) and HOPG.

References

[1] R. Addou, A. Dahal, P. Sutter, and M. Batzill, Appl. Phys. Lett. 100, 2012, 021601.

[2] T. G. Gopakumar, H. Tang, J. Morillo, R. Berndt, J. Am. Chem. Soc. 134, 2012, 11844−11847.

[3] M.-S. Liao and S. Scheiner J. Chem. Phys., 117, 2002, 205.

[4] G. Bussetti, A. Calloni, R. Yivlialin, A. Picone, F. Bottegoni and M. F. Beilstein J. Nanotechnol. 7, 2016, 1527–1531.

[5] K.Comanici, F.Buchner, K.Flechtner, T.Lukasczyk, J.M.Gottfried, H.P. Steinrück,H.Marbach, Langmuir, 24, 2008, 1897–1901.

[6] J.M. Gottfried, Surface Science Reports, 70, 2015, 259–379.

[7] L. Massimi, S. Lisi, D. Pacilè, C. Mariani, M. G. Betti1 Beilstein J. Nanotechnol, 5, 2014, 308–312.

[8] W. Auwärter, D. Écija, F. Klappenberger, Johannes V. Barth, Nature Chemistry volume7, 2015,105–120.

[9]   J. P. Beggan, S. A. Krasnikov, N. N. Sergeeva, M. O. Senge, A. A. Cafolla, Nanotechnology 23, 2012 235606.

[10] .H. C. Herper, M. Bernien, S. Bhandary, C. F. Hermanns, A. Kr¨uger, J. Miguel, C. Weis, C. Schmitz-Antoniak, B. Krumme, D. Bovenschen, C. Tieg, B. Sanyal, E. Weschke, C. Czekelius, W. Kuch, H. Wende,   O. Eriksson,   Physical Review B 87, 2013, 174425.

[11]   D. van , M. Lange, J. Schaffert, Maren C. Cottin, M. Schmuck, R. Robles,H. Wende, C. A. Bobisch, Rolf Mçller ChemPhysChem, 14, 2013, 3472 – 3475.

[12] T. G. Gopakumar, H. Tang, Joseph Morillo, Richard Berndt, J. Am. Chem. Soc. 134, 2012, 11844−11847.

[13] Maria Bassiouk, Edgar Álvarez-Zauco, and Vladimir A., Journal of Computational and Theoretical Nanoscience 9,2012, 532–540.

[14] Patera, L. L. et al. ACS Nano 7,2013, 7901–7912.

[15] A. Dahal, M. Batzill, Nanoscale, 6, 2014, 2548-2562.

[16] D. Nobis et.al., Physical Review B 88, 2013, 195435.

[17] C. Rubio-Verdú, A. Sarasola, D. Sánchez-Portal & Jose Ignacio Pascual Communications Physics 1, 2018, 15.

[18] S. Rangan, S. Katalinic, R. Thorpe, and E. Galoppini, J. Phys. Chem. C, 114, 2010,1147.

[19] P. Palmgren, T. Angot, C.I. Nlebedim, J.M. Layet, G. Le Lay, M. Göthelid, J. Chem. Phys. 128, 2008, 064702.

[20] H. K. Jeong, C. Yang, EPL, 92, 2010, 37005.

[21] Ashish Bhattarai, Kevin Marchbanks-Owens, Ursula Mazur, and K. W. Hipps J. Phys. Chem. C 120, 2016, 18140−18150.

[22] . M.Gao, Applied Physics Letters **98**, 20111, 033101.

[23] J.M. Gottfried, Science Reports, 70, 2015, 259–379.

[24] Isvoranu, C.; Wang, B.; Ataman, E.; Knudsen, J.; Schulte, K.; Andersen, J. N.; Bocquet, M.-L.; Schnadt, J., J. Phys. Chem. C 2011, 115, 24718−24727.

[25] Schmid, M.; Zirzlmeier, J.; Steinrück, H.-P.; Gottfried, J. M. J. Phys. Chem. C 2011, 115, 17028−17035.

[26] Scardamaglia, M.; Forte, G.; Lizzit, S.; Baraldi, A.; Lacovig, P.; Larciprete, R.; Mariani, C.; Betti, M. G.. J. Nanopart. Res. 2011, 13, 6013−6020.

[27] S. Müllegger, M. Rashidi, T. Lengauer, E. Rauls, W.G. Schmidt, G. Knör, W. Schöfberger, and R. Koch, Physical Review B 83, 20111, 165416.

[28] 1. Chylarecka, D.; Wäckerlin, C.; Kim, T. K.; Müller, K.; Nolting, F.; Kleibert, A.; Ballav, N.; Jung, T. A. J. Phys. Chem. Lett. 2010, 1, 1408.

[29] T. A. Jung et al. J. Phys. Chem. C 2011, 115, 1295–1301.

[30]   C.Castellarin-Cudia,P.Borghetti,G.DiSanto,M.Fanetti, R. Larciprete,C.Cepek,P.Vilmercati, L.Sangaletti, A.Verdini, A. Cossaro,L. Floreano,A.Morgante,A.Goldoni,ChemPhysChem 11, 2010, 2248–2255.

[31] 18. Marius Toader, Pavel Shukrynau, Martin Knupfer, Dietrich R. T. Zahn, and Michael Hietschold, Langmuir, 28, 2012, 13325−13330.

[32] 21.Auwarter, W. Seufert, K. Klappenberger, F. Reichert, J. Weber-Bargioni, A. Verdini, A.; Cvetko, M. Floreano, L.Cossaro, A, Phys. Rev. B: Condens. Matter Mater. Phys. 2010, 81, 245403−245403.

[33] M. Sauer, H. Shiozawa, P. Ayala, H. Kataura, K. Yanagi, S. Krause, and T. Pichler, Phys. Status Solidi B 12, 2012, 2408–2411.

[34] K. Svensson, T.R. Bedson, R.E. Palmer, Surface Science 451, 2000, 250–254.

[35] S.Marocchi, P. Ferriani, N. M Caffrey, F. Manghi, S.Heinze, V. Bellini, Physical Review B.2018, 88, 14.

[36] J. Zeng, et.al. Carbon 98, 2016, 607-612.

[37] Y. Gao, G. Hu, W. Zhang, D. Ma and X. Baob, Dalton Trans. 2011, 40, 4542.

[38] Maider Ormaza, J. Phys. Chem. Lett. 6,2015, 395−400.

[39] Dulip Welipitiya, A. Green, J. P. Woods, and P. A. Dowben, J. Appl. Phys. 79, 1996,14-16.

[40] K. Svensson, T.R. Bedson, R.E. Palmer, Surface Science 451, 2000, 250–254.

[41] A.N. Titov, Chemical physics letters, 497, 2010, 187-190.

[42] G. Avvisati, P. Gargiani, P. Mondelli, F. Presel, A. Baraldi, and M. G. Betti, Phys. Rev. B 2018, 98, 115412.

[43] H. Lee, H-Bo-R. Lee. S. Kwon, M. Salmeron,and J.Y. Park, ACS Nano, 9, 3814-3819.

[44] P.A. Dowben, Chemical Physics Letters, 283, 1998. 44–50.

[45] A. Vollmer, X.L. Feng, X.Wang, L.J. Zhi, K. Müllen, Appl Phys A 94, 2009, 1–4.

[46] K.N. Kudin, B. Ozbas, H.C. Schniepp, R.K. Prud'homme, I.A. Aksay, R. Car, Nano Lett. **8**, 2008, 36.

[47] K. Godehusen,T. Richter, P. Zimmermann, P. Wernet, , J. Phys. Chem. A 2017, 121, 66−72.

[48] W. E. Britton. J.Electroanal. Chem., 178, 1984, 153-163.

[49] S. Böttcher, M. Weser, Y. S. Dedkov, K. Horn, E. N Voloshina, B. Paulus, Nanoscale Research Letters 6, 2011, 214.

125

[50] E. Otero, R. G. Wilks, T. Regier, R. I. R. Blyth, A. Moewes, J. Phys. Chem. A 2008, 112, 624-634.

[51] Christopher Ehlert, W. E. S. Unger and P. Saalfrank, Phys. Chem. Chem. Phys., 2014, 16, 14083—14095

[52] O. Romanyuk, M. Varga, S. Tulic, Izak, P. Jiricek, A. Kromka, V. Skakalova, and B. Rezek, J. Phys. Chem. C 2018, 122, 6629−6636.

[53] J. Dıaz, G. Paolicelli, S. Ferrer, and F. Comin Physical Review B, 54, 2011, 8064-8069.

[54] M. A. Langell et.al. J. Phys. Chem. B, 14, 2000, 3085-3095.

[55] J. Touzeau, F. Barbault, F. Maurel, M. Seydou Chemical Physics Letters 714, 2018, 172–179.

[56] L. L. Patera, C. Africh, R. S. Weatherup, R. Blume, S. Bhardwaj, C. Castellarin-Cudia, A. Knop-Gericke, R. Schloegl, G. Comelli, S. Hofmann, and C. Cepek, ACSNano, 7, 7901–7912 ' 2013.

[57] Y.S.Dedkov, et.al. Fonin, M. New J. Phys. 2010, 12, 125004.

[58] A. Varykhalov et.al. Phys. Rev. X 2012, 2, 041017.

[59] 25. D. Nobis et.al. Physical Review B 88, 2013, 195435.

[60] M. Gao, Y. Pan; L. Huang; H. Hu; L. Z. Zhang; H. M. Guo; S. X. Du; H.-J. Gao Applied Physics Letters **98**, 2011, 033101.

[61] Christopher Ehlert , et. al. Phys. Chem. Chem. Phys., 2014, 16, 14083-14095.

[62] S.Berner,M.Brunner,L.Ramoino,H.Suzuki,H.J.Güntherodt,T. A. Jung,Chem.Phys.Lett.348(2001)175–181.

[63] S.Berner,M.deWild,L.Ramoino,S.Ivan,A.Baratoff,H. J. Güntherodt,H.Suzuki,D.Schlettwein,T.A.Jung,Phys.Rev.B68 (2003) 115410.

[64] J.C.Buchholz,G.A.Somorjai,J.Chem.Phys.66(1977)573–580.

[65] J.K.Gimzewski,E.Stoll,R.R.Schlittler,Surf.Sci.181(1987)267–277.

[66] W.Auwärter,D.Ecija,F.Klappenberger,J.V.Barth,Nat.Chem.7 (2015) 105–120.

[67] S.Mohnani,D.Bonifazi,Coord.Chem.Rev.254(2010)2342–2362.

[68] S.Yoshimoto,S.Yasunishi,T.Kawamoto,J.Phys.Chem.C118 (2014) 29880–29886.

[69] Y.Wang,K.Wu,J.Kröger,R.Berndt,AIPAdvances2(2012)041402.

[70] T.Niu,A.Li,J.Phys.Chem.Lett.4(2013)4095–4102.

[71] T.Komeda,H.Isshiki,J.Liu,K.Katoh,M.Yamashita,ACSNano8 (2014) 4866–4875.

[72] L.Vitali,S.Fabris,A.M.Conte,S.Brink,M.Ruben,S.Baroni, K. Kern,NanoLett.8(2008)3364–3368.

Chapter -6

Conclusion and Outlook

The nanoscale material science of tetrapyrrole transition metal complexes, as porphyrin, phthalocyanine and related complexes, is an active area of research due to enormous variation in the reactivity, electronic and magnetic properties depending on the type of the central metal atom and molecular structure. The driving force to explore the surface science of these conjugated molecules is due to their relevance in both fundamental sciences as well as in technological applications. In particular, a thorough understanding of metal-molecule interfaces is highly desirable to utilize these molecules for functional molecular devices. Interaction with the substrate can result in substantial conformational changes, especially if the porphyrins carry large substituent, such as phenyl rings in the meso-positions. The complexity of these systems induces the use of a multi-technique approach based on electronic and absorption spectroscopies and structural diffraction techniques. Inverse photoemission spectroscopy has been utilized to highlight the influence of intermolecular interactions on unoccupied density of states, as empty orbitals are more sensitive to the intermolecular interaction due to their higher delocalization around the macrocycle.

There have been considerable efforts in analyzing interfacial electronic properties and molecular structure adopted by organic conjugated molecules on inorganic substrates utilizing techniques such as scanning tunneling microscopy, photoemission and X-ray absorption etc. However, there are certain gaps in the detailed knowledge of porphyrin and phthalocyanine molecular TFs as far as unoccupied density of states investigations based on IPES are concerned. The present thesis is an attempt to address this issue. Another important issue in molecular opto-electronics is to establish relation between structure and properties of molecular thin films and develop a generalized framework for the dependence of properties on molecular structure adopted by molecules.

The thesis aims to add to the existing knowledge related to metal-molecular interfaces and establish relationship between molecular structure of thin films and their vibrational and electronic properties. We have specifically selected certain metal-molecule systems to serve this purpose. It has been established that nature of substrate and its treatment significantly impact molecular order and polymorphism adopted by molecular thin films, thereby influencing their vibrational and electronic properties. Inverse photoemission has been extensively utilized to study the unoccupied density of states for phthalocyanine and prophyrin molecular thin films in order to obtain hints on a coherence picture of unoccupied molecular states together with valence band states.

The research activity involves the characterization and analysis of perturbations induced by the interaction of stiff phthalocyanine molecules with conducting substrate as compared to more

plastic porphyrin molecules with different peripheral groups. The motivation is to rationalize the impact of the different factors which influence energy level alignment at interface, such as molecular conformations, electrostatic effects, polarizability, interface dipole, symmetry of substrate, charge transfer and chemical interaction etc. As the structural and chemical properties of molecular monolayer on substrates strongly influence multilayer growth, it is crucial to characterize organic-inorganic interfaces in monolayer regime. Therefore, we have devoted our study to characterize the interfacial electronic properties of tetrapyrrole transition metal complexes interfaces with conducting substrates focusing on the molecule-substrate interactions for different interaction strength. Overall the high resolution of our IPES instrument provides us unprecedented details of the unoccupied states for octaethyl porphyrin, tetraphenyl porphyrin and phthalocyanine TFs that were unseen in previous investigations. These results open further future characterization.

We establish that the interaction of more flexible porphyrin molecules with peripheral groups with underlying substrate is notably different as compared to more rigid phthalocyanine molecules. We have observed that structural perturbations of the molecular conformers in the molecular layers and substrate symmetry lead to the alterations in the opto-electronic properties and energy level alignment of the molecular orbitals.

In the following a summary of the specific achievements of this thesis is reported.

Third chapter has been devoted to provide fundamental understanding of MPc TFs unoccupied density of states corresponding to different central metal atom. DFT calculations provide basis for the sequence of unoccupied states for MPc, though, certain contradictions are observed in case of MPc ground state configurations. Soft X-ray absorption studies provide useful information about the nature of orbitals involved in the interaction process due to variation of x-ray absorption intensity related to the symmetry and the orientation of the molecular orbitals.

IPES measurements are preformed on about 8nm MPc TFs with the aim to investigate the contribution of unoccupied states. Overall high resolution of our IPES instrument enable us to clearly reveal unoccupied states and we have assigned the relevant peaks based on soft x-ray analysis of MPc TFs.

We have utilized IPES to investigate the unoccupied states involved in the interactions process by selecting CoPc/Au(110) and CuPc/Au(110) system. The purpose of selecting these systems is to unambiguously highlight the involvement of unoccupied states in interaction and charge transfer process at the interface due to difference in electronic configuration of 3d central metal atom. A depletion of density of states close to the Fermi level can be observed upon CoPc adsorption on the highly anisotropic Au(110) substrate, while CuPc levels slightly intermix with the underlying Au substrate. The out of plane Co 3d orbitals strongly hybridize, as deduced also by momentum-resolved inverse photoemission, and the contribution from molecular unoccupied density of states is enhanced. Importantly, XMCD studies reveal total quenching of CoPc

magnetic moment on Au(110) for low coverages, in contrast to CuPc, demonstrating the possibility of rehybridization of the CoPc frontier orbitals with the underlying Au states. A detailed comparison with the empty density of states obtained with the element selective X-Ray absorption enlightens and complements the IPES results and confirms the driving forces of the interaction process. We can thus provide a coherent picture of the interface electronic structure of CoPc and CuPc, induced by the different occupancy of 3d level of central metal atom, complementary to recent X-ray absorption studies.

Phthalocyanine TFs present pronounced polymorphism. Theoretically a strong perturbation of the electro-magnetic and vibrational properties is expected in the various polymorphs. α and β polymorphs of phthalocyanine differ in the interlayer distance of central metal atom thus can influence the magnetic coupling with the substrate and can impact vibrational properties of MPc TFs. As mention in the first chapter, the objective of the study is to correlate MPc TFs vibrational properties with molecular order and polymorphism. In order to achieve this , α phthalocyanine powders were synthesized from the commercial β powders in order to study their structural details with grazing incidence X-ray diffraction (GIXRD). About 50nm thin films of Iron phtathalocyanine (FePc) and Cobalt phtathalocyanine (CoPc) were deposited in Ultra High Vacuum (SIPE lab, TASC) on to technologically important substrates Si(111), ITO and polycrystalline gold. The structure of phtathalocyanine thin films and powders were studied using grazing incidence GIXRD at XRD-1 beamline at Elettera.

Raman spectroscopic analysis shows lower intensity for the frequencies corresponding to phthalocyanine macrocycle for the CoPc and FePc thin films grown on ITO as compared to SiO_x/Si due to the higher order of phthalocyanine molecules on SiO_x/Si. Atomic force microscopy displays a higher grain size for FePc and CoPc thin films on ITO as compared to SiO_x/Si and polycrystalline gold indicating towards the influence of molecule–substrate interactions on the molecular stacking. Grazing incidence X-ray diffraction(GIXD) reciprocal space maps analysis reveal that FePc and CoPc molecules adopt a combination of herringbone and brickstone arrangement on SiO_x/Si and polycrystalline gold substrate which can have significant implications on the optoelectronic properties of the films due to unique molecular stacking.

In continuation with our research activity to establish interconnection between structural and physical properties of transition metal complexes thin films, CoPc thin films of about 40nm thickness were deposited on Gr/SiOx and Au(111) substrates. Two systems are selected due to different registry of first CoPc monolayer on these substrates as revealed by STM studies. GIXRD reciprocal space maps show that CoPc molecules adopt predominantly herringbone and brickstone molecular arrangements, respectively. Analysis of reciprocal space maps establish that in case of CoPc deposition on Au(111) brickstone molecular phase is dominant as compared to the more common herringbone molecular arrangement. Co $L_{2,3}$ NEXAFS compliments these findings. Excited state dynamics studies indicate towards two decay channels. It is suggested

that the hybridization of central metal atom d orbitals with the π-orbitals of macrocycle provides extra decay channels or fast relaxation is also possible by charge transfer states. As herringbone and brickstone molecular arrangements (α-Phase) have notably distinct molecular arrangement , therefore , faster decay process involving Co atoms is expected to show notable differences for herringbone and brickstone molecular arrangements

Visible Pump-probe measurements performed with ultrafast laser to excite Q-band at FORTH research laboratory show notable differences in the hopping relaxation dynamics, related to the transport properties, of CoPc thin films on these substrates in the sub picoseconds and picoseconds timescales.

The objective of the fourth chaper is to investigate interfacial electronic properties of MOEP molecular TFs and to highlight the impact of different intermolecular interactions due to distinct central metal atoms. In order to surve the purpose, we selected NiOPE/Au(111) and CuOPE/Au(111) systems and inverstigated their unoccupied density of states with IPES.

Morevoer, in case of metal octaethyl porphyrin molecules ethyl groups can adopt different orientations in order to minimize steric hindrance and to obtain energetically stable configuration. We investigates the basic mechanisms in the ordering of single layers of metal Octaethylporphyrin molecules (MOEP) onto surfaces and the role played by the central atom in octaethylporphyrin molecules in their interaction with substrate and the effect on the molecular orbitals in the intermolecular interaction. We investigated the formation of the interface between the Au(111) single crystal surface and the MOEP, namely CuOEP (copper(II) octaethyl porphyrin) and NiOEP. These interfaces are taken as model systems of weak interaction. Au(111) presents a prototypical model substrate to understand weakly interacting metal-molecule interfaces and relevant in organic electronics due to its applications in optoelectronic devices. It has been observed that NiOEP molecules adopt two different structural phases in the monolayer regime while CuOEP exhibits single structural phase as confirmed by LEED investigation. IPES studies highlight the consequences on unoccupied density of states corresponding to different structural phases. A redistribution of the MO energies is measured and an important role of intermolecular interaction is proved, with a good agreement with DFT calculations. This achievement show that even in weak interaction organic-inorganic interface the effects on the electronic properties and energy level alignment are relevalnt.

In order to understand the implications of ordered molecular stacking on physical properties of transition metal complexes, we have employed vacuum deposited Zinc Octaethyl porphyrin (ZnOEP) thin films with a different degree of long-range order as model systems. This choice is due to the fact that though similar to the CuOEP, ZnOEP presents a higher photovoltaic efficiency and no polymorphism in the film structure. In the literature higher photovoltaic yield is found for ordered ZnOEP TF. Our intention is to provide an insight into the inter-relation between the intermolecular interaction and the long range ordering of organic semiconductors by considering Zinc octaethyl porphyrin (ZnOEP) as model system. In order to highlight the

influence of intermolecular interaction, ZnOEP thin films are typically grown on ITO and silicon and characterized by a combination of complementary techniques to study the structural, vibrational and morphological details of organic thin films at different size scales, from the molecular comformers structure to the grain size. Grazing incidence X-Ray diffraction(GIXRD) analysis reveals that the differently grown ZnOEP films obtained by UHV vapor deposition presents different degree of long range ordering, paracrystallinity and average crystallites size. Raman spectroscopy together with x-ray absorption analysis indicates towards weak intermolecular interactions among adjacent ZnOEP molecules in the thin films while the alterations in the macrocycle bond distances are found to be modest. Influence of peripheral ethyl groups conformations on vibrational properties are more pronounced for ordered thin films grown on silicon substrate as compared to disordered films. Theoretical modeling of Raman and XAS spectrum are performed to further comprehend the effect of molecular stacking of differently grown ZnOEP thin films on the intermolecular interactions. Zn K edge of the as grown ZNOEP films has been modeled by MXAN analysis, establishing a symmetry reduction in the molecular conformers and a relevant influence on the ethyl conformations on the molecular ordering. These structural variations in ordered ZnOEP TF correspond to a higher density of inter-molecular charge-transfer excitons found in the optical absorption spectra and could be related to an improvement of the photovoltaic yield.

It has been demonstrated that work function and interfacial charge transfer can be significantly influenced by the introduction of graphene buffer layer between transition metal complexes adsorbed on metallic substrates. There are few investigations to explore the impact of intermediate 2D layer on the interfacial electroninc properties of adsorbed moelcules on metallic substrates. Influecne of graphene layers on the work function alterations and chargre injection barriers for porphyrin adlayers on different metallics substrates is still an open questions. We devote chapter six to address this issue. To achieve this goal we selected Gr/Ni(111), Gr/Pt(111) and HOPG substrates so that comparison between weakly interacting graphene can be made with strongly interacting graphene. HOPG is taken as refrecne substrate due to its weakly interacting nature with porphyrin.

These substrates enable us to highlight the impact of dissimilar graphene-substrate coupling and unique surface properties of these substrates on interaction with adsorbed molecules, which in turn control the interface dipole, energy level alignment, and bond strength and adsorption geometry of the molecules. In this context, photoemission and X-ray absorption spectroscopy have been utilized to demonstrate the ability of graphene to control the interaction of FeTPP-Cl adsorbed onto Gr/Ni(111) and Gr/Pt(111) substrates. FeTPP-Cl molecules decouple from the underlying Pt(111) substrate in contrast to Gr/Ni(111) due to weaker graphene-substrate interaction. Photoemission analysis reveals that work function alterations and energy level alignment at Gr/Pt(111) interface exhibits resemblance with adsorption onto HOPG demonstrating weaker metal-molecule interactions. C K edge NEXAFS demonstrates that the peripheral phenyl groups of FeTPP-Cl adopts near gas phase configuration for the adsorption on

HOPG in contrast to Gr/Ni(111) and Gr/Pt(111). The study establishes the ability of graphene to alter the energy level alignment at tetrapyrrole complexes interfaces onto conducting substrates. The presence of an interface state at 0.3 eV below the E_F measured in the caase of Gr/Ni(111) substrate suggesst the possibility of the gap opening in the FeTPP-Gr system, previewed by the recent theoretical calculations [17], though the simulation is referred to a free-standing graphene layer. Notably the interface state is absent in the case of Gr/Pt(111) case. Further work is mandatory to confirm this point.

Second part of chpater five is focused on the electronic properties of ferrocene/Graphene interface on ferromagnetic surface and its comparative behviour on HOPG. The motivation of the study is to invesitgate the dissimilarties in the intrfacial electroninc properties of Ferrocene/HOPG and Ferrocene /Gr/Ni(111) systems due to peculier differecnes in the surface proeperties of graphene and HOPG. Interestingly, Fe $L_{2,3}$ analysis indicates no significant charge transfer from Ni(111) to the iron ion and ferrocene almost desorbs completely due to weaker interaction with underlying transition metal substrate passivated by intermediate graphene layer. Moreover, ferrocene molecules do not desorb at room temperature on HOPG in contrast to Gr/Ni(111) probably due to captive environment provided by layered HOPG structure and π-π interactions.

Although, considerable attention has been given to understand the electronic and magnetic properties of porphyrin and phthalocyanine molecules adsorbed on metallic substrates. However, adsorption of these molecules on oxides and nitrides surfaces is still not widely studied. The potential of IPES can be utilized to explore the perturbations of unoccupied density of states induced by the interaction of these molecules with oxide and nitride surfaces. Another interesting area is the tuning of porphyrin and phthalocyanine molecules interfacial electronic properties by the adsorption on 2D nanostrucutured materials such as GdAu$_2$ 2D-layers on Au(111) which forms a moiré pattern when Gd ions adsorbed on Au(111). [results published in Correa *et al.* Nanoscale 2017, 9, 17342, in collaboration with Dr. Lucia Vitali Universidad del País Vasco, Spain] .These findings can provide insight into the interface effects on the electronic properties of 2D materials and on the importance of their distortion from the planar geometry. Magnetic properties studies of these systems using XMCD(X-ray magnetic circular dichroism) can provide plethora of information about magnetic behavior of porphyrin and phthalocyanine molecules. Therefore, there are still certain loose ends in the surface science of porphyrin and phthalocyanine molecules, which needs further investigations.

Publications

- A Kumar, Naumenko D, Cozzarini L, Barba L, Cassetta A, Pedio M. Influence of substrate on molecular order for self-assembled adlayers of CoPc and FePc. J Raman Spectrosc. 2018, 49, 1015–1022.

- A. Kumar, D. Naumenko, G. Rossi, E. Magnano, S. Nappini, F. Bondino, E. Segoloni, L. Amidani, F. d'Acapito, F. Boscherini, L. Barba, E. Pace, M. Benfatto, S. Casassa, and M. Pedio, "Effect of long-range order on Intermolecular Interactions in Organic Semiconductors: Zinc octa ethyl porphyrin molecular thin films model systems" Accepted to journal of Physical Chemistry Chemical Physics.

- A. Kumar, A. Goldoni, M. Panighel, A.Nefedov, C. Cepek , M.Pedio. "Tuning of Interfacial Electronic Properties by Intermediate Graphene Layer on Transition Metal Surfaces" (In preparation).

- A. Kumar, C. Soncini, A. Papadopoulos, E. Serpetzoglou, E. I. Stratakis, F. Bondino, E. Magnano, I. Pis, M. Stupar, B. Ressel, G. D. Ninno, L. Barba, M. Pedio "Impact of Co-phthalocyanine thin films polymorphism on electronic and ultrafast optical dynamical effects "(In preparation).

- A. Kumar, C. Cepek, A. Goldoni, A. Nefedov, M. Pedio"Electronic properties of Ferrocene/Graphene interface on ferromagnetic surface and intercalation into pyrolytic graphite"(In preparation).

Other publications

- Correa, M.F. Camellone, A. Barragan, A. Kumar, C. Cepek, M. Pedio, S.Fabris, L. Vitali, "Self- texturizing electronic properties in a 2-dimensional $GdAu_2$ layer on Au(111): the role of out-of-plane atomic displacement", Nanoscale, 2017,9, 17342-17348.

- Correa, M.F. Camellone, A. Barragan, A. Kumar, C. Cepek, M. Pedio, S.Fabris, L. Vitali "Electronic properties of the de-hydrogenated H2-phthalocyanine molecule on GdAu2/Au(111)" in preparation

Appendix

It is worthwhile to mention that splitting of the molecular orbitals for transition metal complexes in the ligand field strongly depends on the coordination geometries as shown in figure below

Figure A1 Splitting of d-orbital energy levels in ligand fields of different symmetries [1]

It is important to highlight some important aspects when molecules form crystalline thin films on substrates. Actually, in the solid state form gas phase values of IE_g and EA_g and corresponding energy gap are modified due to polarization energies. The Figure below represents the schematic diagram for the IE_g and EA_g of isolated molecules in gas phase. As shown in Figure in the solid

state form due to the polarization of the surrounding media IE_g decreases by the positive polarization energy P+ and increases EA_g by the negative polarization energy P−.[2]

The polarization energy of the cation (P^+) is defined as the difference in energy between the ionization energy of the molecular system in the crystal (IE) and the ionization energy of the molecular system in the gas phase (IE_{gas}). Similarly (P^-)can be defined for anion.

$$P^+ = IE\text{-}IE_g$$

$$P^- = EA\text{-}EA_g$$

Importantly, transport band gap is further affected by geometric distortions which can change the bond lengths of molecule.The energy associated with geometrical change in the molecular structure is known as the geometric relaxation energy λ, and the charge traveling through the molecular crystal, that comes along with the geometric distortion of the molecules, is commonly referred to as "polaron". Moreover, the geometrical reorganization energy λ+/− further decreases/increases the vertical IE/EA resulting in an energy gap of Δ_{trans}. Further, the transport band gap is not equal to optical band gap. The difference between Δt_{rans} and Δ_{opt} is the Coulomb attraction between electron and hole, called exciton-binding energy (Eexciton). The Figure below summarizes difference contributions resulting in change of gas pahse values of IE and EA.
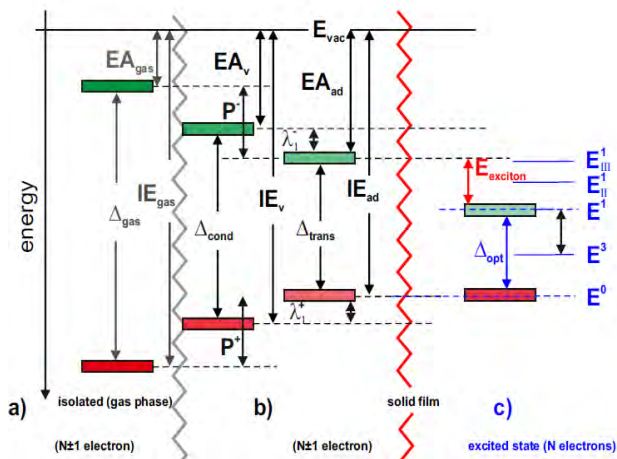

Figure A2 Schematic HOMO and LUMO frontier energy levels, of (a) an isolated molecule in the gas phase, with IEgas, EAgas and the energy gap Δgas. (b) Respective energy levels of a molecule in a solid (condensed film), where the polarization of the surrounding media decreases IEgas by the positive polarization energy P^+ and increases EAgas by the negative polarization energy P^-. The energetic difference between both energy levels is the conductivity gap Δcond. Moreover, the geometrical reorganization energy _+/− further decreases/increases the vertical IE/EA resulting in an energy gap of Δtrans. In (c) the fundamental optical transition E^0 _ E^1 (triplet (E^3) or higher excitations (E^1_{II} , E^1_{III}) are indicated) yields the optical band gap Δopt. Comparing Δtrans and Δopt yields an energy difference corresponding to the exciton binding energy ($E_{exciton}$).[2].

References

1. Espen Tangen, PhD Thesis 'High valent transition metal corrole and corrolazine complexes', University of Tromsø.

2. Stefanie Winkler, PhD Thesis 'Photoelectron spectroscopy of polaron in molecular semiconductors', University of Berlin.

Symbols and Abbreviations

2H-TPP-- 2H-5,10,15,20-tetra-phenyl-porphyrin

2H-OEP-- 2H-octa-ethyl-porphyrin

AFM—Atomic Force Microscopy

CoTPP-- Co(II)-tetra-phenyl-porphyrin

CuOEP-- Copper octathyl porphyrin

CuPc-- Copper phthalocyanine

CoPc -- Cobalt Phthalocyanine

FeCp$_2$--Ferrocene

DFT-- Density functional theory

DOS--local density of states**FeOEPCl --**Fe(III)-octa-ethyl-porphyrin-Cl

Fe-TPPCl-- Fe(II)-tetra-phenyl-porphyrin-Cl

GIXRD—Grazing Incidence X-ray Diffraction

HOMO--highest occupied molecular orbital

 hv—photon energy

IPES—Inverse Photoemission Spectroscopy

LEED –Low Wlwctron Energy Diffraction

LUMO-- Lowest unoccupied molecular orbital

MO—Molecular Orbitals

MOEP—Transition Metal Octaethyl Porphyrin

MPc--Transition Metal Phthalocyanine

MTTP--Transition Metal Tetraphenyl Porphyrin

ML--monolayer

NEXAFS--Near-edge X-ray absorption fine structure

PES -- Photoemission spectroscopy

P&P—Pump and Probe

RT – Room Temperature

STM—Scanning Tunneling Microscopy

WF – Work Function

XAS – X-ray Absorption Spectroscopy

XMCD --X-ray magnetic circular dichroism

XPS—X –ray Photoemission Spectroscopy

UHV—Ultra High Vacuum

ZnOEP-- Zn(II)-octa-ethyl-porphyrin

Acknowledgements